

THE SPATIALLY RESOLVED STAR FORMATION LAW FROM INTEGRAL FIELD SPECTROSCOPY:
VIRUS-P OBSERVATIONS OF NGC 5194GUILLERMO A. BLANC,¹ AMANDA HEIDERMAN,¹ KARL GEBHARDT,¹ NEAL J. EVANS II,¹ JOSHUA ADAMS¹*Draft*

ABSTRACT

We investigate the relation between the star formation rate surface density (Σ_{SFR}) and the mass surface density of gas (Σ_{gas}) in NGC 5194 (a.k.a. M51a, Whirlpool Galaxy). VIRUS-P integral field spectroscopy of the central 4.1×4.1 kpc² of the galaxy is used to measure H α , H β , [NII] $\lambda\lambda 6548, 6584$, and [SII] $\lambda\lambda 6717, 6731$ emission line fluxes for 735 regions ~ 170 pc in diameter. We use the Balmer decrement to calculate nebular dust extinctions, and correct the observed fluxes in order to measure accurately Σ_{SFR} in each region. Archival HI 21cm and CO maps with similar spatial resolution to that of VIRUS-P are used to measure the atomic and molecular gas surface density for each region. We present a new method for fitting the Star Formation Law (SFL), which includes the intrinsic scatter in the relation as a free parameter, allows the inclusion of non-detections in both Σ_{gas} and Σ_{SFR} , and is free of the systematics involved in performing linear correlations over incomplete data in logarithmic space. After rejecting regions whose nebular spectrum is affected by the central AGN in NGC 5194, we use the [SII]/H α ratio to separate spectroscopically the contribution from the diffuse ionized gas (DIG) in the galaxy, which has a different temperature and ionization state from those of H II regions in the disk. The DIG only accounts for 11% of the total H α luminosity integrated over the whole central region, but on local scales it can account for up to a 100% of the H α emission, especially in the inter-arm regions. After removing the DIG contribution from the H α fluxes, we measure a slope $N = 0.82 \pm 0.05$, and an intrinsic scatter $\epsilon = 0.43 \pm 0.02$ dex for the molecular gas SFL. We also measure a typical depletion timescale $\tau = \Sigma_{HI+H_2}/\Sigma_{SFR} \approx 2$ Gyr, in good agreement with recent measurements by Bigiel et al. (2008). The atomic gas density shows no correlation with the SFR, and the total gas SFL in the sampled density range closely follows the molecular gas SFL. Integral field spectroscopy allows a much cleaner measurement of H α emission line fluxes than narrow-band imaging, since it is free of the systematics introduced by continuum subtraction, underlying photospheric absorption, and contamination by the [NII] doublet. We assess the validity of different corrections usually applied in narrow-band measurements to overcome these issues and find that while systematics are introduced by these corrections, they are only dominant in the low surface brightness regime. The disagreement with the previous measurement of a super-linear molecular SFL by Kennicutt et al. (2007) is most likely due to differences in the fitting method. Our results support the recent evidence for a low, and close to constant, star formation efficiency ($SFE = \tau^{-1}$) in the molecular component of the ISM. The data shows an excellent agreement with the recently proposed model of the SFL by Krumholz et al. (2009b). The large intrinsic scatter observed may imply the existence of other parameters, beyond the availability of gas, which are important at setting the SFR.

Subject headings: galaxies:

1. INTRODUCTION

In the quest to achieve a thorough understanding of the processes involved in the formation and subsequent evolution of galaxies, we must first fully characterize the process of star formation under different environments in the ISM. During the last decade, major efforts have been made to characterize the variables involved in triggering star formation and setting the star formation rate (SFR) in galaxies. Kennicutt (1998b) showed that, integrating over the whole optical disk of galaxies, the star formation rate surface density (Σ_{SFR}), as measured by the H α emission, tightly correlates with the total gas surface density (Σ_{HI+H_2}) over several orders of magnitude in SFR and gas density. The relation from Kennicutt follows a power-law form, with a slope $N = 1.4$. These types of correlations between Σ_{SFR} and Σ_{gas} , either atomic (Σ_{HI}), molecular (Σ_{H_2}), or total (Σ_{HI+H_2}),

are usually known as Star Formation Laws (SFL, a.k.a. Schmidt Laws or Schmidt-Kennicutt Laws, after Schmidt 1959, who first introduced the power-law parametrization to relate gas density and the SFR), and they show that the availability of gas is a key variable in setting the SFR.

Although the global SFL provides us with valuable insights on the role that gas density plays at setting the SFR, the measurement involves averaging over the many orders of magnitude in Σ_{gas} and Σ_{SFR} present in the ISM of single galaxies, implying the loss of valuable information about the detailed physics that give rise to the SFL. Azimuthally averaged measurements of gas surface densities and the SFR have been used to conduct more detailed studies of the SFL across the disks of local galaxies. For example, Wong & Blitz (2002) measured, under the assumption of constant dust extinction, a slope of $N \approx 0.8$ for the molecular SFL, and $N \approx 1.1$ for the total gas SFL on a sample of seven molecule rich spirals, with

¹ Astronomy Department, University of Texas at Austin, USA

a large scatter from galaxy to galaxy, and Schuster et al. (2007) measured $N = 1.4 \pm 0.6$ for the total gas SFL on NGC 5194. Azimuthally averaged profiles are also affected by averaging effects since Σ_{SFR} and Σ_{gas} can change by more than 2 orders of magnitude at constant galactocentric radius due to the presence of spiral structure. We refer the reader to Bigiel et al. (2008) for a thorough compilation of previous measurements of the SFL in local galaxies.

More recently two studies have been aimed at measuring the “spatially resolved” SFL throughout the disks of nearby galaxies. Kennicutt et al. (2007) used a combination of narrow-band $H\alpha$ and $24\mu\text{m}$ photometry to estimate Σ_{SFR} , as well as 21cm and CO J=1-0 maps to measure Σ_{gas} for 257 star-forming regions, 520 pc in diameter, in the disk of NGC 5194. They measured slopes of $N = 1.37 \pm 0.03$ and $N = 1.56 \pm 0.04$ for the molecular and total gas SFL respectively. Bigiel et al. (2008) used far-UV and $24\mu\text{m}$ images to create a Σ_{SFR} map, and 21cm, CO J=2-1, and CO J=1-0 data to create Σ_{gas} maps of seven spiral galaxies and eleven late-type/dwarf galaxies. After convolving the maps to a common resolution of 750 pc, they performed a pixel-to-pixel analysis and measured a molecular SFL with an average $N = 1.0 \pm 0.2$ for the normal spirals ($N = 0.84$ for NGC 5194). Both studies found a lack of correlation between the SFR and the atomic gas density, which saturates around a value of $10 \text{ M}_{\odot} \text{pc}^{-2}$. This value is thought to be associated with a density threshold for the formation of molecular gas, and is consistent with predictions from theoretical modeling of giant atomic-molecular complexes (Krumholz et al. 2009a). The total gas SFL is then driven by the correlation between the molecular gas density and the SFR, and the molecular fraction in the ISM. At the highest densities present in normal spiral galaxies ($\Sigma_{HI+H_2} = 50 - 1000 \text{ M}_{\odot} \text{pc}^{-2}$) the ISM is mostly molecular and the total gas SFL closely follows the H_2 SFL. At densities lower than $10 \text{ M}_{\odot} \text{pc}^{-2}$ the total gas SFL gets much steeper due to a strong decrease of the molecular fraction. This behavior has been recently modeled by Krumholz et al. (2009b).

While spatially resolved studies of the SFL obtain consistent results on the behavior of the atomic gas, they disagree when it comes down to the molecular component. The Bigiel et al. (2008) measurement of a linear molecular SFL is consistent with a scenario in which star formation occurs at a constant efficiency inside GMCs, whose properties are fairly uniform across normal spiral galaxies (Blitz et al. 2007; Bolatto et al. 2008). This homogeneity in the properties of GMCs is expected if they are internally regulated by processes like stellar feed-back, and they are decoupled from their surroundings due to the fact of being strongly overpressured (Krumholz et al. 2009b). Kennicutt et al. (2007), on the other hand, measured a super-linear molecular SFL in NGC 5194, which suggests an increasing SFE towards higher gas densities. Although the authors state that a super-linear slope ($N > 1$) is still consistent with a constant “efficiency” if the star-forming lifetimes of massive clouds were systematically lower than those of low-mass clouds, this is true only if the efficiency is defined as the ratio of the produced stellar mass over the available molecular gas mass, which is the classical definition used by galactic studies in the Milky Way. In this work, as well as in Bigiel et al.

(2008), the efficiency is defined as $\text{SFE} = \Sigma_{SFR} / \Sigma_{gas}$, or the inverse of the depletion time, so shorter star formation timescales imply a higher SFE, and a super-linear SFL always translate in higher SFE at higher gas densities.

With the goal of investigating this issue, we have conducted the first measurement of the spatially resolved SFL using integral field spectroscopy. We mapped the $H\alpha$ emission in the central $4.1 \times 4.1 \text{ kpc}^2$ of the nearby face-on spiral galaxy NGC 5194 using the Visible Integral field Replicable Unit Spectrograph Prototype (VIRUS-P, Hill et al. 2008). Hydrogen recombination lines are known to be good tracers of the SFR. Their intensity scales linearly with the ionizing UV flux in galaxies, which is dominated by the emission from massive stars ($\geq 10 \text{ M}_{\odot}$) with typical lifetimes of $< 20 \text{ Myr}$, hence they provide an almost instantaneous measurement of the SFR (Kennicutt 1998a, and references therein).

Due to the small field of view of current integral field units (IFUs), typically less than 1 arcmin^2 , 2D spectroscopic $H\alpha$ mapping of nearby galaxies with large angular sizes has not been conducted efficiently in the past. Instead, narrow-band imaging has been typically used to construct $H\alpha$ based SFR maps. $H\alpha$ narrow-band imaging suffers from contamination from the $[\text{NII}]\lambda\lambda 6548, 6584$ doublet, and is sensitive to systematic errors in continuum subtraction and the estimation of the strength of the $H\alpha$ absorption in the underlying stellar spectrum. Spectroscopic measurements are free of all these sources of error, and hence provide a much cleaner measurement of $H\alpha$ fluxes. A major part of this paper is dedicated to investigate these systematics in order to assess the validity of the typical corrections applied to narrow-band $H\alpha$ images.

VIRUS-P is the largest field of view IFU in the world and it allows for efficient $H\alpha$ mapping of nearby galaxies. The observations presented here were taken as part of the VIRUS-P Exploration of Nearby Galaxies (VENGA², Blanc et al. in preparation). VENGA is a large scale extragalactic IFU survey that will spectroscopically map large parts of the disks of ~ 20 nearby spirals, to allow a number of studies on star-formation, structure assembly, stellar populations, gas and stellar dynamics, chemical evolution, ISM structure, and galactic feedback.

The VIRUS-P spectral map was used in combination with CO J=1-0 and HI 21cm intensity maps of NGC 5194 from the BIMA Survey of Nearby Galaxies, SONG (Helfer et al. 2003), and The HI Nearby Galaxy Survey, THINGS (Walter et al. 2008), to measure Σ_{SFR} , Σ_{H_2} , and Σ_{HI} in order to construct the spatially resolved SFL. In §2 and §3 we present the VIRUS-P observations and the data reduction and calibration methods. In §4 we describe the CO and 21cm data used to measure the molecular and atomic gas surface densities, as well as a HST NICMOS Pa α image used to validate our dust extinction measurements. §5 presents the methods used to remove the stellar continuum and measure accurate nebular emission line fluxes, together with our dust extinction correction. The calculation of Σ_{gas} is described in §6. The rejection of regions whose nebular emission is affected by the central AGN in NGC 5194 is presented in §7. The correction to account for the contribution of

² <http://www.as.utexas.edu/~gblancm/venga.html>

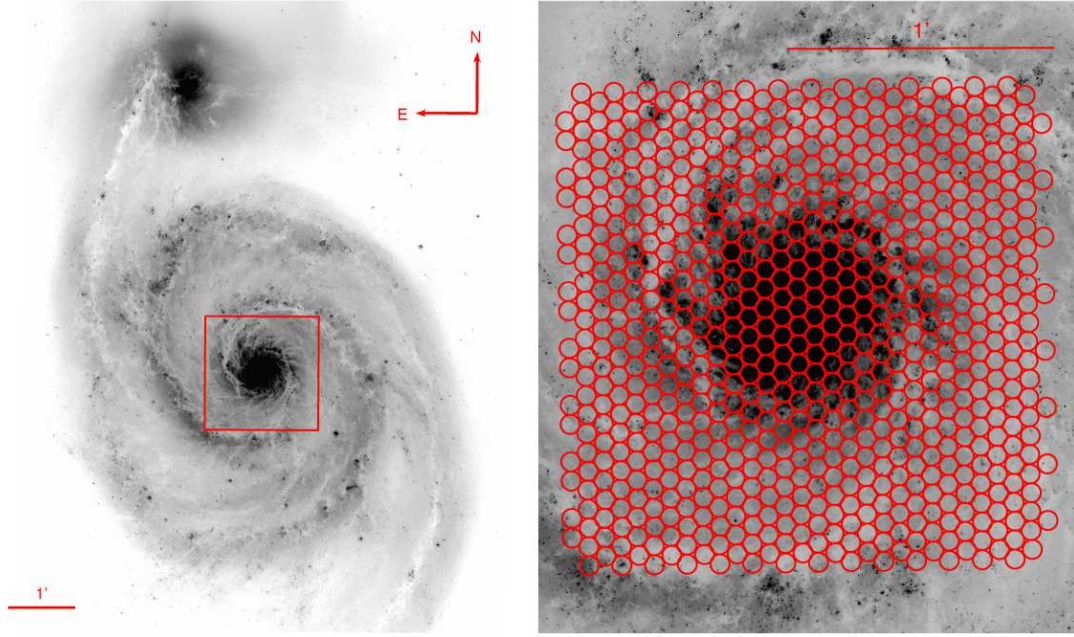


FIG. 1.— *Left*: HST+ACS V-band image of NGC5194 and its companion NGC 5195 (Mutchler et al. 2005). The central 4.1×4.1 kpc² region sampled by the $1.7' \times 1.7'$ VIRUS-P field of view is marked in red. *Right*: Map of the 738 regions sampled by VIRUS-P in the 3 dither positions. Each region has a diameter of $4.3''$ corresponding to ~ 170 pc at the distance of NGC5194.

the DIG to the H α fluxes is described in §8. The resulting spatially resolved SFLs for the molecular, atomic and total gas are presented in §9, followed by a discussion on the implications of our results for narrow-band imaging surveys in §10. Finally we compare our results with previous measurements and theoretical predictions of the SFL in §11, and present our conclusions in §12.

Throughout this paper we assume a distance to NGC 5194 of 8.2 Mpc for consistency with Kennicutt et al. (2007). While Bigiel et al. (2008) used a slightly smaller distance of 8.0 Mpc, it is worth noticing that most of the results in this paper are based on surface densities, which are independent of distance, and thus are not affected by the assumed value. All values for Σ_{SFR} are in units of $M_{\odot} \text{yr}^{-1} \text{kpc}^{-2}$, and values of Σ_{gas} are in units of $M_{\odot} \text{pc}^{-2}$.

2. OBSERVATIONS

We obtained spatially resolved spectroscopy over the central 4.1×4.1 kpc² region of NGC 5194 on the night of April 4, 2008, using VIRUS-P on the 2.7m Harlan J. Smith telescope at McDonald Observatory. VIRUS-P with the VP-2 IFU bundle used in this work consists of a square array of 246 optical fibers which samples a $1.7' \times 1.7'$ field of view with a 1/3 filling factor. The fibers are $200 \mu\text{m}$ in diameter, corresponding to $4.3''$ on sky. The spectrograph images the spectrum of the 246 fibers on a 2048×2048 Fairchild Imaging CCD. Because of camera alignment issues, the spectrum of one fiber fell off the chip, reducing the number of usable fibers to 245.

The spectrograph was used in a red setup under which it samples a wavelength range of 4570-6820Å with a spectral resolution of $\sim 5.0\text{\AA}$ (FWHM). This red setup allows us to sample both H β and H α , and our resolution is high enough to resolve the H α -[NII] $\lambda\lambda 6548, 6893$ complex. We took the data in 2×1 binning mode in the spectral direc-

tion which translates into a plate scale of $2.2 \text{\AA pixel}^{-1}$. Given the 1/3 filling factor of the IFU, three dithered exposures were necessary to sample the complete field of view.

We obtained four 20 minute exposures at each of the 3 dither positions, accounting for an effective exposure time of 80 minutes. Dither 1 was centered at $\alpha=13:29:52.69$; $\delta=+47:11:43.0$. Dithers 2 and 3 were offset from dither 1 by $\Delta\alpha = -3.6''$; $\Delta\delta = -2.0''$ and $\Delta\alpha = 0.0''$; $\Delta\delta = -4.0''$ respectively. Figure 1 shows the observed region in NGC 5194 as well as the position of the IFU fibers for the 3 dithers. Because of the extended nature of NGC 5194 no fibers in the field of view sampled a blank region of the sky. This implied the need for off-source sky frames in between science frames. We obtained 5 minute sky exposures bracketing all science exposures. These were obtained $30'$ North of NGC 5194. The typical seeing during the observations was $2.0''$.

Bias frames, comparison NeCd lamps, and twilight flats were taken at the beginning and end of the night. VIRUS-P is mounted on a two-degree of freedom gimble at the broken cassegrain focus of the telescope. The gimble keeps the spectrograph in a fixed gravity vector independent of the position of the telescope during the observations which translates into a practically complete lack of flexure in the spectrograph optical components. For this reason calibration frames intercalated with the science observations were not necessary.

The spectro-photometric standard Feige 34 was observed for the purpose of flux calibration (see §3.1). Standard observations were performed using a finer 6 position dither pattern which better samples the PSF of the star and ensures the collection of its total flux (see §3.1 and Figure 2).

The instrument is equipped with a guiding camera which images a $4.5' \times 4.5'$ field offset from the science field

sampled by the IFU. The guiding camera is a 512×512 pixel Apogee unit equipped with a BV filter which allows broad-band photometric measurements of the stars in the field. During the night we saved a guider frame every 30 seconds in order to reconstruct changes in atmospheric transparency. The guider images are also used to establish the IFU astrometry. The relative offset, rotation and plate scales of the guider and IFU fields have been precisely calibrated using observations of crowded fields in open clusters, so the pixel coordinates of stars in the guider frames provide us with coordinates for the center of all fibers in the IFU with an astrometric rms of $\sim 0.5''$.

In this way we obtained spectra for 735 regions $4.3''$ in diameter (~ 170 pc at the distance of NGC 5194), in the central region of the galaxy. The spectra reaches a median 5σ sensitivity in continuum flux density of 2.5×10^{-17} erg s $^{-1}$ cm $^{-2}$ Å $^{-1}$, which translates into a median signal-to-noise (S/N) ratio per resolution element of 95 (53 for the faintest fiber).

3. DATA REDUCTION

Data reduction is performed using our custom pipeline VACCINE (Adams et al. in preparation). Individual frames are overscan and bias subtracted, and bad pixels are masked. We use the twilight flats to trace the peak of the spatial profile of the spectrum of all fibers on the chip, and extract the 2D spectrum of each fiber on the science frames, comparison lamp frames, and flats using a seven pixel aperture around the peak.

The extracted comparison lamp spectra are used to compute an independent wavelength solution for each fiber. We use 4th order polynomials to compute the wavelength solutions which show a typical rms of 0.2 Å (~ 0.1 pixel).

We correct the twilight flats for solar absorption lines and use them to measure the shape and amplitude of the spatial profile of the fibers as a function of wavelength. This profile is given by the point spread function (PSF) of the fibers on chip in the spatial direction, and the relative instrumental throughput of each fiber as a function of wavelength. Dividing the twilight flats by this profile yields a pixel-to-pixel flat. We divide all science, sky, and spectro-photometric standard frames by both the fiber profile and the pixel-to-pixel flats. This removes any fiber-to-fiber and pixel-to-pixel variations in sensitivity.

A background frame is created for each science exposure by averaging the two bracketing 5 minute sky frames and scaling by the difference in exposure time. We estimate the sky spectrum for each fiber by fitting a non-uniform spline to the spectra of the 60 neighboring fibers on chip in the background frame. This spectrum is subtracted from each fiber in the science data.

In order to test the quality of our background subtraction algorithm we construct background frames for each of our sky exposures using the two closest of the other sky exposures. We then follow the same procedure to background subtract our sky frames. We observe residuals centered around zero in the background subtracted sky frames that are less than 1% of the galaxy continuum flux in the faintest fibers in our science data. The only exception are the regions of the spectra at the wavelength of the 4 brightest sky emission lines in our wavelength range in which the residuals can be considerably larger

due to the fast time variability of these spectral features. These regions showing poor background subtraction are masked in our science data. At this stage we combine individual exposures using a biweight (Beers et al. 1990).

Error maps including Poisson photon count uncertainties and read-noise are created for every fiber on each frame. We use these error maps together with the fiber profile to calculate the weights used for collapsing the 2D spectrum into a 1D spectrum. The flux in photoelectrons at each wavelength after collapsing is given by

$$f_{\lambda} = \frac{\sum_{i=1}^7 \left(\frac{p_i}{e_i}\right)^2 G f_{\lambda,i}}{\sum_{i=1}^7 \left(\frac{p_i}{e_i}\right)^2} \quad (1)$$

where p_i is the value of the fiber profile, G is the gain, f_i is the flux in ADUs in the combined background subtracted spectrum, and e_i is the corresponding error at each pixel as measured in the error map. This is equivalent to weighting the pixels by $(S/N)^2$. The sum is performed at every wavelength (column) over the the 7 pixel aperture used for extraction. The final product is a wavelength calibrated 1D spectrum of the area sampled by each of the 245 fibers on each of the 3 dither positions on the galaxy.

3.1. Flux Calibration

Flux calibration of IFU data can be challenging but, if proper care is taken, very accurate spectro-photometry can be achieved. This is mostly because of the lack of a wavelength dependent slit loss function. Atmospheric dispersion can change the position of a standard star in the field of view as a function of wavelength, but as long as the field is completely sampled by the fibers the total flux of the star at all wavelengths is always collected. Also, photometry of stars in the guider images taken during the observations allows us to measure and correct for changes in atmospheric transparency during the night.

During the observation of standard stars, fibers in the IFU only sample a region of the star's PSF. Determining the fraction of the total flux collected by each fiber is essential in order to compute a proper instrumental sensitivity function by comparing each fiber spectrum to the total intrinsic spectrum of the star. This requires knowledge of the shape of the PSF as well as the distance from the PSF centroid to the center of each fiber.

The spectro-photometric standard star Feige 34 was observed using a 6 position dither pattern shown in the left panel of Figure 2. This tight pattern provides a better sampling of the PSF and ensures we collect the total flux of the star. We calculate the position of the centroid of the PSF relative to the fibers by taking the weighted average of the fibers positions in the field of view, using the measured flux in each of them as weights. This corresponds to the first moment of the observed light distribution.

The filled circles in the right panel of Figure 2 show the flux measured in each fiber as a function of its radial distance to the PSF center. This information can be used to reconstruct the shape of the star PSF at the moment of the observations. In order to do this, we assume a Moffat profile for the PSF and reconstruct its observed light distribution by summing the flux in $4.3''$

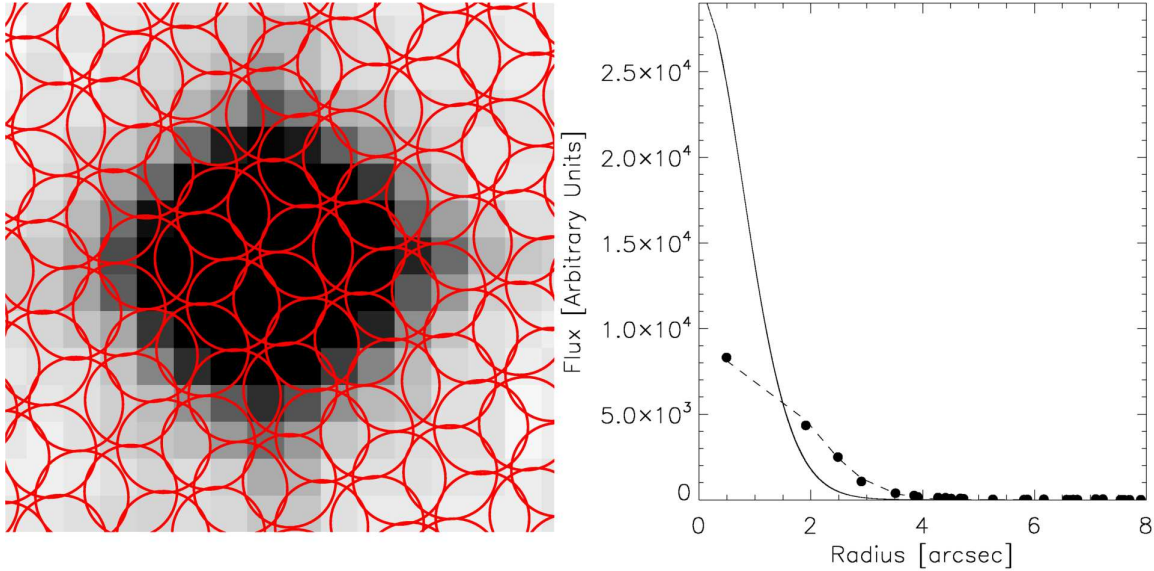


FIG. 2.— *Left:* DSS image of Feige 34. Superimposed is the 6 dither position pattern used to observe spectro-photometric standard stars. *Right:* Flux measured by each fiber as a function of its distance to the PSF centroid (filled circles). Also shown are the best-fitted Moffat PSF (solid line), and its fiber-sampled light distribution (dashed line).

diameter circular apertures at the corresponding radial distance of each fiber. The best-fitted PSF and its fiber sampled light distribution are shown by the solid and dashed curves in the right panel of Figure 2. It can be seen that the best-fitted model PSF, after being sampled by the fibers in our dither pattern, matches the measured flux remarkably. This PSF model allows us to know what fraction of the star total flux was measured by each fiber during the observations.

We normalize the spectrum of each fiber by the fraction of the total flux it sampled, and average this value for all fibers having a significant ($> 5\sigma$) flux measurement in order to obtain the star total instrumental spectrum. We correct the total spectrum by atmospheric extinction and use the Feige 34 measurement of Oke (1990) to construct our instrumental sensitivity function.

Relative variations in atmospheric transparency during the night are measured by performing aperture photometry on stars in the guider images. Observing conditions were confirmed to be very stable, with maximum variations in transparency of less than a 10%. All spectra in our science frames are corrected by this variations, atmospheric extinction, and flux calibrated using the instrumental sensitivity function.

It is important to notice that any difference in illumination or throughput between fibers was taken out during the flat-fielding process, so a common sensitivity function applies to all fibers. Our final product is a wavelength and flux calibrated spectrum for the 735 regions.

In order to estimate the systematic uncertainty in our flux calibration we have compared sensitivity functions computed using different standard star observations taken as part of different observing programs with VIRUS-P. Comparison of 10 standards taken between September 2007 and June 2008 under different observing conditions show that after correcting for relative changes in atmospheric transparency (using photometry of stars in the guider images) the computed sensitivity functions

show an rms scatter of less than 5%.

4. OTHER DATA

4.1. THINGS HI Data

We use a combined 21 cm line intensity map of NGC 5194 from the Very Large Array (VLA) taken as part of The HI Nearby Galaxy Survey (THINGS³; Walter et al. 2008) to estimate the atomic gas surface density (Σ_{HI}). HI data for NGC 5194 was taken using the B, C, and D arrays during 2004 and 2005, with a combined on source integration time of ~ 10 hours. The final co-added (B+C+D array) integrated intensity map has a robustly weighted beam size of $5.82'' \times 5.56''$, which is well matched to the $4.3''$ VIRUS-P fiber diameter convolved with the $2''$ seeing. The 1σ noise per 5.2 km s^{-1} channel is $0.44 \text{ mJy beam}^{-1}$ corresponding to a atomic gas surface density of $\Sigma_{HI} = 0.59 \text{ M}_{\odot} \text{ pc}^{-2}$. For more details on data products and data reduction see Walter et al. (2008).

4.2. BIMA SONG CO Data

Molecular gas surface densities are measured using the CO J=1-0 intensity map of NGC 5194 from the Berkeley Illinois Maryland Array (BIMA) Survey of Nearby Galaxies (BIMA SONG⁴; Helfer et al. 2003). Zero spacing single dish data from the NRAO 12 m telescope was combined with the interferometric BIMA C and D array data, resulting in a map with a robust beam size of $5.8'' \times 5.1''$, well matched to the 21 cm map and the VIRUS-P spatial resolution. The corresponding 1σ noise is 61 mJy beam^{-1} in a 10 km s^{-1} channel or $\Sigma_{H_2} = 13 \text{ M}_{\odot} \text{ pc}^{-2}$. For more details on the observations and the data reduction refer to Helfer et al. (2003).

³ <http://www.mpia.de/THINGS/Data.html>

⁴ <http://nedwww.ipac.caltech.edu/level5/March02/SONG/SONG.html>

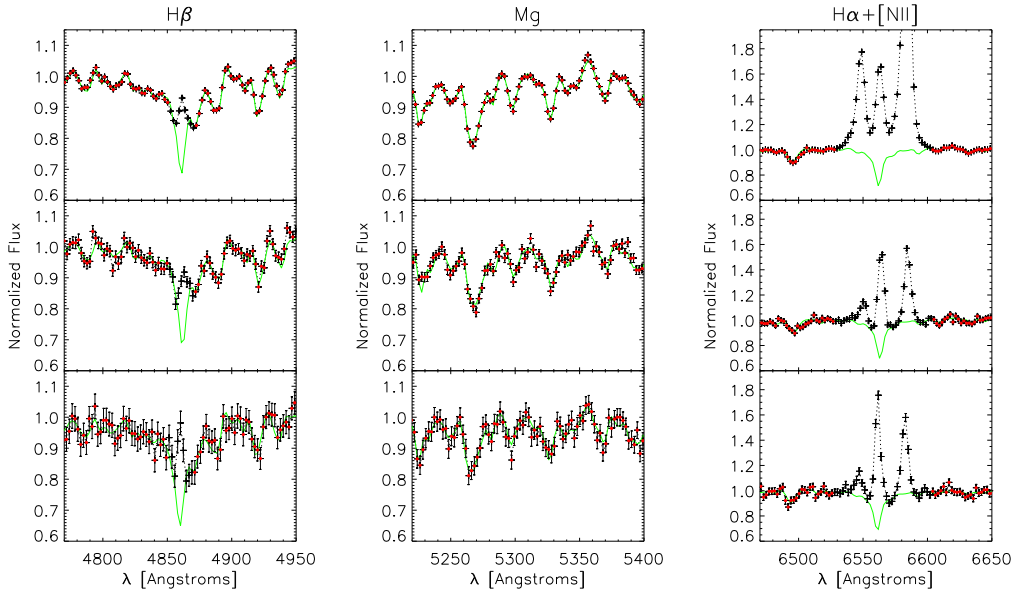


FIG. 3.— Continuum normalized spectra around the $H\beta$, $MgII$, and $H\alpha$ features for 3 regions having the highest, median and lowest (top, middle, bottom) S/N per resolution element in the continuum. Crosses show the data with error bars. Red crosses mark the data points used to fit the best linear combination of stellar templates (green solid line). Black crosses were masked in the fit due to the presence of nebular emission.

4.3. *HST* NICMOS Paschen- α Data

The center of NGC 5194 was imaged in Pa α by Scoville et al. (2001) using HST+NICMOS. A 3×3 mosaic covering the central $186'' \times 188''$ of the galaxy was imaged using the F187N and F190N narrow-band filters, sampling the Pa α line and the neighboring stellar continuum respectively. In this work we use this continuum subtracted Pa α image to measure emission line fluxes to check the validity of our dust extinction correction. The data reduction, mosaicking, flux calibration and continuum subtraction are described in Scoville et al. (2001) and Calzetti et al. (2005). The Pa α image overlaps completely with the VIRUS-P pointing shown in Figure 1.

5. MEASUREMENT OF EMISSION LINE FLUXES

We estimate the current Σ_{SFR} for each region by means of the $H\alpha$ nebular emission luminosity. In this section we describe the methods used to separate the emission lines coming from ionized gas from the underlying stellar spectrum, measure emission line fluxes, and estimate the dust extinction in each region using the $H\alpha/H\beta$ ratio.

5.1. Photospheric Absorption Lines and Continuum Subtraction

In galaxy spectra, both the $H\alpha$ and $H\beta$ emission lines sit on top of strong Balmer absorption lines characteristic of the photospheric stellar spectrum of young stars. Removing the contribution from these absorption lines is essential in order to estimate properly the emission line flux.

We use a linear combination of stellar template spectra to fit the absorption line spectrum of each region. The templates are high S/N, high resolution, continuum normalized spectra of a set of 18 stars from the Indo-U.S. Library of Coudé Feed Stellar Spectra (Valdes et al. 2004).

Stars were chosen to span a wide range in spectral types and metallicities (A7 to K0, and $[Fe/H]$ from -1.9 to 1.6).

The resolution of the templates is degraded to match the VIRUS-P 5.0\AA spectral resolution. For each of the 735 regions, we mask the parts of the galaxy spectrum affected by emission lines and sky subtraction residuals from bright sky lines. The continuum at each wavelength is estimated using an iterative running median filter, and used to normalize the observed spectrum.

We use this masked, continuum normalized spectrum to fit the best linear combination of stellar templates for each region. Figure 3 shows the best-fitted template combinations in regions centered in $H\beta$, $Mg\ b$, and $H\alpha$ for 3 regions in the galaxy. The bottom, middle and upper panels correspond to fibers with the lowest, median and highest S/N in their spectra respectively. For all 735 regions we obtain excellent fits to the underlying stellar spectrum. Figure 3 shows the importance of taking into account the effect of photospheric Balmer absorption lines when measuring $H\alpha$ and $H\beta$ fluxes. Ignoring the presence of the absorption features can introduce serious underestimations of the emission line fluxes. For $H\alpha$ this effect can account for underestimations of up to 100% as will be shown in §10.

The best-fitted linear combination of stellar templates is scaled by the galaxy continuum and subtracted from the original spectrum in order to produce pure nebular emission line spectra for all fibers. Figure 4 shows the nebular spectrum of the same regions shown in Figure 3. After subtracting the stellar light, we are able to identify most well known emission features in galaxy spectra. $H\beta$, $[OIII]\lambda\lambda 4959, 5007$, $[NII]\lambda\lambda 6548, 6584$, $H\alpha$ and $[SII]\lambda\lambda 6717, 6731$ are clearly seen in the spectra of all 735 regions. Visual inspection of Figure 4 shows that the $[NII]\lambda\lambda 6548, 6584/H\alpha$ ratio can change drastically from region to region. This effect can introduce systematic biases in narrow-band measured $H\alpha$ fluxes if the ratio

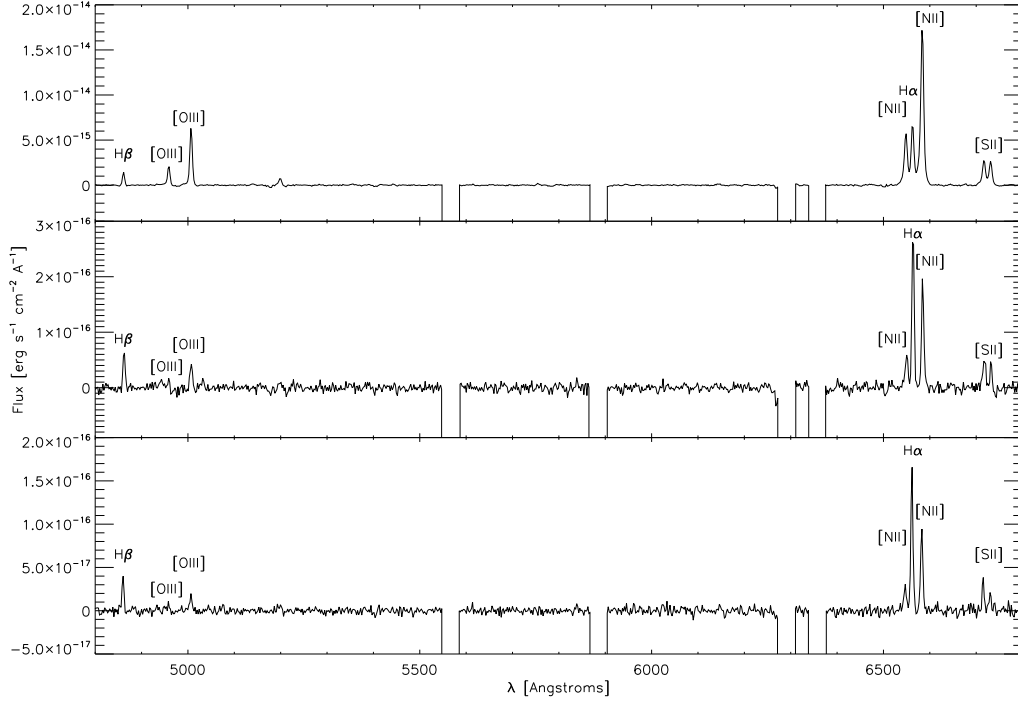


FIG. 4.— Nebular emission spectrum of the same regions shown in Figure 3, obtained by subtracting the best-fitted linear combination of stellar templates from the observed spectrum. Masked parts of the spectra correspond to the regions around strong night sky emission lines showing background subtraction residuals.

is assumed to be constant across the disk (Calzetti et al. 2005; Kennicutt et al. 2007). This issue will be discussed in detail in §10.

5.2. Emission Line Fluxes

We measure emission line fluxes by independently fitting $H\beta$, the $H\alpha$ -[NII] $\lambda\lambda, 6548, 6584$ complex, and the [SII] $\lambda\lambda, 6717, 6731$ doublet. Although the lines in the $H\alpha$ -[NII] complex are clearly resolved in our spectra, their wings show some level of overlap so we used a 3 Gaussian component model to fit these lines. Similarly a 2 Gaussian component model was used to fit the [SII] doublet. $H\beta$ was fitted using a single Gaussian. These fits provide the total flux and its uncertainty of all the above lines for the 735 regions. All lines are detected with a significance higher than 3σ in all fibers. We measure a median and lowest S/N over all fibers of 109 and 15 for $H\alpha$, 29 and 4 for $H\beta$, 49 and 13 for [NII] $\lambda 6584$, and 32 and 5 for [SII] $\lambda 6717$. Emission line fluxes of all lines for all fibers are given in Table 1, available in the electronic version of this paper.

5.3. Extinction Correction from the Balmer Decrement

The observed spectra is affected by differential extinction due to the presence of dust in the ISM of both NGC 5194 and the Milky Way. Before attempting to estimate SFRs from $H\alpha$ fluxes, these have to be corrected for dust extinction. Failing to do so can introduce underestimations in the SFR of up to factors of ~ 10 in the regions we are studying. The Balmer line ratio $H\alpha/H\beta$, as will be shown below, provides a good estimate of the dust extinction at the wavelength of the $H\alpha$ line.

Assuming an intrinsic $H\alpha/H\beta$ ratio of 2.87 (Osterbrock & Ferland 2006), the observed ratio provides the extinction at the wavelength of $H\alpha$ through the following equation,

$$A_{H\alpha} = -2.5 \log \left[\frac{[H\alpha/H\beta]_{obs}}{2.87} \right] \left(\frac{1}{1 - k(H\alpha)/k(H\beta)} \right) \quad (2)$$

where $[H\alpha/H\beta]_{obs}$ is the observed line ratio and $k(\lambda)$ is the extinction law. We assume a foreground MW extinction law as parameterized by Pei (1992). SMC and LMC laws were also tested (also using the Pei 1992, parametrization), and no significant change was observed in the deduced extinction values (these 3 extinction laws are practically identical at these wavelengths). To correct for Galactic extinction towards NGC 5194 we use a value of $A_B = 0.152$, taken from Schlegel et al. (1998).

In order to test the reliability of our Balmer decrement extinction values, we compare our corrected $H\alpha$ fluxes to corrected Pa α fluxes. The hydrogen recombination Pa α line at $1.87\mu\text{m}$, although one order of magnitude fainter than $H\alpha$, is very weakly absorbed by dust, and hence provides an unbiased estimate of the intrinsic SFR even in highly extinguished regions (Scoville et al. 2001). Most recent studies of spatially resolved star formation in nearby disk galaxies use recipes to account for dust obscured star formation which are ultimately linked to a calibration based on Pa α (Calzetti et al. 2005; Kennicutt et al. 2007; Bigiel et al. 2008; Leroy et al. 2008). In particular, Calzetti et al. (2005) finds a tight linear correlation between the $24\mu\text{m}$ luminosity of star forming regions in

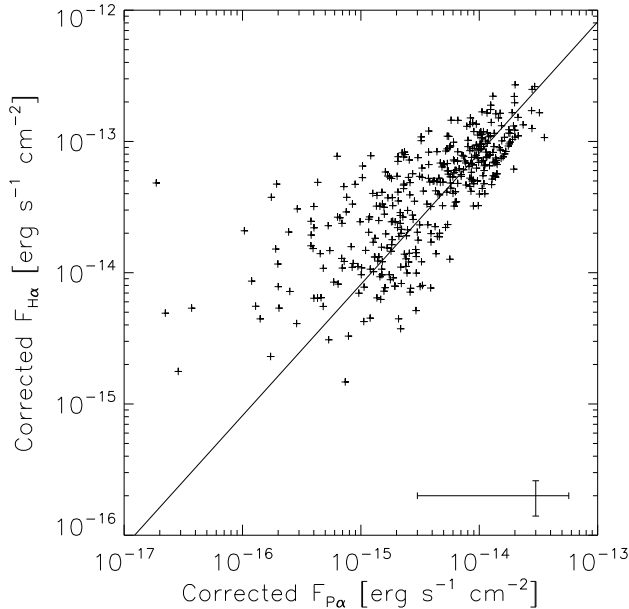


FIG. 5.— $H\alpha$ versus $P\alpha$ fluxes of all regions showing 5σ detections of $P\alpha$ emission in the NICMOS narrow-band image. Fluxes are corrected for dust extinction using the Balmer decrement derived values. The solid line shows the $H\alpha/P\alpha=8.15$ ratio predicted by recombination theory. Median error bars for the corrected fluxes are shown.

NGC 5194 and their $P\alpha$ luminosities, providing justification for the use of linear combinations of $24\mu\text{m}$ fluxes with either $H\alpha$ or UV fluxes to estimate the intrinsic SFR in the other mentioned works. In our case, if the extinction corrected $H\alpha$ fluxes linearly correlate with the corrected $P\alpha$ fluxes, following the intrinsic line ratio expected from recombination theory, then we can confirm that our extinction values have been properly estimated. In that case we can do without the IR data, and apply an extinction correction to the measured $H\alpha$ fluxes which is solely based in the optical spectra.

We measure $P\alpha$ fluxes for all 735 regions in the NICMOS F187N continuum subtracted narrow-band image (see §4.1), using apertures matching the size of the VIRUS-P fibers. Figure 5 shows extinction corrected $P\alpha$ versus $H\alpha$ fluxes for all regions showing 5σ detections of $P\alpha$ emission in the NICMOS narrow-band image. Both lines have been corrected using the Balmer decrement derived extinction, and a MW extinction law. The solid line in Figure 5 shows the theoretical $H\alpha/P\alpha=8.15$ ratio taken from Osterbrock & Ferland (2006). The observed line ratios are in agreement with the theoretical value, and the scatter can be attributed mostly to measurement errors. This confirms that $H\alpha$ fluxes, once corrected for dust obscuration using the Balmer decrement derived extinction, can provide an unbiased measure of the intrinsic SFR in the disks of normal face-on spirals.

6. MEASUREMENT OF GAS MASS SURFACE DENSITIES

In order to measure the atomic and molecular gas surface density at the position of each of the 735 regions under study, we measure integrated intensities in the THINGS 21 cm and the BIMA SONGS CO J=1-0 maps,

and translate them into gas surface densities using the calibrations presented below. The intensities are measured over an area equal to the beam size of each map. At each of the 735 fiber positions we perform aperture photometry on the 21 cm and CO maps, and measure the integrated gas intensity in apertures of effective radius $r_{\text{eff}}=\sqrt{ab}/2$, where a and b are the major and minor axis of the beam of each map. This translates in an effective aperture diameter of $5.7''$ and $5.4''$ for the 21 cm and CO maps respectively, which is well matched to the VIRUS-P spatial resolution which is set by the convolution of a $4.3''$ diameter fiber and a $2''$ FWHM seeing disk.

To convert the 21 cm intensities in atomic hydrogen column densities we use the following relation adapted from Walter et al. (2008),

$$N_{HI} = 1.823 \times 10^{18} \left(\frac{T_B}{\text{K km s}^{-1} \text{ sr}} \right) \text{ cm}^{-2} \quad (3)$$

where T_B is the velocity integrated surface brightness temperature in the 21 cm map. To convert the CO J=1-0 intensities to H_2 column densities we use the CO to H_2 conversion factor X_{CO} from Bloemen et al. (1986) so,

$$N_{H_2} = 2.8 \times 10^{20} \left(\frac{T_b}{\text{K km s}^{-1} \text{ sr}} \right) \text{ cm}^{-2} \quad (4)$$

where T_B is the velocity integrated surface brightness temperature in the CO J=1-0 map. The X_{CO} factor used here was chosen for consistency with Kennicutt et al. (2007), and differs from the $X_{CO} = 2.0 \times 10^{20} (\text{K km s}^{-1})^{-1}$ factor used by Bigiel et al. (2008). Current uncertainties in X_{CO} are of the order of a factor of 2, and the true value depends on assumptions about the dynamical state of GMCs (Blitz et al. 2007). In any case, using a different X_{CO} can only introduce an offset in the normalization of the SFL and should not change its observed shape.

Finally, the atomic and molecular gas surface densities are derived from the column densities using the following relations,

$$\Sigma_{HI} = m_H N_{HI} \cos i \quad (5)$$

$$\Sigma_{H_2} = 2m_H N_{H_2} \cos i \quad (6)$$

where m_H is the hydrogen atom mass and $i = 20^\circ$ is the inclination of NGC 5194 as measured by Tully (1974). These correspond to hydrogen gas surface densities, and should be multiplied by a factor ~ 1.36 to account for the mass contribution of helium and heavier elements.

7. PHOTOIONIZATION AND SHOCK-HEATING BY THE CENTRAL AGN

The center of NGC 5194 hosts a weak active nucleus. The emission-line ratios in the narrow-line region around the AGN are consistent with those of typical Seyfert nuclei (Bradley et al. 2004, and references therein). X-ray *Chandra* observations show the nucleus and two extended emission components extending $\sim 15''$ North and $\sim 7''$ South of it (Terashima & Wilson 2001). Bipolar extended radio emission spatially coincident with the X-ray emission, as well as weak jet with a position angle of 158°

connecting the nucleus with the southern radio lobe was observed by Crane & van der Hulst (1992) and further confirmed by Bradley et al. (2004). All the observations are consistent with the gas in the inner nuclear region ($r < 1''$) being dominantly photoionized by the central AGN, and the outer parts showing extended emission, arising from shock-heating by a bipolar outflow.

For the purpose of constructing the SFL, we want to exclude regions whose main source of ionization is not UV flux coming from massive star-formation. Regions in which the gas is photoionized by the AGN or shock-heated by the jet will emit in $H\alpha$ and mimic star-formation.

In order to identify these regions we use emission-line ratio diagnostics commonly used to distinguish normal from active galaxies (Veilleux & Osterbrock 1987; Kewley et al. 2001). Figure 6 shows the extinction corrected $[NII]\lambda 6584/H\alpha$ versus $[OIII]\lambda 5007/H\beta$ line ratios for all the regions. The solid and dotted lines mark the theoretical threshold separating AGNs from star-forming galaxies proposed by Kewley et al. (2001) and the ± 0.1 dex uncertainty in their modeling. To avoid the rejection of regions unaffected by AGN contamination which scatter above the threshold, we impose a double criteria. We flag as “AGN affected”, all the region lying above the threshold, and at an angular distance of less than $15''$ (600 pc) from the nucleus of the galaxy. Filled triangles in Figure 6 correspond to the 17 regions complying with both criteria. Open diamonds correspond then to the 718 regions unaffected by AGN contamination we will use to construct the SFL. Notice that none of these regions lie

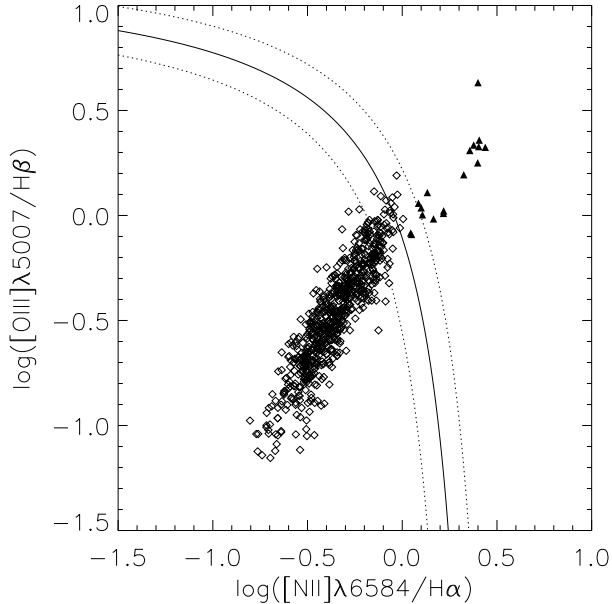


FIG. 6.— $[NII]\lambda 6584/H\alpha$ versus $[OIII]\lambda 5007/H\beta$ line ratio for the 735 regions. The solid line marks the theoretical threshold of Kewley et al. (2001) separating AGNs from star-forming galaxies. Dotted lines mark the ± 0.1 dex uncertainty in the threshold modeling. The 17 regions above the threshold and having angular distances to the galaxy nucleus of $< 15''$ are flagged as “AGN affected” and are shown as filled triangles. Open diamonds show the 718 regions unaffected by AGN contamination used to construct the SFL.

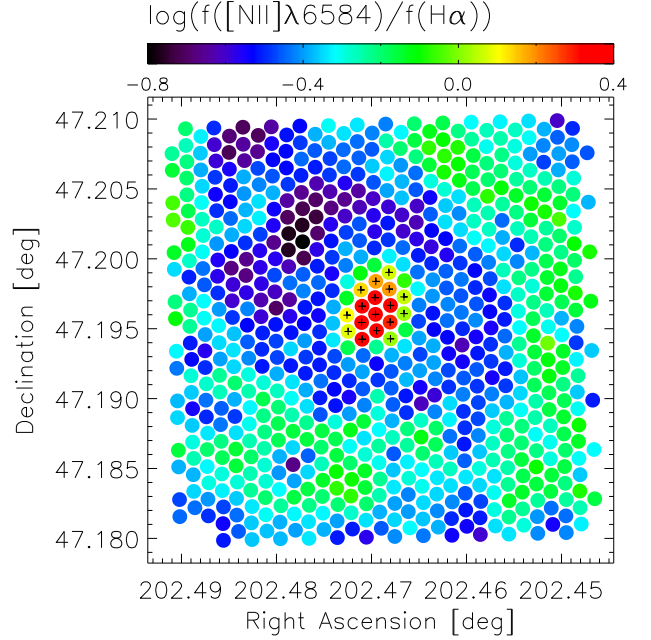


FIG. 7.— Map of the $[NII]\lambda 6584/H\alpha$ emission line ratio in the central region of NGC 5194. Regions flagged as “AGN affected” are marked by black crosses.

above the $+0.1$ dex model uncertainty dotted line, and that the ones lying above the threshold seem to follow the same sequence traced by the regions unaffected by AGN contamination below it. These fibers showing high line ratios but not associated with the central AGN fall in the inter-arm regions of the galaxy, and have a spectrum that is dominated by the DIG (§8).

Figure 7 shows a map of the $[NII]\lambda 6584/H\alpha$ line ratio. Regions flagged as “AGN affected” are marked with black crosses. It can be seen that they have high emission-line ratios typical of AGN, and that they fall in a region which is spatially coincident with the extended radio and X-ray emission observed around the nuclei. The “AGN affected” region is elongated in a similar direction to the measured $PA=158^\circ$ of the radio jet (Crane & van der Hulst 1992; Bradley et al. 2004; Terashima & Wilson 2001). Figure 7 clearly shows the enhanced line ratio in the inter-arm regions of NGC 5194. These high ratios originate in the DIG of the galaxy and are discussed in the following Section.

8. CONTRIBUTION FROM THE DIFFUSE IONIZED GAS AND CALCULATION OF SFR SURFACE DENSITIES

If we were to calculate Σ_{SFR} using the extinction corrected $H\alpha$ flux observed on each region, we would be working under the assumption that all the emission observed in a given line of sight towards the galaxy has an origin associated with ionizing flux coming from localized star-formation in the same region. This is not necessarily true in the presence of a diffuse ionized component in the ISM of the galaxy. The role of the diffuse ionized gas (DIG, a.k.a. warm ionized medium, WIM) as an important component of the ISM of star-forming disk galaxies in the local universe has been properly established during the last two decades (e.g. see reviews by Mathis 2000 and Haffner et al. 2009). The existence of

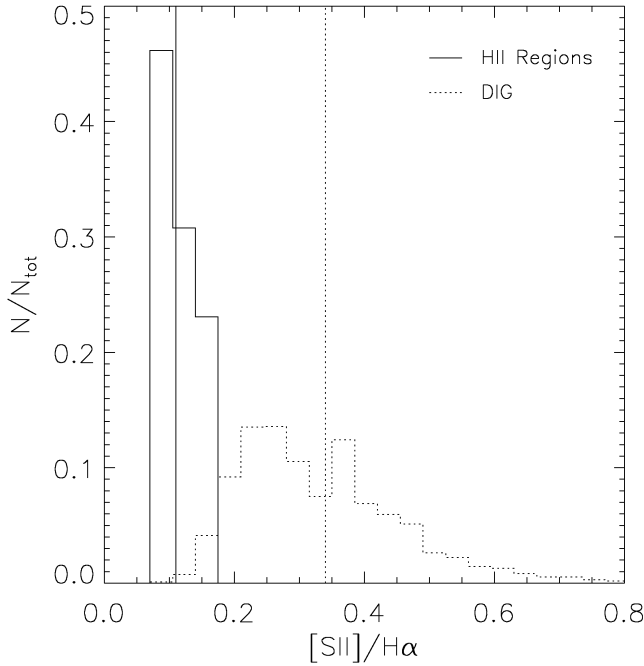


FIG. 8.— Histogram of the $[SII]/H\alpha$ of H II regions (solid) and pointings towards DIG (dotted) in the Milky Way as measured by WHAM (Madsen et al. 2006). Vertical lines mark the mean values for the two distributions.

a significant component of extra-planar ionized hydrogen in a galaxy requires that a fraction of the ionizing Lyman continuum photons generated in star forming regions in the disk escapes and travels large distances of the order of kiloparsecs before ionizing neutral hydrogen at large heights above the disk. These distances are one order of magnitude larger than the Strömgren radii associated with the most massive O stars, and the ionizing flux is thought to escape through super-bubbles in a complex hydrogen density and ionization distribution created by supernovae, stellar winds, and large scale ionization by OB associations (e.g. Dove et al. 2000).

Under these conditions a hydrogen atom emitting an $H\alpha$ photon observed to come in the direction of a certain region of the galaxy is not necessarily required to have been ionized by locally produced UV photons in the same region. Hence the $H\alpha$ flux measured in each region is the sum of the flux coming from locally star-forming H II regions in the disk, and a contribution from the DIG. In order to properly estimate Σ_{SFR} and the spatially resolved SFL we need to separate and subtract the DIG contribution from the observed $H\alpha$ fluxes.

Low-ionization line ratios like $[NII]\lambda 6584/H\alpha$ and $[SII]\lambda 6717/H\alpha$ (hereafter $[SII]/H\alpha$) are observed to be greatly enhanced in the DIG, as compared to the typical values observed in H II regions (Reynolds 1985; Hoopes & Walterbos 2003). Recent results from The Wisconsin $H\alpha$ Mapper (WHAM⁵) sky survey by Madsen et al. (2006) show that H II regions in the Milky Way have a typical $([SII]/H\alpha)_{HII}=0.11$ with a small rms scatter from region to region of only $\Delta([SII]/H\alpha)_{HII}=0.03$. On the other hand, high galac-

tic latitude pointings sampling the DIG component show a mean $([SII]/H\alpha)_{DIG}=0.34$, with a large scatter from pointing to pointing of $\Delta([SII]/H\alpha)_{DIG}=0.13$. Figure 8 shows a histogram of the $[SII]/H\alpha$ line ratios taken from Madsen et al. (2006) for H II regions and the DIG as measured by WHAM. It can be seen that the $[SII]/H\alpha$ ratio provides a very useful tool to separate the contribution from the DIG and the disk H II regions in our spectra. The $[NII]/H\alpha$ ratio, while still enhanced in the DIG as can be clearly seen in Figure 7, shows a much larger scatter both for H II regions and pointings towards the DIG, and does not provide such a clean separation as the $[SII]/H\alpha$ ratio (see Figure 21 in Madsen et al. (2006)).

We model the measured $H\alpha$ flux of each region as the sum of a contribution from H II regions plus a contribution from the DIG, so

$$\begin{aligned} f(H\alpha) &= f(H\alpha)_{HII} + f(H\alpha)_{DIG} \\ &= C_{HII}f(H\alpha) + C_{DIG}f(H\alpha) \end{aligned} \quad (7)$$

where C_{HII} is the fraction of the total flux coming from local star-forming regions in the disk, and $C_{DIG}=(1-C_{HII})$. The observed $[SII]/H\alpha$ ratio is then given by,

$$\frac{[SII]}{H\alpha} = Z' \left[C_{HII} \left(\frac{[SII]}{H\alpha} \right)_{HII} + C_{DIG} \left(\frac{[SII]}{H\alpha} \right)_{DIG} \right] \quad (8)$$

where $Z' = Z/Z_{MW}$ is the metallicity of NGC 5194 normalized to the Milky Way value. Figure 9 shows the observed $[SII]/H\alpha$ ratio as a function of extinction corrected $H\alpha$ flux. The left axis shows C_{HII} calculated assuming a value of $Z' = 1.0/1.5$. Bresolin et al. (2004)

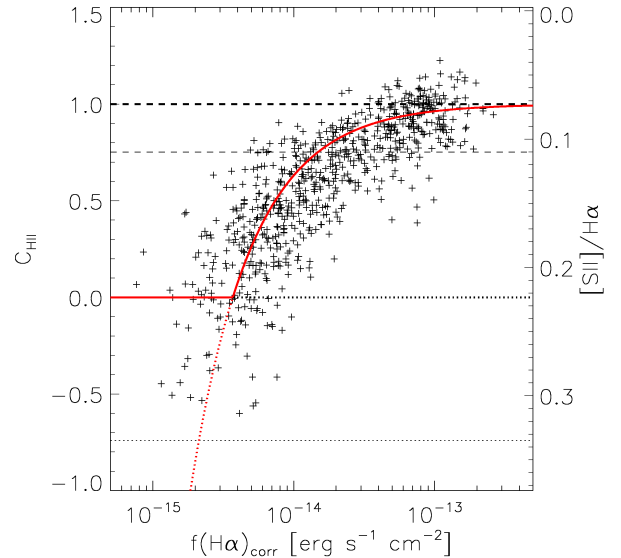


FIG. 9.— Observed $[SII]/H\alpha$ emission line ratio for the 718 regions unaffected by AGN contamination. The thin dashed and dotted lines show the mean ratio observed in H II regions and pointings towards the DIG in the Milky Way respectively. The thick dashed and dotted lines show the former ratios scaled down by a factor $Z' = 1.0/1.5$. The left axis shows the fraction of the flux coming from H II regions in the disk given by Equation 8. The solid red curve shows the DIG correction applied to the data given by Equation 9, and the continuation of the function to fluxes lower than f_0 is marked by the dashed red line.

⁵ <http://www.astro.wisc.edu/wham/>

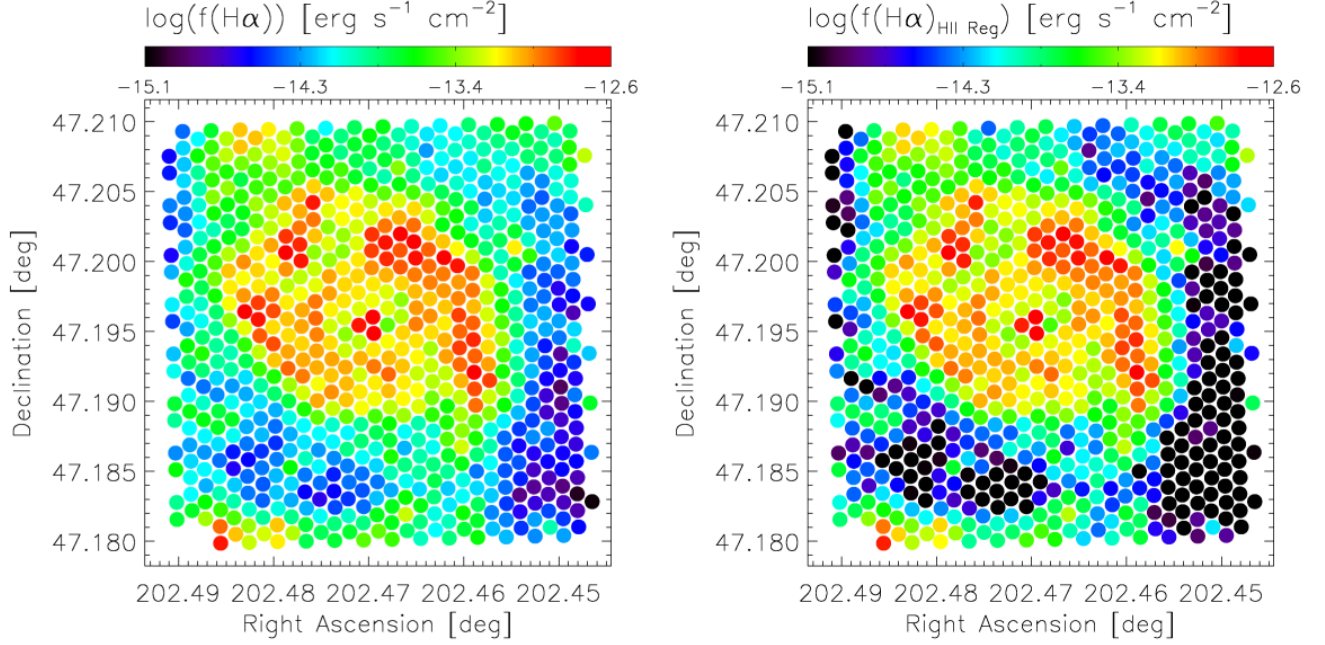


FIG. 10.— *Left:* Map of the extinction corrected $\text{H}\alpha$ nebular emission flux in the central $4.1 \times 4.1 \text{ kpc}^2$ of NGC 5194. *Right:* Same map after removing the DIG contribution to the $\text{H}\alpha$ emission line flux, that is, showing only the flux coming from H II regions in the disk of NGC 5194.

measured the oxygen and sulfur abundance gradient in NGC 5194 using multi-object spectroscopy of 10 H II regions spanning a large range in radii. Integrating his best-fitted oxygen abundance gradient out to a radius of 4.1 kpc provides an mean $12+\log(\text{O}/\text{H})=8.68$, which is 1.55 times lower than the solar oxygen abundance measured by Grevesse et al. (1996). Although a large scatter is observed in the literature for both the solar oxygen abundance and the oxygen abundance in Milky Way H II regions (Grevesse et al. 1996; Allende Prieto et al. 2001; Shaver et al. 1983; Deharveng et al. 2000), it can be seen in Figure 9 that using a factor of 1.5 implies that the brightest $\text{H}\alpha$ emitting regions in NGC 5194 are completely dominated by emission from H II regions in the disk, having $C_{\text{HII}} \sim 1$ with a scatter that is consistent with the intrinsic scatter of 0.03 measured in the Milky Way by Madsen et al. (2006). These brightest regions trace the spiral structure of the galaxy and are expected to be H II region dominated since on high star-formation regions the disk should outshine the DIG by many orders of magnitude.

There is a clear correlation between C_{HII} and the $\text{H}\alpha$ flux. The observed trend is consistent with the DIG dominating the spectrum of fainter $\text{H}\alpha$ regions, and the H II regions in the disk outshining the DIG in the brightest ones. The scatter is large mostly because of intrinsic scatter in the line ratio (see Figure 8). In order to compute a robust DIG correction, we fit the C_{HII} values using the simple functional form,

$$C_{\text{HII}} = 1.0 - \frac{f_0}{f(\text{H}\alpha)}; \quad (\text{for } f(\text{H}\alpha) > f_0) \quad (9)$$

where $f_0 = 3.69 \times 10^{-15} \text{ erg s}^{-1} \text{ cm}^{-2}$ is the flux at which the DIG contributes 100% of the emission, and hence $C_{\text{HII}} = 0$ for $f(\text{H}\alpha) \leq f_0$. The correction is

shown as the red solid line in Figure 9. We multiply the extinction corrected $\text{H}\alpha$ fluxes by the above correction factor in order to remove any contribution from the DIG in NGC 5194. It is worth noting that using Equation 9 to remove the DIG is equivalent to subtracting a constant DIG flux value f_0 for all regions with $f(\text{H}\alpha) > f_0$ (the large majority of the regions). Hence, the line ratio distribution presented in Figure 9 is very well fitted by a flat DIG component.

Figure 10 presents maps of the extinction corrected $\text{H}\alpha$ emission line flux before and after the DIG correction is applied. It can be seen clearly how the $\text{H}\alpha$ emission traces the spiral pattern of star-formation. The correction leaves the $\text{H}\alpha$ flux coming from the brightest star-forming regions practically unchanged, while removing the contribution from the DIG which dominates the observed spectrum in the inter-arm regions of the galaxy. The latter can also be appreciated in Figure 7, which shows an enhanced $[\text{NII}]/\text{H}\alpha$ ratio typical of the DIG in the inter-arm regions, and normal H II region ratios throughout the spiral arms.

Integrating over the complete observed area, the DIG contributes only 11% of the total $\text{H}\alpha$ flux. Previous photometric measurements of the diffuse ionized fraction in nearby spiral galaxies, including NGC 5194, yield median diffuse fractions of $\sim 50\%$ (e.g. Ferguson et al. 1996; Hoopes et al. 1996; Greenawalt et al. 1998; Thilker et al. 2002; Oey et al. 2007). These studies are performed either by masking of H II regions or by discrete H II region photometry in $\text{H}\alpha$ narrow-band images. Although it will be seen in §10 that the assumption of a constant $[\text{NII}]/\text{H}\alpha$ ratio throughout the galaxy used to correct the narrow-band images in all the above studies can introduce overestimations of the DIG $\text{H}\alpha$ brightness of up to 40%, this effect is small, and cannot account for the difference between our diffuse fraction and the typical

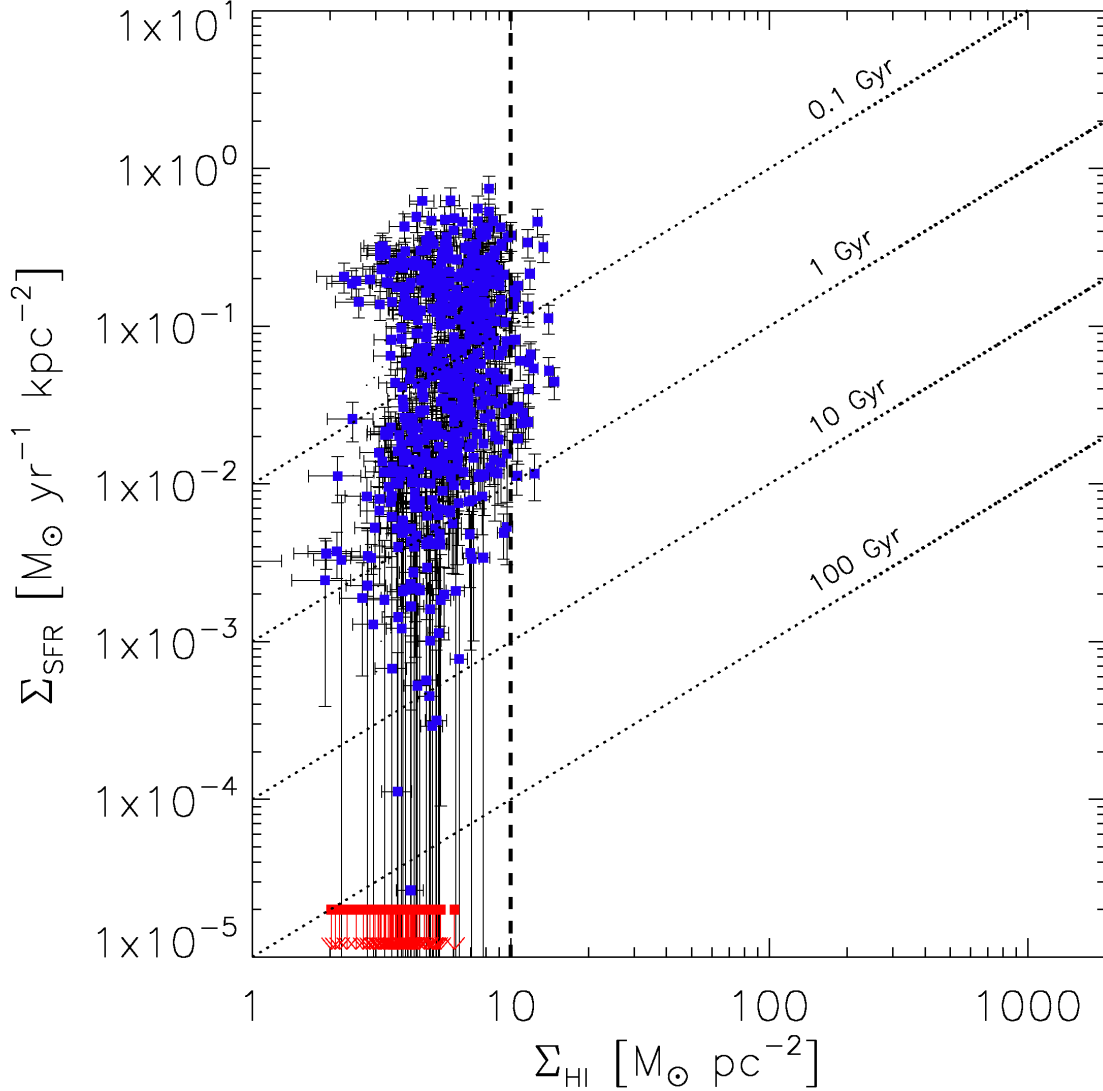


FIG. 11.— Atomic gas surface density versus SFR surface density for the 718 regions unaffected by AGN contamination. Upper limits in Σ_{SFR} correspond to regions with $C_{HII} = 0$. The vertical dashed line marks the HI to H₂ transition threshold at 10 $M_{\odot} \text{pc}^{-2}$. The diagonal dotted lines correspond to constant depletion timescales $\tau = \text{SFE}^{-1}$ of 0.1, 1, 10 and 100 Gyr.

values found in the literature. The difference is most likely due to the fact that our observations are limited to the highly molecular, and hence strongly star-forming central part of the galaxy. Our measured diffuse ionized fraction is then only a lower limit to the DIG contribution over the whole galaxy, since at larger radii the relative contribution from H II regions is expected to significantly decrease. Though the DIG contribution to the integrated H α luminosity in the central region of NGC 5194 could be small, on the small scales sampled by the VIRUS-P fibers the DIG can account for 100% of the observed H α flux, especially in between the spiral arms where H II regions are rare. Given the clear dependence of the above correction with H α flux, failing to correct for this effect introduces a bias in the SFL towards shallower slopes.

The corrected H α emission-line fluxes are transformed into H α luminosities using the assumed distance to NGC 5194 of 8.2 Mpc. Since the DIG is suspected to arise from

UV photons escaping star forming regions in the disk, not accounting for these photons should introduces a systematic underestimation of the SFR. The challenge resides in our inability to tell from where in the disk these UV photons come from. To ameliorate this problem, we scale the H α luminosities by a factor of 1.11, which is equivalent to assuming that the UV photons ionizing the DIG were originated in the star-forming regions in the disk proportionally to their intrinsic UV luminosities. These scaled luminosities ($L_{\text{corr}}(\text{H}\alpha)$) are used to estimate the SFR for each of the 718 regions. We use the calibration presented in Kennicutt (1998a), for which the SFR is given by,

$$\text{SFR} [M_{\odot} \text{yr}^{-1}] = 7.9 \times 10^{-42} L_{\text{corr}}(\text{H}\alpha) [\text{erg s}^{-1}] \quad (10)$$

The above calibration assumes a Salpeter IMF over the range of stellar masses 0.1-100 M_{\odot} . To convert to the

Kroupa-type two-component IMF used in Bigiel et al. (2008), the SFR must be multiplied by a factor of 0.63.

The SFRs for individual regions are then converted to SFR surface densities (Σ_{SFR}). Following Kennicutt et al. (2007), we divide the SFR by the projected area on the sky of the $4.3''$ (172 pc) diameter regions sampled by each fiber on the IFU, and multiply it by a factor of $\cos(20^\circ)$ to account for the inclination of NGC 5194 (Tully 1974).

9. THE SPATIALLY RESOLVED STAR FORMATION LAW

The observed relations between Σ_{SFR} and the gas surface densities of different components of the ISM (Σ_{HI} , Σ_{H_2} , and Σ_{HI+H_2}) are presented in Figures 11, 12 and 13. Error bars in gas surface densities correspond to the 1σ uncertainties given in §4.1 and §4.2. Error bars in the SFR surface density include a series of uncertainties that we proceed to describe. First we consider the uncertainty in the observed $H\alpha$ fluxes. This comes from the fitting of the $H\alpha$ line described in §5.2, which was performed considering the observational error in the spectrum (obtained from the error maps described in §3). Second, the uncertainty in the dust extinction correction is included by propagating the fitting errors of the observed $H\alpha$ and $H\beta$ fluxes through Equation 2. Finally, in order to account for the error associated with the DIG correction, we introduce a 20% uncertainty in Σ_{SFR} , consistent with the median scatter of the points in Figure 9 around the correction used. All these uncertainties are summed in quadrature to account for the error bars in Σ_{SFR} . We do not consider errors in the flux calibration which are expected to be of $\sim 5\%$, nor in the CO to H_2 conversion factor. The latter is currently highly uncertain and might change by up to a factor of 2 depending on assumptions about the dynamical state of GMCs (Blitz et al. 2007). In any case, these two sources of systematic errors enter the SFL as multiplicative factors. Hence, they can only introduce a bias in the normalization of the SFL, and should not affect the fitted values of the slope and the intrinsic scatter.

From Figure 11 it is clear that Σ_{SFR} shows a very poor correlation with Σ_{HI} , since regions having similar atomic gas budgets can have star formation activities that differ by more than 3 orders of magnitude. We observe an evident saturation in the atomic gas surface density at $\Sigma_{HI} \approx 10 \text{ M}_\odot \text{pc}^{-2}$. Also, there is a slight inversion in the sense of the correlation at high Σ_{SFR} , associated with the central part of the galaxy due to the presence of a minimum in the HI profile (Bigiel et al. 2008). These HI “holes” are common in the centers of spiral galaxies, and in them the ISM is fully dominated by molecular hydrogen while the atomic gas is almost completely depleted. The saturation at $10 \text{ M}_\odot \text{pc}^{-2}$ has been previously observed by Wong & Blitz (2002) using azimuthally averaged data, and further confirmed to be a widespread phenomena in normal spirals by Bigiel et al. (2008) using 2D spatially resolved measurements. It is thought to be related to a threshold in surface density at which a phase-transition from atomic to molecular gas occurs in the ISM (Krumholz et al. 2009a). Given the lack of correlation between Σ_{HI} and Σ_{SFR} , we do not attempt to fit a atomic gas SFL. We restrict our analysis to the modeling of the molecular and total gas correlations with the star-formation activity. These correlations are

usually well described by a power-law function (Schmidt 1959; Kennicutt 1998b).

It has been established that the observed rms dispersion about a power-law in these SFLs is much larger than the observational uncertainties (Kennicutt 1998b; Kennicutt et al. 2007), implying the existence of significant intrinsic scatter of physical origin in the relations. However, previous works have not introduced this intrinsic scatter into the parameterization of the SFL, and authors restrict themselves to measure the scatter after fitting a power-law to the data. In this work, we incorporate the intrinsic scatter in the SFL, which we parameterize as:

$$\frac{\Sigma_{SFR}}{1 \text{ M}_\odot \text{yr}^{-1} \text{kpc}^{-2}} = A \left(\frac{\Sigma_{gas}}{100 \text{ M}_\odot \text{pc}^{-2}} \right)^N \times 10^{\mathcal{N}(0, \epsilon)} \quad (11)$$

where A is the normalization factor, N is the slope, and $\mathcal{N}(0, \epsilon)$ is a logarithmic deviation from the power-law, drawn from a normal distribution with zero mean and standard deviation ϵ . The value of ϵ corresponds to the intrinsic scatter of the SFL in logarithmic space. The factor $10^{\mathcal{N}(0, \epsilon)}$ can be interpreted as changes of physical origin in the star-formation efficiency for different regions. We chose a pivot value for the normalization of $100 \text{ M}_\odot \text{pc}^{-2}$, which is roughly at the center of the distribution of measured Σ_{gas} values, in order to minimize the covariance between the slope and the normalization. When comparing the normalization factors derived here with other fits found in the literature, this must be taken into account. Most works quote normalizations at $1 \text{ M}_\odot \text{pc}^{-2}$, while Bigiel et al. (2008) quotes normalizations at $10 \text{ M}_\odot \text{pc}^{-2}$.

Previous measurements of the spatially resolved SFL use different algorithms to fit a power-law to the data. Usually a linear regression in logarithmic space is performed, but methods differ in the treatment of error bars. Kennicutt et al. (2007) used a FITEXY algorithm (Press et al. 1989), which has the advantage of incorporating errors in both the ordinate and abscissa coordinates, although errors must be assumed to be symmetric in logarithmic space, which is not always the case. Bigiel et al. (2008) used an ordinary least-squares (OLS) bisector method (Isobe et al. 1990) giving the same weighting to every data point. Both methods have the disadvantage of not being able to incorporate upper limits in the minimization. Our data is mainly limited by the sensitivity of the CO intensity maps as can be seen in Figure 12, where 93 of the 718 regions unaffected by AGN contamination are undetected in CO and hence we can only provide upper limits for their molecular gas surface densities. This is also the case in the works mentioned above. As will be seen in §11, these upper limits contain important information regarding the slope of the spatially resolved SFL, and neglecting them biases the fits towards steeper slopes. We introduce and use a new method for fitting the SFL which is not affected by the above issues.

9.1. The Fitting Method

To fit our data we use a Monte Carlo (MC) approach combined with two-dimensional distribution comparison techniques commonly used in color-magnitude diagram

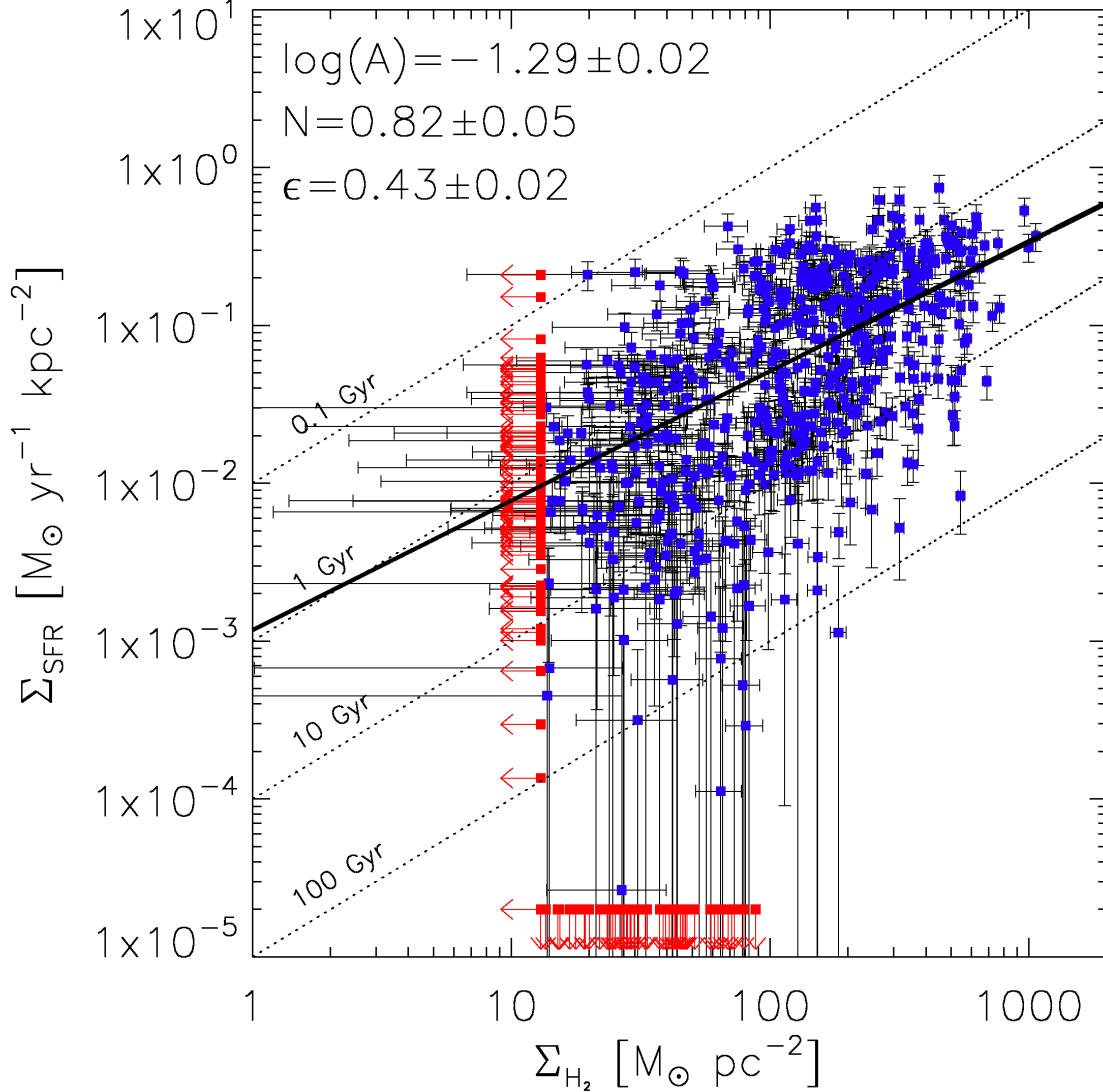


FIG. 12.— Molecular gas surface density versus SFR surface density for the 718 regions unaffected by AGN contamination. Upper limits in Σ_{SFR} correspond to regions with $C_{HII} = 0$. Upper limits in Σ_{H_2} correspond to regions with non-detection in CO at the 1σ level. The diagonal dotted lines correspond to constant depletion timescales $\tau = SFE^{-1}$ of 0.1, 1, 10 and 100 Gyr. Also shown is the best-fitted power law from the Monte Carlo method (black solid line), and the best-fitted parameters.

(CMD) fitting (Dolphin et al. 2001). Our method allows us to include the regions not detected in the CO map (including the ones with negative measured fluxes), incorporate the intrinsic scatter in the SFL as a free parameter, and perform the fitting in linear space, avoiding the assumption of log-normal symmetric errors. In the following, we describe our fitting method.

For any given set of parameters $\{A, N, \epsilon\}$, we generate 200 Monte Carlo realizations of the data. To create each realization, we take the measured values of Σ_{gas} as the true values and calculate the corresponding true Σ_{SFR} using Equation 11, drawing a new value from $\mathcal{N}(0, \epsilon)$ for each point in order to introduce the intrinsic scatter. Regions for which we measure negative CO fluxes are assumed to have $\Sigma_{gas} = \Sigma_{SFR} = 0$. In order to account for observational errors, data points are then offset in Σ_{SFR} and Σ_{gas} by random quantities given

by the observed measurement error for each data point. The uncertainty in Σ_{SFR} is largely dominated by the errors introduced in the dust extinction and DIG corrections. Since both corrections are multiplicative, we apply the random offsets as multiplicative factor drawn from a $\mathcal{N}(1, \sigma(\Sigma_{SFR})/\Sigma_{SFR})$ distribution. On the other hand, the error in Σ_{gas} is dominated by systematic offsets introduced during the combination and calibration of interferometric data. Accordingly, the random offsets in Σ_{gas} are introduced in an additive manner, using values drawn from a $\mathcal{N}(0, \sigma(\Sigma_{gas}))$ distribution. It is important to notice that while for plotting purposes, Figures 11, 12, and 13 show upper limits in Σ_{gas} and Σ_{SFR} , in the fitting procedure the measured values of these data-points are used together with their usually large error bars.

Having the observed data points and the large collection of realizations of the data coming from the model, we

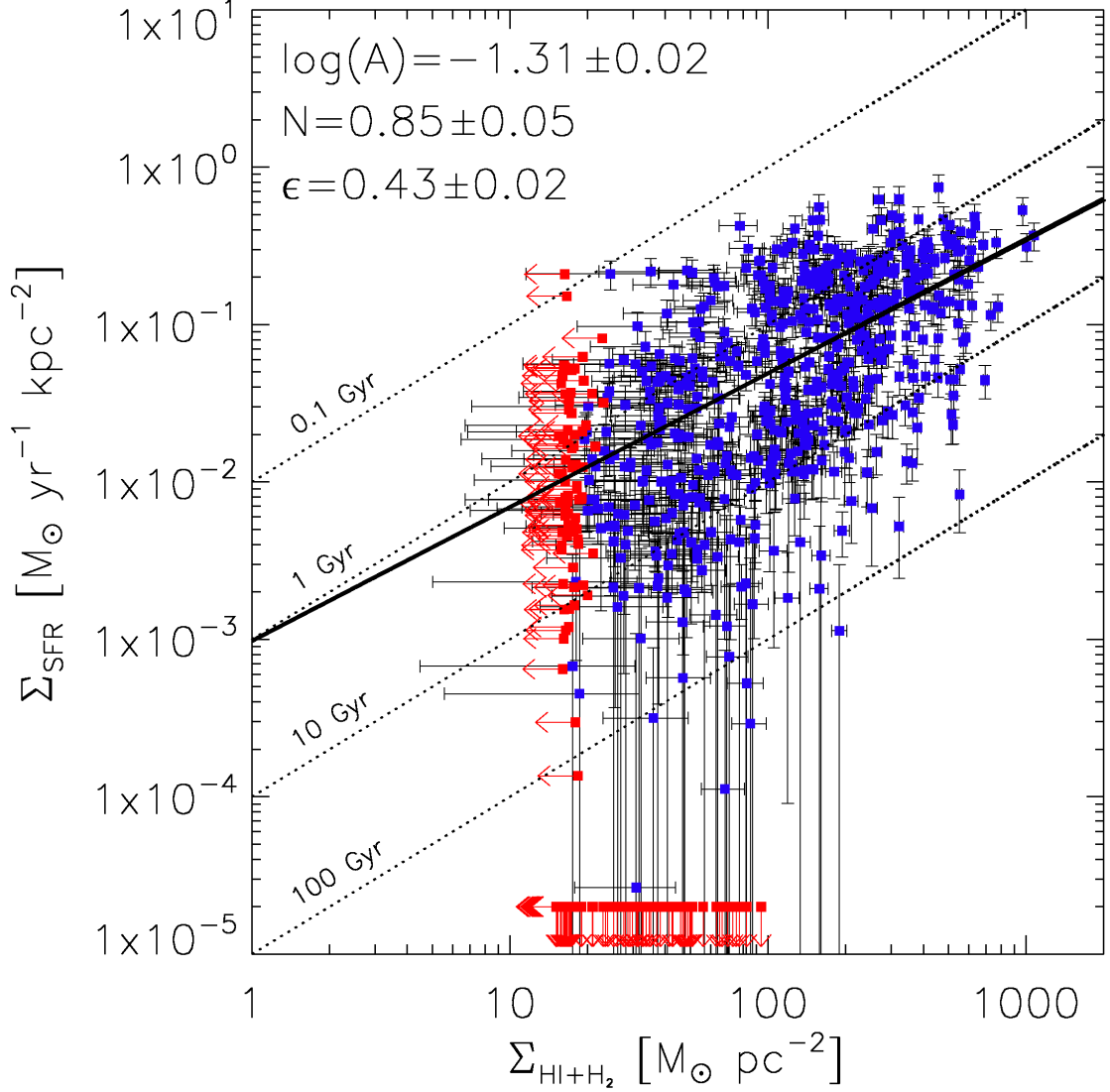


FIG. 13.— Total gas surface density versus SFR surface density for the 718 regions unaffected by AGN contamination. Upper limits in Σ_{SFR} correspond to regions with $C_{HII} = 0$. Upper limits in Σ_{HI+H_2} correspond to regions with non-detection in CO at the 1σ level. The diagonal dotted lines correspond to constant depletion timescales $\tau = SFE^{-1}$ of 0.1, 1, 10 and 100 Gyr. Also shown is the best-fitted power law from the Monte Carlo method (black solid line), and the best-fitted parameters.

need to compare the distribution of points in the Σ_{gas} - Σ_{SFR} plane in order to assess how well the model fits the data given the assumed parameters. To do so, we define a grid on the Σ_{gas} - Σ_{SFR} plane and count the number of data points falling on each grid element both in the data and in the 200 realizations. This method is adapted from Dolphin et al. (2001), and it is the equivalent to the construction of Hess diagrams used in CMD fitting. The grid covers all the observed data points, has a resolution of $\Delta\Sigma_{gas}=156 \text{ M}_\odot\text{pc}^{-2}$ and of $\Delta\Sigma_{SFR}=0.11 \text{ M}_\odot\text{yr}^{-1}\text{kpc}^{-2}$, and is shown in the left panel of Figure 14. A single extra grid element containing all the points in the Monte Carlo realizations falling outside the grid and zero observed data points is also included in the calculations below.

We average the number of points in each grid element for the 200 Monte Carlo realizations and call this “the

model”. In order to compare the model to the data we compute a χ^2 statistic of the following form:

$$\chi^2 = \sum_i \frac{(N_i - M_i)^2}{M_i} \quad (12)$$

Where the sum is over all the grid elements in the Σ_{gas} - Σ_{SFR} plane, N_i is the number of observed data points, and M_i is the number of model data points in the grid element i . We sample a large three dimensional grid in parameter space with a resolution of $\Delta\log(A)=0.018$, $\Delta N=0.036$, and $\Delta\epsilon=0.011$, centered around our best initial guesses for the different SFLs, and compute χ^2 for every combination of parameters in the cube.

To exemplify our method, the left panel in Figure 14 shows the observed molecular SFL in linear space, together with the best-fitted Monte Carlo model. Overlaid

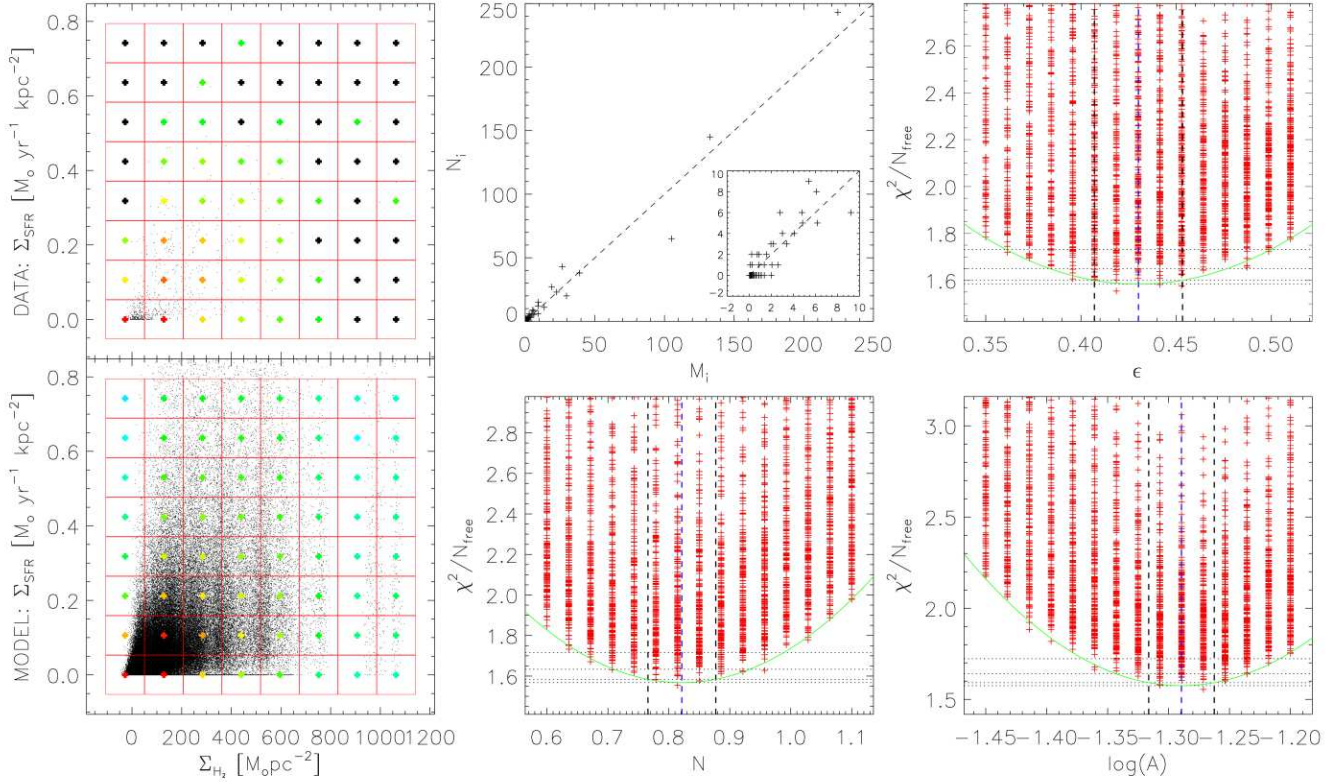


FIG. 14.— *Left:* The observed molecular SFL in linear space (top), together with the 200 Monte Carlo realizations of the data for the best-fitted parameters (bottom). The grid used to compare the model to the data is shown in red, and each box in the grid shows a cross, color-coded according to the number of points in the grid (with red corresponding to the highest value and black corresponding to zero). *Center-Top:* Number of data-points per grid elements in the model versus the data. *Center-Bottom and Right:* Reduced χ^2 for each of the three free parameter in the fit (A , N , and ϵ), marginalized over the other two parameters. Red crosses show the χ^2 obtained for each sampled combination of parameters. The best-fitted quadratic function to the minimum χ^2 is shown in green. The best-fitted χ^2 , together with the 1σ , 2σ , and 3σ levels are shown as horizontal dotted lines. The blue and black vertical dashed lines marks the best-fitted parameter and its 1σ uncertainty respectively.

are all the grid elements, color-coded according with the density of points inside each of them. The top central panel shows the number of points in each grid element in the model versus the data for the best-fitted model, in this plot, deviations from the dashed line contribute to the χ^2 statistic. Also shown is the χ^2 for each parameter, marginalized over the other two. The best-fitted value for each parameter is obtained by fitting a quadratic function to the minimum χ^2 at each parameter value sampled. Uncertainties at the 1σ , 2σ , and 3σ levels are also shown in the plots. Notice that the sampled set of parameters showing the minimum χ^2 is always within 1σ of the best-fitted value deduced from the quadratic function fitting.

Thorough testing of the fitting method was carried out. The number of Monte-Carlo simulations is high enough for consecutive runs of the algorithm on the same data to produce best-fitted values for the parameters that show a scatter of less than 0.1σ . The best-fitted parameters are somewhat sensitive to the chosen grid spacing in the linear $\Sigma_{gas}-\Sigma_{SFR}$ plane. Fitting of artificially generated data-sets drawn from known parameters, showed the grid resolution we use to be the best at recovering the intrinsic parameters with deviations from the true values of less than 0.5σ .

9.2. Fits to the Molecular and Total Gas Star Formation Laws

We applied our method to fit the observed SFL in both molecular gas and total gas. The best-fitted SFLs are shown as solid lines in Figures 12 and 13, where the best-fitted parameters are also reported. For the molecular gas SFL we measure a slope $N = 0.82 \pm 0.05$, an amplitude $A = 10^{-1.29 \pm 0.02}$, and an intrinsic scatter $\epsilon = 0.43 \pm 0.02$ dex. In the central part of NCG 5194 we are sampling a density regime in which the ISM is almost fully molecular, hence the total gas SFL closely follows the molecular SFL and shows very similar best-fitted parameters. For the total gas SFL we obtain a slope $N = 0.85 \pm 0.05$, an amplitude $A = 10^{-1.31 \pm 0.02}$, and an intrinsic scatter $\epsilon = 0.43 \pm 0.02$ dex.

Of great interest is the large intrinsic scatter observed in the SFL. A logarithmic scatter of 0.43 dex implies that the SFR in regions having the same molecular gas surface density can vary roughly by a factor of ~ 3 . This is very important to keep in mind when using the SFL as a star-formation recipe in theoretical models of galaxy formation and evolution. Results from this type of modeling should be interpreted in an statistical sense, and we must always remind ourselves that SFRs predicted for single objects can be off by these large factors. The bot-

tom left panel of Figure 14 is an striking reminder of the limitations involved in the use of SFLs as star-formation recipes in analytical and semi-analytical models. The large scatter observed is indicative of the existence of other parameters, besides the availability of molecular gas, which are important in setting the SFR.

As will be discussed in §11, the fact that we measure a slightly sub-linear SFL is consistent recent results by Bigiel et al. (2008) and Leroy et al. (2008), as well as with recent theoretical modeling by Krumholz et al. (2009b), but in disagreement with the significantly super-linear molecular and total gas SFLs measured in NGC 5194 by Kennicutt et al. (2007). Our results imply depletion times for the molecular gas of $\tau \approx 2$ Gyr, which is roughly a factor of ~ 100 longer than the typical free fall time of GMCs (McKee 1999). These low efficiencies, of the order of 1% per free-fall time, are observed in a large range of spatial scales and densities in different objects. It is seen all the way from HCN emitting clumps, infrared dark clouds, and GMCs in the Milky Way to the molecular ISM in large scales in normal spiral galaxies and starburst, and is consistent with models in which star-formation is regulated by supersonic turbulence in GMCs, induced by feedback from star-formation itself (Evans et al. 2009; Krumholz & Tan 2007).

10. BALMER ABSORPTION AND THE $N[\text{II}]/\text{H}\alpha$ RATIO, IMPLICATIONS FOR NARROW-BAND IMAGING

Narrow-band imaging is the most widely used method for conducting spatially resolved measurements of the $\text{H}\alpha$ emission line in nearby galaxies. Images taken with a narrow-band filter centered at $\text{H}\alpha$, and either a broad-band or off-line narrow-band, are subtracted in order to

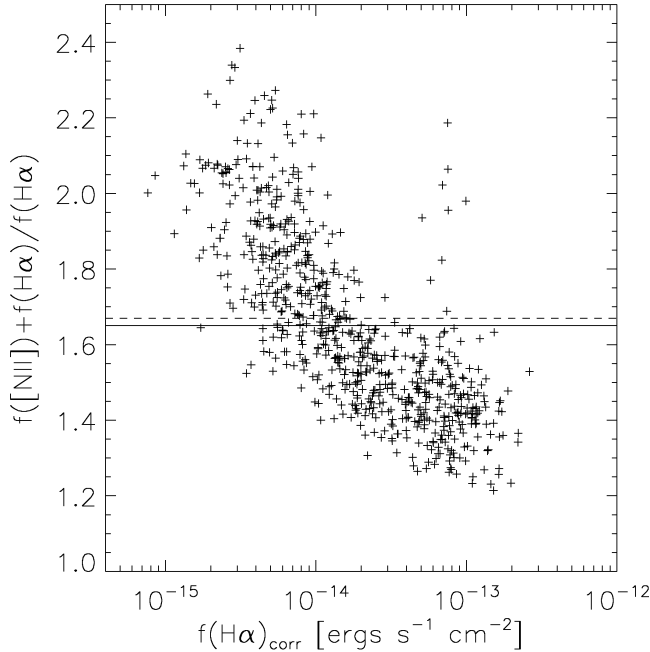


FIG. 15.— $([\text{NII}]\lambda 6548 + [\text{NII}]\lambda 6584 + \text{H}\alpha)/\text{H}\alpha$ ratio as a function of extinction corrected $\text{H}\alpha$ flux for the 718 regions under study. The solid line marks the observed mean value of 1.65. The dashed line marks the 1.67 value expected by assuming line ratio of $[\text{NII}]\lambda 6584/\text{H}\alpha = 0.5$ and $[\text{NII}]\lambda 6548/[\text{NII}]\lambda 6584 = 0.335$.

remove the continuum in the on-line bandpass. The excess flux in the on-line narrow-band is expected to map the nebular emission. Narrow-band filters have typical FWHMs of $\sim 70\text{\AA}$, and hence suffer from contamination from the $[\text{NII}]\lambda\lambda 6548, 6584$ doublet. Also, narrow-band techniques cannot directly separate the nebular emission from the underlying photospheric absorption $\text{H}\alpha$. Corrections to account for these two factors are usually applied.

In order to correct for the underlying absorption, the continuum image is usually scaled before subtraction so selected regions in the galaxy, which are a priori expected to be free of $\text{H}\alpha$ emission, show zero flux in the subtracted image. This is equivalent to correcting for a constant $\text{H}\alpha$ absorption EW across the galaxy (assuming that the continuum level was reliably estimated, which might not be the case when broad-bands are used instead of off-line narrow-bands, since the spectral slope of the stellar continuum can vary significantly across the galaxy). The $[\text{NII}]$ contamination is usually taken out by assuming a constant $[\text{NII}]/\text{H}\alpha$ ratio across the whole galaxy, which together with the relative filter transmission at the wavelengths of the three lines, is used to compute a correction factor which is used to scale down the observed continuum subtracted narrow-band fluxes in order to remove the $[\text{NII}]$ contribution. Integral-field spectroscopy is free of these two effects, since both the $[\text{NII}]$ lines and the photospheric $\text{H}\alpha$ absorption can be clearly separated from the $\text{H}\alpha$ emission (see Figure 3). Thus, our observations provide an important check on the validity of the corrections typically applied in narrow-band studies, and the biases introduced by them.

For the $[\text{NII}]$ correction, line ratios of $[\text{NII}]\lambda 6584/\text{H}\alpha = 0.5$ and $[\text{NII}]\lambda 6548/[\text{NII}]\lambda 6584 = 0.335$ are typically assumed (Calzetti et al. 2005). Based on these ratios, a perfect $\text{H}\alpha$ filter (i.e. one with a constant transmission across the three lines) would measure a flux that is a factor of 1.67 higher than the $\text{H}\alpha$ flux. Figure 15 shows the $([\text{NII}]\lambda 6548 + [\text{NII}]\lambda 6584 + \text{H}\alpha)/\text{H}\alpha$ ratio as a function of the extinction corrected $\text{H}\alpha$ flux, as measured in the VIRUS-P spectra of all 718 star-forming regions. Although we measure a mean value of 1.65 (solid line), in good agreement with the predictions from the above line ratios (dashed line), it can be seen that the correction factor is a strong function of $\text{H}\alpha$ flux. The fact that we observe an increasing $[\text{NII}]/\text{H}\alpha$ ratio as we go to fainter $\text{H}\alpha$ fluxes is consistent with the nebular emission in the faintest parts of the galaxy (mainly the inter-arm regions) being dominated by the DIG component of the ISM (see Figure 7 and §8).

The observed line ratios imply that assuming a constant $\text{NII}/\text{H}\alpha$ ratio throughout the galaxy would introduce systematic overestimations of the $\text{H}\alpha$ flux of up to 40% in the faintest regions, as well as systematic underestimations of up to 25% for the brightest regions. The effect is a strong function of $\text{H}\alpha$ flux, and its magnitude is of the order of the typical uncertainties quoted for narrow-band photometry of star-forming regions in nearby galaxies. While in theory these systematic miss-estimations should bias a measurement of the slope of the SFL towards shallower values, the magnitude of the effect is ten times smaller than the intrinsic scatter in the SFL and the introduced bias is negligible.

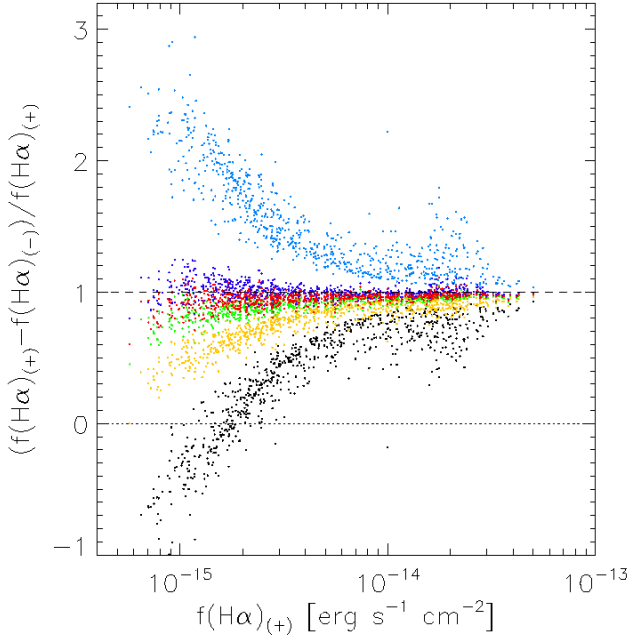


FIG. 16.— Bias introduced by the misestimation of the strength of the $H\alpha$ absorption feature or equivalently of the continuum level. Black dots show the fraction of the observed flux that we would observe if the stellar absorption was not considered at all. Red dots show the same fluxes corrected using a constant absorption $EW = -2.4\text{\AA}$. Dark blue and green dots correspond to underestimations and overestimations of the continuum by a 10%. Light blue and orange dots correspond to underestimations and overestimations of the continuum by a 50%.

Now let's look at the effects introduced by errors in the continuum subtraction and estimation of the underlying $H\alpha$ stellar absorption. When doing narrow-band imaging, the estimated value for the $H\alpha$ absorption EW is coupled, and impossible to separate from the estimated continuum level. So overestimations of the absorption EW can be thought as underestimations of the subtracted continuum and viceversa. Black crosses in Figure 16 show the observed $H\alpha$ emission flux (before dust extinction correction) versus the fractional difference between the $H\alpha$ emission and absorption fluxes for all the regions unaffected by AGN contamination. The magnitude of the $H\alpha$ absorption was measured in the best-fitted stellar continuum spectrum of each region, constructed as described in Section 5.1. The vertical axis in Figure 14 can be interpreted as the fraction of the true flux we would observe if the underlying absorption was not taken out from our measurement. Negative values correspond to regions in which the absorption EW is higher than the emission EW. We measure a fairly constant absorption EW, showing a median of -2.4\AA , and rms scatter of 0.2\AA between different regions. This supports the approximation of a constant $H\alpha$ absorption EW on which narrow-band corrections are based. Not taking into account the absorption feature can translate into gross underestimations of the emission line fluxes. For the brightest regions the underestimation can be up to $\sim 50\%$, and for the faintest regions we could completely miss the presence of nebular emission, and observe pure absorption.

The red crosses in Figure 16 show the emission minus

absorption fluxes corrected using a constant $H\alpha$ absorption EW of -2.4\AA . It can be seen that, under the assumption of a constant absorption EW, true fluxes can be recovered with typical uncertainties of less than 20% if the correct value of the median EW is used. Green and blue crosses in Figure 16 correspond to the values that would be obtained if the continuum had been overestimated and underestimated by 10% respectively, or equivalently if the $H\alpha$ absorption EW had been underestimated by -0.2\AA and overestimated by $+0.3\text{\AA}$. The orange and light blue crosses correspond to continuum misestimations of a 50% (-0.8\AA , $+2.4\text{\AA}$). These offsets are of the same order of magnitude as the typical uncertainties in the continuum subtraction of narrow-band images of nearby galaxies. It can be seen that a systematic misestimations can be introduced to the measured $H\alpha$ fluxes, especially in the fainter regions. Similarly to the [NII] correction discussed above, this effect is a strong function of $H\alpha$ flux and in this case can induce a significant change in the slope of the SFL if the estimated absorption (continuum level) is sufficiently off from the true value. A 10% error in the continuum level can introduce systematic misestimations of up to 30%, which is small compared to the intrinsic scatter in the SFL, but a 50% error in the estimation of the continuum can induce misestimations of the measured fluxes that are of the order of the SFL intrinsic scatter, and hence introduce a significant systematic bias to the SFL slope.

We perform a comparison of our spectroscopically measured $H\alpha$ emission line fluxes to fluxes measured by performing photometry in $4.3''$ diameter apertures at the positions of each of our fibers on the continuum-subtracted and absorption line corrected narrow-band image used by Calzetti et al. (2005) and Kennicutt et al. (2007). We correct the narrow-band fluxes for [NII] contamination using the correction factors shown in Figure 13, scaled by 0.97 to account for the lower filter transmission at the [NII] lines. Figure 17 shows the comparison. In order to account for differences in flux calibration and photometry aperture effects, we scale the narrow-band fluxes by a factor of 1.25, given by the mean ratio between the VIRUS-P and narrow-band fluxes for regions with $f(H\alpha) > 10^{-14}\text{erg s}^{-1}\text{cm}^{-2}$ (to the right of the dotted line in Figure 15). At high $H\alpha$ emission fluxes the effects of errors in the continuum subtraction are much smaller than for the fainter regions, so we consider safe to scale the fluxes in order to match the bright end of the distribution, also the magnitude of the scaling factor is of the order of the combined uncertainties in flux calibration.

Narrow-band fluxes presented in Figure 17 should not be affected by previously discussed systematics introduced by [NII] corrections, since we used the spectroscopically measured ratios to correct them. On the other hand, they clearly show a systematic deviation, with narrow-band fluxes being lower than spectroscopic fluxes as we go to fainter regions. This is consistent with an overestimation of the continuum level by $\sim 30\%$, or equivalently and underestimation of the $H\alpha$ absorption EW by -0.6\AA , which is well within the uncertainties involved in the continuum subtraction of the narrow-band image (Calzetti private communication). It is important to notice that in Kennicutt et al. (2007), the spatially resolved SFL was built by doing photometry on $H\alpha$ bright star-

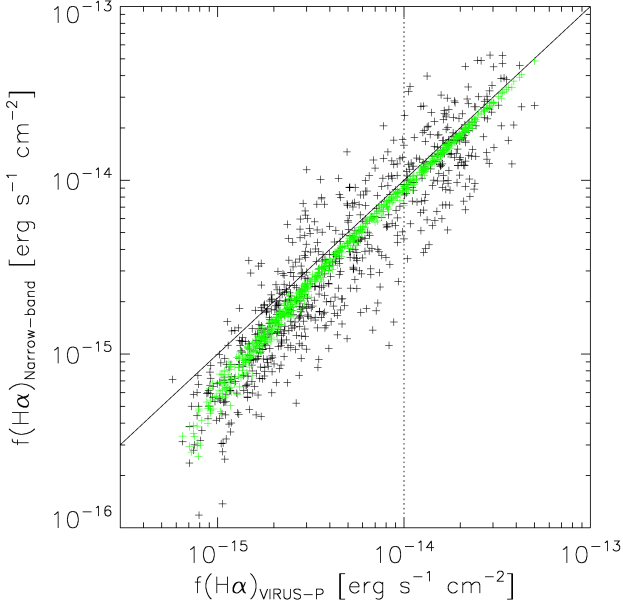


FIG. 17.— VIRUS-P observed $H\alpha$ fluxes (before dust extinction correction) versus $H\alpha$ fluxes measured in the continuum subtracted image from Calzetti et al. (2005) (black crosses). Data-points to the right of the vertical dotted line were used to scale the narrow-band fluxes in order to account for flux calibration and aperture discrepancies. The green crosses show the $H\alpha$ fluxes that would have been measured by VIRUS-P if the continuum would have been overestimated by a 30% (see Figure 16).

forming knots (brighter than $3 \times 10^{-15} \text{ erg s}^{-1} \text{ cm}^{-2}$), which are less affected by errors in the continuum subtraction than for example the inter-arm regions. Hence we do not expect this effect to significantly affect the slope of the SFL that they measure.

The above comparison stresses a very important point. Although very deep narrow-band imaging can be obtained using present day imagers, low surface-brightness photometry of nebular emission in these images is limited by uncertainties in the continuum subtraction and estimation of photospheric absorption. In this respect, integral field spectroscopy provides us with a less biased way of measuring faint nebular emission in nearby galaxies.

11. COMPARISON WITH PREVIOUS MEASUREMENTS AND THEORETICAL PREDICTIONS

In this section we compare our results to the recent measurements on the spatially resolved SFL in NGC5194 by Kennicutt et al. (2007) and Bigiel et al. (2008), and to the predictions of the theoretical model of the SFL proposed by Krumholz et al. (2009b).

We find an almost complete lack of correlation between the atomic gas surface density and the SFR surface density (Figure 10). This is in good agreement with the observation of both Kennicutt et al. (2007) and Bigiel et al. (2008), and confirms the fact that the SFR is correlated with the molecular gas density, and it is this correlation which drives the power-law part of the total gas SFL. At low gas surface densities ($< 20 M_{\odot} \text{ pc}^{-2}$) the ISM of spiral galaxies stops being mostly molecular, and hence the shape of the total gas SFL is driven by a combination of the molecular gas SFL and the ratio of molecular to

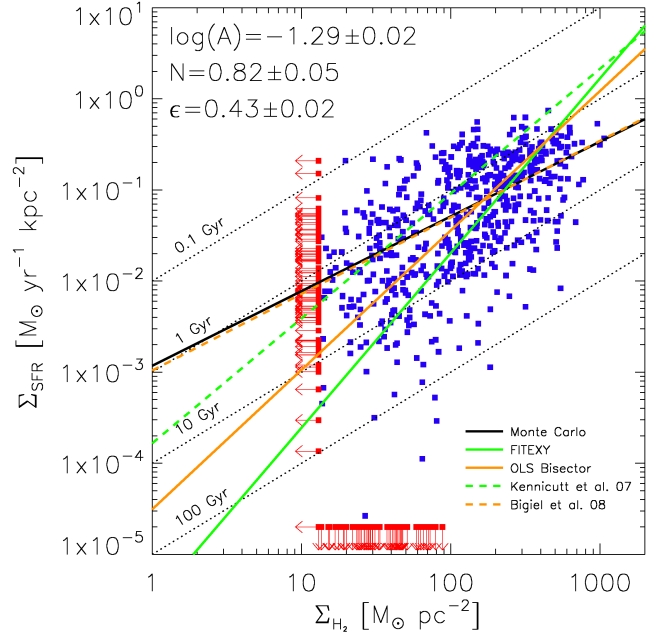


FIG. 18.— Molecular gas SFL as measured by VIRUS-P. Symbols are the same as in Figure 12. The black solid line shows our best fitted power-law obtained using the Monte Carlo method described in §9.1. Previous measurements by Kennicutt et al. (2007) and Bigiel et al. (2008) are shown as the green and orange dashed lines respectively. Also shown are fits to our data (rejecting upper limits) using the FITEXY (solid green line) and OLS bisector (solid orange line) methods.

atomic hydrogen.

As discussed in §1, Kennicutt et al. (2007) finds a super-linear slope of 1.37 for the molecular SFL in NGC5194, while Bigiel et al. (2008) measures a slightly sub-linear slope of 0.84. The first of these measurements is consistent with models in which the SFR is inversely proportional to the gas free-fall time in GMCs and the molecular gas surface density is proportional to the total gas density ($N = 1.5$, Kennicutt (1998b)), while the second is more consistent with models in which the SFR shows a linear correlation with the molecular gas density, product of star-formation taking place at a constant efficiency in GMCs. Hence, establishing the slope of the SFL is important in order to distinguish between different physical phenomena that give rise to it.

Figure 18 shows the molecular SFL measured as described in §9, together with the best-fitted SFL as measured by Kennicutt et al. (2007) and Bigiel et al. (2008). The results from the latter are adjusted to account for differences in the IMF assumed for calculating Σ_{SFR} , and the different CO- H_2 conversion factor used in the calculation of Σ_{H_2} .

Our best-fitted molecular SFL shows a considerably shallower slope than the one measured by Kennicutt et al. (2007). We consider the source of the disagreement to be a combination of two factors. First, as shown in §10, the narrow-band $H\alpha$ fluxes used by Calzetti et al. (2005) and Kennicutt et al. (2007) might be underestimated at the faint end of the flux distribution due to small systematic errors in continuum subtraction, although the effect is small (of the order of the

intrinsic scatter in the SFL), and cannot account for the bulk of the difference observed in the SFL slope. The second factor, which we consider to be the main cause behind the disagreement, is the difference in the fitting methods used to adjust a power-law to the data. As mentioned in §9, Kennicutt et al. (2007) used a FITEXY algorithm to perform a linear regression to the data in logarithmic space, rejecting upper limits in Σ_{H_2} from the fit, and not fitting for the intrinsic scatter in the SFL. The solid green line in Figure 17 shows the result of applying the same procedure to our data. The FITEXY method significantly overpredicts the slope of the SFL ($N = 1.9$), in large part due to the exclusion of the Σ_{H_2} upper limits. These data-points, having large error bars in Σ_{gas} and clear detections in Σ_{SFR} , have a significant statistical weight in the Monte Carlo fit because of their large number. Another factor promoting the fitting of shallower slopes by our Monte Carlo method, is the fact that we included the intrinsic dispersion in the SFL as a scatter in Σ_{SFR} , hence the fit will tend to equalize the number of data-points above and below the power-law at any given Σ_{gas} . This is a consequence of the expectation for a causal relation between Σ_{gas} and Σ_{SFR} , with the SFR being a function of the gas density, and not viceversa.

Kennicutt et al. (2007) provide a table of their measured values for Σ_{SFR} and Σ_{HI+H_2} and their uncertainties, from which they recover a slope of $N = 1.56$ for the total gas SFL. We apply our Monte Carlo fitting method to their data, and find best-fitted values of $A = 10^{-1.23 \pm 0.03}$ for the amplitude, $\epsilon = 0.40 \pm 0.03$ for the intrinsic scatter, and a slope $N = 1.03 \pm 0.08$. This shallower slope is a lot closer to our measured value of $N = 0.85$, and the rest of the difference can be easily explained by the underestimation of the narrow-band $H\alpha$ fluxes presented in Figure 17 and differences in the DIG correction. The two independent datasets show excellent agreement in the value of intrinsic scatter. The small difference of 0.08 dex in the amplitude can be attributed to the fact that Kennicutt et al. (2007) targeted active star-forming regions in their study, and hence their measurement of the SFL is most likely biased towards higher star-formation efficiencies than the one presented here.

On the other hand, we measure a molecular SFL which shows an excellent agreement with Bigiel et al. (2008) both in slope and normalization. The agreement is better than expected, given the differences in the methods used to measure Σ_{SFR} and fitting the SFL. Their SFR measurements are not based on extinction corrected hydrogen recombination lines as in Kennicutt et al. and this work, but rather on a linear combination of space-based GALEX far-UV and *Spitzer* MIPS 24 μ m fluxes. Also, they do not correct their data in order to account for any contribution from the DIG. The fitting method used by Bigiel et al. (2008) is an OLS Bisector, and they also reject non detections in CO from the fit. The orange solid line shows the result of applying this fitting method to our data. Just as in the case of the FITEXY algorithm, the OLS Bisector yields a significantly higher slope ($N = 1.5$) than the Monte Carlo fit. The reasons for this are the same as for the FITEXY algorithm, that is, the inclusion of the upper limits in Σ_{H_2} , and the introduction of the intrinsic scatter in Σ_{SFR} in our method. One possible explanation for the agreement could be the

interplay between the lack of DIG correction and the difference in fitting methods. The first will tend to drive the slope to shallower values, while the second will steepen it. The combination of these two effects working in opposite directions might be behind the agreement between Bigiel et al. (2008) and this work.

Although the comparison is hard due to the systematics involved in the different methods, the bottom line is that we measure a slope that is consistent with the scenario proposed by Bigiel et al. (2008) and Leroy et al. (2008), in which star-formation takes place at a nearly constant efficiency in GMCs over a large range of environments present in galaxies. This is also in agreement with recent findings of (Bolatto et al. 2008), who find that extragalactic GMCs in the Local Group, detected on the basis of their CO emission, exhibit remarkably uniform properties, with a typical mass surface density of roughly $85 \text{ M}_\odot \text{pc}^{-2}$.

Based on these concepts of uniformity of GMC properties, and good correlation between the SFR and the molecular gas density, Krumholz et al. (2009b) proposed a simple theoretical model to explain the observed total gas SFL. In their model, star formation takes place only in molecular gas, and the total gas SFL is determined by three factors. First, the fraction of the gas in molecular form is set by the balance between the formation of H_2 in the surface of dust grains, and the dissociation of molecules by the far-UV continuum in the Lyman-Werner bands (Krumholz et al. 2008, 2009a). This drives the shape of the total gas SFL in the low density regime where the ISM is not fully molecular. Second, the star-formation efficiency inside GMCs is low, and it is set by turbulence driven feedback processes (Krumholz & McKee 2005). These are responsible for the power-law behavior of the molecular SFL. Third, GMCs are decoupled from the surrounding ISM when their internal pressure is higher than external pressure. In this regime their structure is determined by internal feedback processes, and they show very uniform properties including an almost constant surface density of $85 \text{ M}_\odot \text{pc}^{-2}$ (Bolatto et al. 2008). When the galactic ISM pressure becomes higher than this value, the GMC surface density must increase accordingly in order to maintain pressure balance with the external ISM. This gives rise to a steepening of the slope of the molecular SFL at $\Sigma_{H_2} \geq 85 \text{ M}_\odot \text{pc}^{-2}$. In summary, the total gas SFL in the model shows a different behavior in the low, intermediate, and high density regimes. At low densities its behavior is driven by the transition from an atomic to a molecular ISM. Beyond the point at which the ISM becomes almost fully molecular the total gas SFL follows closely the molecular SFL, which shows a steeper slope in the high density regime driven by the pressure balance between the galactic ISM and GMCs.

Figure 18 shows a comparison of our data and the Krumholz et al. (2009b) model. We have assumed $Z' = Z/Z_{MW} = 1.0/1.5$, consistently with the DIG correction applied in §8, and a clumpiness factor $c = 4$ to account for the effect that the averaging of Σ_{gas} introduces in the molecular fraction in the model. We observe an excellent agreement for both the atomic and molecular gas, as well as for the total gas SFL. The gas density range sampled by our observations, and the scatter in SFL does not allow us to discern between the model and the simple

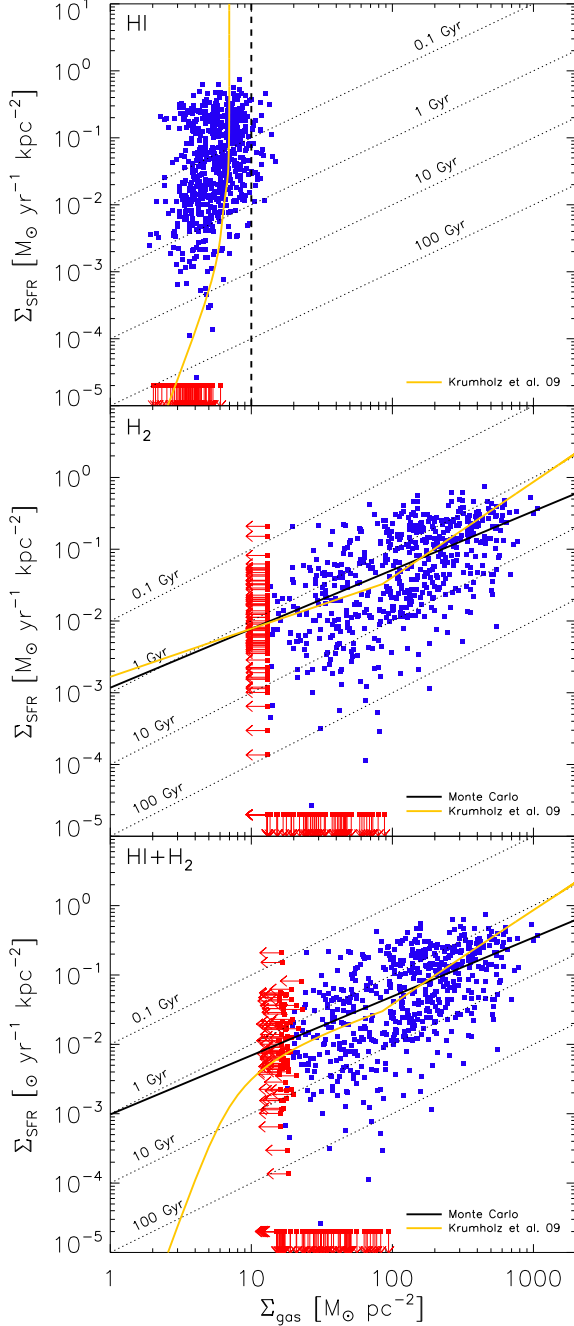


FIG. 19.— Comparison of the observed SFL for atomic gas (top), molecular gas (center), and total gas (bottom) and the theoretical model proposed by Krumholz et al. (2009b). Symbols are the same as in Figures 11, 12, and 12. The solid orange line show the Krumholz et al model for $Z' = 1.0/1.5$ and $c = 4$.

power law fitted using the Monte Carlo method, stressing the need to extend our observations towards more extreme density environments.

12. SUMMARY AND CONCLUSIONS

We have performed the first measurement of the spatially resolved SFL in nearby galaxies using integral field

spectroscopy. The wide field VIRUS-P spectroscopic map of the central 4.1×4.1 kpc² of NGC 5194, together with the HI 21cm map from THINGS, and the CO J=1-0 from BIMA SONG were used to measure Σ_{SFR} , Σ_{HI} , and Σ_{H_2} for 718 regions ~ 170 pc in diameter throughout the disk of the galaxy.

In this paper we have presented our method for calculating Σ_{SFR} from the spectroscopically measured H α emission line fluxes. We have shown that the observed H α /H β ratio is a good estimator of the nebular dust extinction, at least at the levels of obscuration present in face-on normal spiral galaxies like NGC 5194.

We have also presented a new method for estimating the contribution of the DIG to the H α emission line flux, which is based on the observed low-ionization line ratio [SII]/H α , and the large differences seen in this line ratio between H II regions and pointings towards the DIG in the Milky Way. The use of line ratios to correct both for dust extinction and the DIG contribution is possible only because of the use of integral field spectroscopy spanning a large wavelength range, which includes all these important emission lines.

One of the main goals of this work is to make use of these clean spectroscopic emission line measurements to study the systematics involved in narrow-band estimations of the H α emission line flux of nearby galaxies. We showed that proper estimation of the continuum and of the underlying stellar absorption features is crucial in order to get an unbiased estimate of the H α flux. Errors of the order of 30% in the estimation of these quantities can introduce systematic misestimations of the H α emission line flux by up to a factor of 3 in the low surface brightness regime.

We also tested the assumption of a constant [NII]/H α ratio throughout the galaxy, usually used to remove the [NII] doublet contamination from the narrow-band measured fluxes. We found that the [NII]/H α ratio varies significantly throughout the galaxy, and shows a clear correlation with the H α flux. The sense of the correlation implies a higher [NII]/H α ratio in regions that are fainter in H α (typically the inter-arm regions of the galaxy), and is consistent with the DIG dominating the nebular spectrum in these zones. Assuming a constant [NII]/H α would introduce overestimations of the H α flux of $\sim 40\%$ in the inter-arm regions, and underestimations of $\sim 25\%$ for the brightest star-forming regions in the spiral arms.

Integral field spectroscopy proves to be an extremely powerful tool for mapping the SFR throughout the disks of nearby galaxies, especially with the advent of large field of view IFUs like VIRUS-P. Spatially resolved spectral maps, besides allowing us to measure emission line fluxes in a much more unbiased way than narrow-band imaging, also provides extensive information about the physical conditions throughout the disks of nearby spiral galaxies. The spectra allows the measurement of metallicities, stellar and gas kinematics, stellar populations, and star formation histories across galaxies. In a future study we will investigate the role that all these other quantities that can be extracted from our data play at setting the SFR.

We found that the SFR surface density shows a lack of correlation with the atomic gas surface density, and a clear correlation with the molecular gas surface density. Hence, the total gas SFL is fully driven by the molecular

gas SFL in the density regimes sampled by our observations. The atomic gas surface density is observed to saturate at a value of $\sim 10 \text{ M}_\odot \text{pc}^{-2}$, at which a phase transition between atomic and molecular gas is thought to occur in the ISM.

A Monte Carlo method for fitting the SFL which is not affected by the systematics involved in performing linear correlations of incomplete data in logarithmic space was presented. Our method fits the intrinsic scatter in the SFL as a free parameter. Applying this method to our data yields slightly sub-linear slopes N of 0.82 and 0.85 for the molecular and total gas SFLs respectively.

Comparison with previous measurements of the spatially resolved SFL are somewhat challenging because of the different recipes used to estimate Σ_{SFR} , and the different fitting procedures used to derive the SFL parameters. The slopes we measured are in disagreement with the results of Kennicutt et al. (2007), who measured a strongly super-linear slope for both the molecular component and the total gas. On the other hand, our results are in very good agreement with the slope measured for the molecular gas SFL in NGC 5194 by Bigiel et al. (2008). Our results are consistent with the scenario recently proposed by Bigiel et al. (2008) and Leroy et al. (2008) of a nearly constant SFE in GMCs, which is almost independent of the molecular gas surface density. The main argument to support this scenario is the observation of a close to linear correlation between the Σ_{SFR} and Σ_{gas} in the density ranges present in the ISM of nearby normal spiral galaxies.

On the other hand our results also show a very good agreement with the more complex scenario recently proposed by Krumholz et al. (2009b), in which the surface density of molecular gas grows with the molecular to atomic fraction at low densities ($\Sigma_{\text{HI}+\text{H}_2} \lesssim 10 \text{ M}_\odot \text{pc}^{-2}$), becomes constant at intermediate densities ($10 \text{ M}_\odot \text{pc}^{-2} \lesssim \Sigma_{\text{HI}+\text{H}_2} \lesssim 100 \text{ M}_\odot \text{pc}^{-2}$), and increases linearly with the total gas density in the high density regime ($\Sigma_{\text{HI}+\text{H}_2} \gtrsim 100 \text{ M}_\odot \text{pc}^{-2}$). This, combined with an slightly sub-linear efficiency as a function of molecular gas surface density given by the balance between gravitational potential energy and turbulent kinetic energy originated by internal feedback, gives rise to the observed SFL. In their model, the total gas SFL has a super-linear slope $N = 1.33$ in the high density regime, gets shallower at intermediate densities showing a slope of $N = 0.67$, and steepens again at lower densities as the molecular to atomic gas fraction rapidly decreases. Our observations sample the transition between the intermediate and high density regimes in the model. The intrinsic scatter in the SFL, together with our limited density dynamic range does not allow us to observe the predicted kink in the SFL directly, but our measured slope of 0.85 is very close to what we expect to measure in a region where we sample both the sub-linear and super-linear parts of the SFL predicted by Krumholz et al. model. A proper detection of the kink in the SFL predicted by Krumholz et al. (2009b) will require extending the dynamic range to higher gas surface densities.

A major success of the Krumholz et al. (2009b) model is the excellent agreement it shows with the observation with respect to the SFE, or equivalently to the gas depletion timescales. We observe very long depletion

timescales of $\tau \approx 2 \text{ Gyr}$, in good agreement with previous observations. This time is ~ 100 longer than the typical GMC free-fall time. The good agreement between our observations and the Krumholz et al. model implies that this very low efficiency can be easily explained by models in which star-formation is self regulated through turbulence induced by internal mechanical feedback in GMCs.

An important result of this study is the large intrinsic scatter of 0.43 dex observed in both the molecular and total gas SFLs. This translates into a factor of ~ 3 scatter in the SFR for regions having the same molecular gas availability, and it may indicate the existence of further parameters that are important in setting the SFR. It is worth mentioning that part of the intrinsic scatter in the SFL must come from the scatter in the SFR-L($\text{H}\alpha$) calibration. Charlot & Longhetti (2001) show that SFRs derived from $\text{H}\alpha$ alone present a large scatter when compared to SFRs derived from full spectral fitting of the stellar populations and nebular emission of a sample of 92 nearby star-forming galaxies. Recently, the detection of widespread UV emission beyond the $\text{H}\alpha$ brightness profile cutoff in the outer disks of many nearby galaxies (Gil de Paz et al. 2005; Thilker et al. 2005; Boissier et al. 2007), has raised questions about the proportionality between the $\text{H}\alpha$ emission and the SFR in the low star-formation regime. Incomplete sampling of the IMF in low-mass embedded clusters has been proposed to explain the discrepancy between $\text{H}\alpha$ and UV surface brightness profiles (e.g. Pflamm-Altenburg & Kroupa 2009). Under this scenario the $\text{H}\alpha$ emission fails to tracing star-formation in low mass clusters where statistical fluctuations can translate into a lack of massive ionizing stars, and the SFR-L($\text{H}\alpha$) becomes non-linear in the low star-formation regime (Pflamm-Altenburg et al. 2007), which might enhance the downward scatter in our SFL measurements. This issue is beyond the scope of the current paper, but we intend to investigate the implications of applying non-linear SFR-L($\text{H}\alpha$) to our data in future works.

In this paper we have established the method for studying the spatially resolved SFL using wide integral field spectroscopy, and have set new constraints on important quantities like the slope, normalization, and intrinsic scatter of the SFL. As mentioned in §1, this data forms part of an undergoing large scale IFU survey of nearby galaxies. VENGA will map the disks of ~ 20 nearby spiral galaxies to radius much larger than those sampled by the data presented here. In the future, we will extend this type of study to a larger set of galaxies spanning a range in Hubble types, metallicities, and star-formation activities. This will help us to sample a larger dynamical range in gas surface densities. The later requires the observation of much denser environments, like the ones present in starburst galaxies, to extend the observed SFL to higher densities. Deeper CO observations that map the molecular gas out to large radii will be necessary to extend the sampled range to lower densities. This is of great importance, since a proper characterization of the shape of the total gas SFL is necessary in order to distinguish between different star-formation models.

We thank Phillip McQueen and Gary Hill for designing and constructing VIRUS-P, and for their advice on the

use of the instrument. We also acknowledge David Doss and the staff at McDonald Observatory for their invaluable help during the observations. Tables of the WHAM DIG line ratios were kindly provided by George J. Madsen. We thank Daniela Calzetti for some very useful discussions, and for providing the narrow-band Pa α and H α images used in her work. This study has been possi-

ble thanks to the financial support of the Sigma Xi, The Scientific Research Society. The construction of VIRUS-P was possible thanks to the generous support of the Cynthia & George Mitchell Foundation. NJE and AH were supported in part by NSF Grant AST-0607193. Finally we thank the referee for the helpful comments which helped to improve the quality of this work.

REFERENCES

- Allende Prieto, C., Lambert, D. L., & Asplund, M. 2001, *ApJ*, 556, L63
- Beers, T. C., Flynn, K., & Gebhardt, K. 1990, *AJ*, 100, 32
- Bigiel, F., Leroy, A., Walter, F., Brinks, E., de Blok, W. J. G., Madore, B., & Thornley, M. D. 2008, *AJ*, 136, 2846
- Blitz, L., Fukui, Y., Kawamura, A., Leroy, A., Mizuno, N., & Rosolowsky, E. 2007, *Protostars and Planets V*, 81
- Bloemen, J. B. G. M., et al. 1986, *A&A*, 154, 25
- Boissier, S., et al. 2007, *ApJS*, 173, 524
- Bolatto, A. D., Leroy, A. K., Rosolowsky, E., Walter, F., & Blitz, L. 2008, *ApJ*, 686, 948
- Bradley, L. D., Kaiser, M. E., & Baan, W. A. 2004, *ApJ*, 603, 463
- Bresolin, F., Garnett, D. R., & Kennicutt, R. C., Jr. 2004, *ApJ*, 615, 228
- Calzetti, D., et al. 2005, *ApJ*, 633, 871
- Charlot, S., & Longhetti, M. 2001, *MNRAS*, 323, 887
- Crane, P. C., & van der Hulst, J. M. 1992, *AJ*, 103, 1146
- Deharveng, L., Peña, M., Caplan, J., & Costero, R. 2000, *MNRAS*, 311, 329
- Dolphin, A. E., et al. 2001, *MNRAS*, 324, 249
- Dove, J. B., Shull, J. M., & Ferrara, A. 2000, *ApJ*, 531, 846
- Evans, N. J., et al. 2009, *ApJS*, 181, 321
- Ferguson, A. M. N., Wyse, R. F. G., Gallagher, J. S., III, & Hunter, D. A. 1996, *AJ*, 111, 2265
- Gil de Paz, A., et al. 2005, *ApJ*, 627, L29
- Greenawalt, B., Walterbos, R. A. M., Thilker, D., & Hoopes, C. G. 1998, *ApJ*, 506, 135
- Grevesse, N., Noels, A., & Sauval, A. J. 1996, *Cosmic Abundances*, 99, 117
- Haffner, L. M., et al. 2009, *arXiv:0901.0941*
- Helfer, T. T., Thornley, M. D., Regan, M. W., Wong, T., Sheth, K., Vogel, S. N., Blitz, L., & Bock, D. C.-J. 2003, *ApJS*, 145, 259
- Hill G. J., et al. 2008, *Proc. SPIE*, Vol. 7014, 701470 (2008); DOI:10.1117/12.790235
- Hoopes, C. G., Walterbos, R. A. M., & Greenawalt, B. E. 1996, *AJ*, 112, 1429
- Hoopes, C. G., & Walterbos, R. A. M. 2003, *ApJ*, 586, 902
- Isobe, T., Feigelson, E. D., Akritas, M. G., & Babu, G. J. 1990, *ApJ*, 364, 104
- Kennicutt, R. C., Jr. 1998, *ARA&A*, 36, 189
- Kennicutt, R. C., Jr. 1998, *ApJ*, 498, 541
- Kennicutt, R. C., Jr., et al. 2007, *ApJ*, 671, 333
- Kewley, L. J., Dopita, M. A., Sutherland, R. S., Heisler, C. A., & Trevena, J. 2001, *ApJ*, 556, 121
- Krumholz, M. R., & McKee, C. F. 2005, *ApJ*, 630, 250
- Krumholz, M. R., & Tan, J. C. 2007, *ApJ*, 654, 304
- Krumholz, M. R., McKee, C. F., & Tumlinson, J. 2008, *ApJ*, 689, 865
- Krumholz, M. R., McKee, C. F., & Tumlinson, J. 2009, *ApJ*, 693, 216
- Krumholz, M. R., McKee, C. F., & Tumlinson, J. 2009, *arXiv:0904.0009*
- Leroy, A. K., Walter, F., Brinks, E., Bigiel, F., de Blok, W. J. G., Madore, B., & Thornley, M. D. 2008, *AJ*, 136, 2782
- Madsen, G. J., Reynolds, R. J., & Haffner, L. M. 2006, *ApJ*, 652, 401
- Mathis, J. S. 2000, *ApJ*, 544, 347
- McKee, C. F. 1999, *NATO ASIC Proc. 540: The Origin of Stars and Planetary Systems*, 29
- Mutchler, M., et al. 2005, *Bulletin of the American Astronomical Society*, 37, 452
- Oey, M. S., et al. 2007, *ApJ*, 661, 801
- Oke, J. B. 1990, *AJ*, 99, 1621
- Osterbrock, D. E., & Ferland, G. J. 2006, *Astrophysics of gaseous nebulae and active galactic nuclei*, 2nd. ed. by D.E. Osterbrock and G.J. Ferland. Sausalito, CA: University Science Books, 2006,
- Pei, Y. C. 1992, *ApJ*, 395, 130
- Pflamm-Altenburg, J., Weidner, C., & Kroupa, P. 2007, *ApJ*, 671, 1550
- Pflamm-Altenburg, J. & Kroupa, P. 2009, *arXiv:0905.0898*
- Press, W. H., Flannery, B. P., Teukolsky, S. A., & Vetterling, W. T. 1989, *Cambridge: University Press*, 1989,
- Reynolds, R. J. 1985, *ApJ*, 294, 256
- Schlegel, D. J., Finkbeiner, D. P., & Davis, M. 1998, *ApJ*, 500, 525
- Schmidt, M. 1959, *ApJ*, 129, 243
- Schuster, K. F., Kramer, C., Hitschfeld, M., Garcia-Burillo, S., & Mookerjee, B. 2007, *A&A*, 461, 143
- Scoville, N. Z., Polletta, M., Ewald, S., Stolovy, S. R., Thompson, R., & Rieke, M. 2001, *AJ*, 122, 3017
- Shaver, P. A., McGee, R. X., Newton, L. M., Danks, A. C., & Pottasch, S. R. 1983, *MNRAS*, 204, 53
- Terashima, Y., & Wilson, A. S. 2001, *ApJ*, 560, 139
- Thilker, D. A., Walterbos, R. A. M., Braun, R., & Hoopes, C. G. 2002, *AJ*, 124, 3118
- Thilker, D. A., et al. 2005, *ApJ*, 619, L79
- Tully, R. B. 1974, *ApJS*, 27, 437
- Valdes, F., Gupta, R., Rose, J. A., Singh, H. P., & Bell, D. J. 2004, *ApJS*, 152, 251
- Veilleux, S., & Osterbrock, D. E. 1987, *ApJS*, 63, 295
- Walter, F., Brinks, E., de Blok, W. J. G., Bigiel, F., Kennicutt, R. C., Thornley, M. D., & Leroy, A. 2008, *AJ*, 136, 2563
- Wong, T., & Blitz, L. 2002, *ApJ*, 569, 157

TABLE 1
NEBULAR EMISSION LINE FLUXES, GAS SURFACE DENSITIES, AND SFR
SURFACE DENSITIES

ID	Equatorial Coordinates		H β	[NII] λ 6548	H α	[NII] λ 6584	[SII] λ 6717	[SII] λ 6731	Σ_{H_2}	Σ_{HI}	Σ_{SFR}
	α	δ	$10^{-16} \text{ erg s}^{-1} \text{ cm}^{-2}$			$M_{\odot} \text{ pc}^{-2}$			$M_{\odot} \text{ pc}^{-2}$	$M_{\odot} \text{ yr}^{-1} \text{ kpc}^{-2}$	
1	13:29:48.11	+47:12:35.6	12.57 \pm 0.11	6.45 \pm 0.42	69.73 \pm 0.59	17.63 \pm 0.43	6.89 \pm 0.23	4.95 \pm 0.23	10.71 \pm 13.00	9.75 \pm 0.59	0.08181 \pm 0.01652
2	13:29:48.83	+47:12:35.5	4.22 \pm 0.41	4.94 \pm 0.46	29.44 \pm 0.54	13.90 \pm 0.48	4.77 \pm 0.43	3.12 \pm 0.43	127.44 \pm 13.00	12.25 \pm 0.59	0.05385 \pm 0.01664
3	13:29:49.55	+47:12:35.3	6.05 \pm 0.25	5.89 \pm 0.43	36.35 \pm 0.52	17.82 \pm 0.47	6.02 \pm 0.10	4.63 \pm 0.10	399.25 \pm 13.00	8.73 \pm 0.59	0.04681 \pm 0.01063
4	13:29:50.28	+47:12:35.2	4.78 \pm 0.25	4.42 \pm 0.53	27.71 \pm 0.59	13.85 \pm 0.55	4.11 \pm 0.10	3.02 \pm 0.10	174.20 \pm 13.00	10.05 \pm 0.59	0.02975 \pm 0.00752
5	13:29:51.00	+47:12:35.0	2.94 \pm 0.01	4.88 \pm 0.55	16.37 \pm 0.54	11.66 \pm 0.54	3.19 \pm 0.03	2.44 \pm 0.03	127.30 \pm 13.00	10.53 \pm 0.59	0.01123 \pm 0.00274
6	13:29:51.72	+47:12:34.8	4.75 \pm 0.04	5.77 \pm 0.29	24.74 \pm 0.31	16.43 \pm 0.30	4.64 \pm 0.10	2.99 \pm 0.10	131.55 \pm 13.00	7.08 \pm 0.59	0.01791 \pm 0.00369
7	13:29:52.44	+47:12:34.7	10.97 \pm 0.54	7.33 \pm 0.27	54.63 \pm 0.36	21.14 \pm 0.30	6.39 \pm 0.26	4.75 \pm 0.25	177.73 \pm 13.00	8.80 \pm 0.59	0.04645 \pm 0.01083
8	13:29:53.16	+47:12:34.5	4.62 \pm 0.48	4.20 \pm 0.44	27.62 \pm 0.50	13.26 \pm 0.47	4.30 \pm 0.48	2.47 \pm 0.45	168.82 \pm 13.00	8.98 \pm 0.59	0.03255 \pm 0.01115
9	13:29:53.89	+47:12:34.3	4.99 \pm 0.44	4.08 \pm 0.25	23.63 \pm 0.28	11.96 \pm 0.27	4.13 \pm 0.47	2.97 \pm 0.48	234.42 \pm 13.00	7.61 \pm 0.59	0.01148 \pm 0.00453
10	13:29:54.61	+47:12:34.2	14.64 \pm 0.58	7.49 \pm 0.53	77.49 \pm 0.77	23.63 \pm 0.59	8.51 \pm 0.27	6.00 \pm 0.27	156.60 \pm 13.00	10.39 \pm 0.59	0.08200 \pm 0.01802
11	13:29:55.33	+47:12:34.0	17.90 \pm 0.57	8.67 \pm 0.43	110.78 \pm 0.74	25.85 \pm 0.49	9.25 \pm 0.25	6.34 \pm 0.24	60.35 \pm 13.00	7.20 \pm 0.59	0.17611 \pm 0.03717
12	13:29:56.05	+47:12:33.9	26.21 \pm 0.65	9.79 \pm 0.27	151.56 \pm 0.50	29.99 \pm 0.32	9.70 \pm 0.11	6.57 \pm 0.10	19.73 \pm 13.00	4.79 \pm 0.59	0.20946 \pm 0.04325
13	13:29:56.78	+47:12:33.7	5.97 \pm 0.43	3.54 \pm 0.43	35.11 \pm 0.55	11.43 \pm 0.46	3.37 \pm 0.41	2.36 \pm 0.41	6.45 \pm 13.00	2.77 \pm 0.59	0.04218 \pm 0.01144
14	13:29:57.50	+47:12:33.5	1.65 \pm 0.35	3.13 \pm 0.11	9.08 \pm 0.08	6.03 \pm 0.08	2.10 \pm 0.08	1.49 \pm 0.08	65.49 \pm 13.00	3.78 \pm 0.59	0.00121 \pm 0.00489
15	13:29:47.74	+47:12:29.4	4.11 \pm 0.41	3.99 \pm 0.44	29.62 \pm 0.54	11.94 \pm 0.47	4.03 \pm 0.22	2.56 \pm 0.22	102.00 \pm 13.00	11.76 \pm 0.59	0.05899 \pm 0.01827
16	13:29:48.46	+47:12:29.2	5.33 \pm 0.48	4.19 \pm 0.26	30.08 \pm 0.31	11.94 \pm 0.27	3.97 \pm 0.46	2.94 \pm 0.49	116.73 \pm 13.00	10.70 \pm 0.59	0.03078 \pm 0.00962
17	13:29:49.18	+47:12:29.0	4.16 \pm 0.48	4.29 \pm 0.49	23.25 \pm 0.50	12.24 \pm 0.48	3.53 \pm 0.49	2.52 \pm 0.49	191.33 \pm 13.00	7.41 \pm 0.59	0.02067 \pm 0.00838
18	13:29:49.90	+47:12:28.9	4.46 \pm 0.54	4.26 \pm 0.55	24.35 \pm 0.58	12.58 \pm 0.57	4.03 \pm 0.04	2.92 \pm 0.04	107.58 \pm 13.00	5.40 \pm 0.59	0.02056 \pm 0.00859
19	13:29:50.62	+47:12:28.7	2.90 \pm 0.26	5.82 \pm 0.49	17.49 \pm 0.49	15.35 \pm 0.50	4.41 \pm 0.11	3.36 \pm 0.11	58.22 \pm 13.00	6.21 \pm 0.59	0.01711 \pm 0.00618
20	13:29:51.35	+47:12:28.6	2.66 \pm 0.49	4.35 \pm 0.29	13.53 \pm 0.29	12.24 \pm 0.30	4.35 \pm 0.30	2.49 \pm 0.27	127.99 \pm 13.00	5.12 \pm 0.59	0.00415 \pm 0.00540
21	13:29:52.07	+47:12:28.4	4.22 \pm 0.46	5.92 \pm 0.29	25.72 \pm 0.31	17.14 \pm 0.30	4.28 \pm 0.51	3.49 \pm 0.53	170.03 \pm 13.00	5.87 \pm 0.59	0.03125 \pm 0.01090
22	13:29:52.79	+47:12:28.2	8.83 \pm 0.52	5.32 \pm 0.52	45.38 \pm 0.66	16.26 \pm 0.56	5.23 \pm 0.26	3.87 \pm 0.28	207.98 \pm 13.00	6.75 \pm 0.59	0.04023 \pm 0.01007
23	13:29:53.51	+47:12:28.1	7.02 \pm 0.56	4.31 \pm 0.50	34.93 \pm 0.56	12.86 \pm 0.51	4.50 \pm 0.01	2.90 \pm 0.01	68.23 \pm 13.00	4.17 \pm 0.59	0.02578 \pm 0.00782
24	13:29:54.23	+47:12:27.9	6.14 \pm 0.29	5.20 \pm 0.13	36.11 \pm 0.14	12.94 \pm 0.12	4.55 \pm 0.54	3.15 \pm 0.55	207.04 \pm 13.00	6.91 \pm 0.59	0.04371 \pm 0.01007
25	13:29:54.96	+47:12:27.7	13.46 \pm 0.55	8.57 \pm 0.27	86.25 \pm 0.41	26.44 \pm 0.30	8.65 \pm 0.11	6.15 \pm 0.10	184.39 \pm 13.00	9.14 \pm 0.59	0.14613 \pm 0.03182
26	13:29:55.68	+47:12:27.6	24.96 \pm 0.64	9.80 \pm 0.52	123.07 \pm 0.88	27.29 \pm 0.59	9.88 \pm 0.51	7.15 \pm 0.50	96.32 \pm 13.00	7.04 \pm 0.59	0.11532 \pm 0.02399
27	13:29:56.40	+47:12:27.4	21.15 \pm 0.62	7.97 \pm 0.29	112.54 \pm 0.46	21.82 \pm 0.30	7.24 \pm 0.27	5.27 \pm 0.27	49.28 \pm 13.00	5.51 \pm 0.59	0.12542 \pm 0.02629
28	13:29:57.12	+47:12:27.2	2.91 \pm 0.36	3.66 \pm 0.38	22.94 \pm 0.43	10.45 \pm 0.39	3.18 \pm 0.42	2.06 \pm 0.38	72.04 \pm 13.00	4.81 \pm 0.59	0.05493 \pm 0.01943
29	13:29:57.84	+47:12:27.1	2.08 \pm 0.33	2.09 \pm 0.40	9.18 \pm 0.37	5.57 \pm 0.36	1.73 \pm 0.07	1.06 \pm 0.08	60.84 \pm 13.00	4.20 \pm 0.59	0.00000 \pm 0.00236
30	13:29:48.08	+47:12:22.9	3.63 \pm 0.42	2.67 \pm 0.24	19.55 \pm 0.26	8.28 \pm 0.25	3.43 \pm 0.10	1.96 \pm 0.09	152.16 \pm 13.00	9.14 \pm 0.59	0.01370 \pm 0.00621
31	13:29:48.80	+47:12:22.8	3.04 \pm 0.03	3.55 \pm 0.55	15.04 \pm 0.53	8.45 \pm 0.52	3.11 \pm 0.11	2.23 \pm 0.10	184.29 \pm 13.00	9.38 \pm 0.59	0.00489 \pm 0.00157
32	13:29:49.53	+47:12:22.6	3.53 \pm 0.03	4.25 \pm 0.30	19.03 \pm 0.30	12.46 \pm 0.30	4.32 \pm 0.11	2.75 \pm 0.11	63.33 \pm 13.00	5.10 \pm 0.59	0.01308 \pm 0.00278
33	13:29:50.25	+47:12:22.4	3.25 \pm 0.49	3.80 \pm 0.29	17.24 \pm 0.31	12.04 \pm 0.30	3.45 \pm 0.53	2.59 \pm 0.52	0.00 \pm 13.00	3.37 \pm 0.59	0.01004 \pm 0.00649
34	13:29:50.97	+47:12:22.3	2.70 \pm 0.10	4.70 \pm 0.55	14.63 \pm 0.55	12.60 \pm 0.56	3.20 \pm 0.27	2.04 \pm 0.27	14.38 \pm 13.00	6.89 \pm 0.59	0.00773 \pm 0.00251
35	13:29:51.69	+47:12:22.1	7.42 \pm 0.47	5.81 \pm 0.62	36.36 \pm 0.65	13.56 \pm 0.58	4.38 \pm 0.55	2.92 \pm 0.55	92.42 \pm 13.00	7.92 \pm 0.59	0.02603 \pm 0.00706
36	13:29:52.41	+47:12:21.9	6.47 \pm 0.30	5.37 \pm 0.04	31.56 \pm 0.05	15.43 \pm 0.04	4.42 \pm 0.11	2.77 \pm 0.11	106.36 \pm 13.00	5.23 \pm 0.59	0.02096 \pm 0.00507
37	13:29:53.14	+47:12:21.8	8.94 \pm 0.56	5.57 \pm 0.51	46.62 \pm 0.63	15.80 \pm 0.52	5.54 \pm 0.28	3.69 \pm 0.28	149.83 \pm 13.00	4.45 \pm 0.59	0.04334 \pm 0.01101
38	13:29:53.86	+47:12:21.6	14.87 \pm 0.60	9.17 \pm 0.58	73.39 \pm 0.78	24.92 \pm 0.62	7.90 \pm 0.55	5.91 \pm 0.55	105.98 \pm 13.00	6.14 \pm 0.59	0.06463 \pm 0.01434
39	13:29:54.58	+47:12:21.5	11.83 \pm 0.31	7.24 \pm 0.56	66.49 \pm 0.76	21.19 \pm 0.60	7.02 \pm 0.28	4.61 \pm 0.29	212.71 \pm 13.00	8.02 \pm 0.59	0.07998 \pm 0.01679
40	13:29:55.30	+47:12:21.3	11.02 \pm 0.53	8.10 \pm 0.54	62.21 \pm 0.72	22.01 \pm 0.58	7.32 \pm 0.11	5.07 \pm 0.11	179.39 \pm 13.00	8.19 \pm 0.59	0.07508 \pm 0.01720
41	13:29:56.03	+47:12:21.1	5.35 \pm 0.03	4.64 \pm 0.46	31.37 \pm 0.51	13.25 \pm 0.45	4.32 \pm 0.47	2.89 \pm 0.47	7.63 \pm 13.00	7.82 \pm 0.59	0.03639 \pm 0.00748
42	13:29:56.75	+47:12:21.0	8.48 \pm 0.51	5.24 \pm 0.26	50.10 \pm 0.35	16.97 \pm 0.29	5.69 \pm 0.26	3.86 \pm 0.25	61.97 \pm 13.00	5.18 \pm 0.59	0.06553 \pm 0.01595
43	13:29:57.47	+47:12:20.8	1.96 \pm 0.08	2.97 \pm 0.42	11.87 \pm 0.42	8.03 \pm 0.43	2.22 \pm 0.03	1.70 \pm 0.03	40.68 \pm 13.00	2.78 \pm 0.59	0.00834 \pm 0.00268
44	13:29:47.71	+47:12:16.6	1.53 \pm 0.41	2.39 \pm 0.27	10.92 \pm 0.26	7.11 \pm 0.26	2.12 \pm 0.46	1.31 \pm 0.49	81.06 \pm 13.00	7.17 \pm 0.59	0.01463 \pm 0.01362
45	13:29:48.43	+47:12:16.5	2.13 \pm 0.44	3.12 \pm 0.51	10.63 \pm 0.51	7.94 \pm 0.51	2.88 \pm 0.28	1.83 \pm 0.25	78.23 \pm 13.00	4.35 \pm 0.59	0.00053 \pm 0.00465
46	13:29:49.15	+47:12:16.3	3.57 \pm 0.48	4.68 \pm 0.54	17.90 \pm 0.55	13.74 \pm 0.55	4.19 \pm 0.50	3.21 \pm 0.51	41.67 \pm 13.00	3.46 \pm 0.59	0.00834 \pm 0.00539
47	13:29:49.87	+47:12:16.1	2.88 \pm 0.10	4.69 \pm 0.56	14.14 \pm 0.55	12.59 \pm 0.57	3.42 \pm 0.11	2.45 \pm 0.11	11.18 \pm 13.00	2.82 \pm 0.59	0.00370 \pm 0.00174
48	13:29:50.60	+47:12:16.0	6.90 \pm 0.52	6.18 \pm 0.56	37.54 \pm 0.64	17.50 \pm 0.58	5.19 \pm 0.11	3.34 \pm 0.11	0.00 \pm 13.00	4.22 \pm 0.59	0.03696 \pm 0.01033
49	13:29:51.32	+47:12:15.8	12.37 \pm 0.57	8.19 \pm 0.13	73.77 \pm 0.17	21.63 \pm 0.13	6.53 \pm 0.12	4.57 \pm 0.12	48.41 \pm 13.00	5.57 \pm 0.59	0.10399 \pm 0.02325
50	13:29:52.04	+47:12:15.7	25.53 \pm 0.71	20.67 \pm 0.37	132.87 \pm 0.51	58.85 \pm 0.43	16.06 \pm 0.14	14.06 \pm 0.15	99.08 \pm 13.00	2.58 \pm 0.59	0.14240 \pm 0.02970
51	13:29:52.76	+47:12:15.5	17.55 \pm 0.63	8.64 \pm 0.32	99.61 \pm 0.47	25.19 \pm 0.35	7.92 \pm 0.62	5.24 \pm 0.58	94.15 \pm 13.00	3.84 \pm 0.59	0.12807 $\pm</$

TABLE 1 — *Continued*

ID	Equatorial Coordinates	H β	[NII] λ 6548	H α	[NII] λ 6584	[SII] λ 6717	[SII] λ 6731	Σ_{H_2}	Σ_{HI}	Σ_{SFR}
54	13:29:54.93 +47:12:15.0	23.08 \pm 0.66	11.38 \pm 0.60	141.86 \pm 0.98	33.01 \pm 0.68	11.29 \pm 0.31	7.26 \pm 0.30	257.65 \pm 13.00	8.36 \pm 0.59	0.22487 \pm 0.04699
55	13:29:55.65 +47:12:14.8	8.25 \pm 0.49	9.65 \pm 0.54	56.70 \pm 0.69	26.75 \pm 0.59	8.89 \pm 0.52	6.48 \pm 0.51	215.44 \pm 13.00	6.27 \pm 0.59	0.10967 \pm 0.02617
56	13:29:56.37 +47:12:14.7	13.18 \pm 0.55	7.18 \pm 0.30	63.25 \pm 0.38	18.86 \pm 0.30	6.49 \pm 0.04	4.07 \pm 0.03	26.45 \pm 13.00	6.03 \pm 0.59	0.05035 \pm 0.01129
57	13:29:57.09 +47:12:14.5	3.21 \pm 0.41	3.70 \pm 0.49	18.44 \pm 0.51	9.33 \pm 0.49	2.95 \pm 0.09	1.97 \pm 0.10	20.06 \pm 13.00	3.09 \pm 0.59	0.01577 \pm 0.00748
58	13:29:57.82 +47:12:14.4	0.96 \pm 0.03	2.05 \pm 0.44	6.47 \pm 0.43	6.09 \pm 0.44	1.69 \pm 0.08	0.90 \pm 0.09	35.74 \pm 13.00	1.91 \pm 0.59	0.00244 \pm 0.00206
59	13:29:48.06 +47:12:10.2	1.83 \pm 0.40	3.43 \pm 0.10	10.61 \pm 0.11	10.08 \pm 0.11	3.42 \pm 0.04	2.09 \pm 0.03	41.95 \pm 13.00	5.31 \pm 0.59	0.00479 \pm 0.00670
60	13:29:48.78 +47:12:10.0	4.43 \pm 0.48	4.85 \pm 0.44	19.58 \pm 0.47	14.39 \pm 0.48	4.72 \pm 0.27	2.62 \pm 0.27	18.68 \pm 13.00	3.84 \pm 0.59	0.00508 \pm 0.00357
61	13:29:49.50 +47:12:09.9	6.98 \pm 0.04	3.74 \pm 0.28	33.41 \pm 0.33	12.40 \pm 0.30	4.06 \pm 0.28	2.49 \pm 0.26	9.03 \pm 13.00	3.75 \pm 0.59	0.02137 \pm 0.00434
62	13:29:50.22 +47:12:09.7	4.86 \pm 0.28	5.11 \pm 0.34	24.00 \pm 0.32	13.41 \pm 0.33	3.10 \pm 0.57	1.93 \pm 0.54	16.93 \pm 13.00	3.85 \pm 0.59	0.01401 \pm 0.00405
63	13:29:50.94 +47:12:09.5	12.46 \pm 0.61	8.64 \pm 0.62	59.86 \pm 0.77	27.93 \pm 0.69	7.67 \pm 0.04	5.02 \pm 0.04	0.00 \pm 13.00	2.96 \pm 0.59	0.04723 \pm 0.01109
64	13:29:51.67 +47:12:09.4	58.16 \pm 0.92	23.02 \pm 0.75	295.17 \pm 1.33	71.18 \pm 0.89	22.09 \pm 0.40	15.89 \pm 0.39	115.19 \pm 13.00	3.12 \pm 0.59	0.31111 \pm 0.06310
65	13:29:52.39 +47:12:09.2	35.95 \pm 0.84	22.21 \pm 0.80	210.78 \pm 1.21	65.77 \pm 0.92	20.49 \pm 0.43	13.35 \pm 0.40	165.21 \pm 13.00	4.72 \pm 0.59	0.30470 \pm 0.06276
66	13:29:53.11 +47:12:09.0	16.54 \pm 0.67	11.53 \pm 0.37	98.18 \pm 0.48	34.93 \pm 0.40	9.19 \pm 0.68	6.66 \pm 0.69	283.91 \pm 13.00	6.02 \pm 0.59	0.14039 \pm 0.03061
67	13:29:53.83 +47:12:08.9	17.90 \pm 0.65	9.28 \pm 0.36	94.99 \pm 0.48	26.10 \pm 0.38	7.14 \pm 0.66	4.62 \pm 0.66	138.33 \pm 13.00	5.71 \pm 0.59	0.10356 \pm 0.02229
68	13:29:54.55 +47:12:08.7	69.80 \pm 1.12	19.44 \pm 0.18	332.04 \pm 0.31	57.90 \pm 0.20	13.33 \pm 0.42	11.14 \pm 0.43	75.14 \pm 13.00	8.67 \pm 0.59	0.30342 \pm 0.06149
69	13:29:55.28 +47:12:08.6	11.87 \pm 0.54	7.38 \pm 0.29	75.56 \pm 0.41	21.49 \pm 0.32	7.10 \pm 0.54	4.91 \pm 0.54	424.89 \pm 13.00	5.93 \pm 0.59	0.12489 \pm 0.02779
70	13:29:56.00 +47:12:08.4	6.41 \pm 0.11	6.04 \pm 0.28	36.01 \pm 0.33	16.59 \pm 0.30	6.01 \pm 0.27	4.24 \pm 0.27	135.68 \pm 13.00	7.57 \pm 0.59	0.03844 \pm 0.00791
71	13:29:56.72 +47:12:08.2	3.68 \pm 0.03	4.31 \pm 0.11	21.22 \pm 0.12	11.73 \pm 0.12	4.34 \pm 0.53	3.00 \pm 0.51	39.64 \pm 13.00	5.71 \pm 0.59	0.01996 \pm 0.00404
72	13:29:57.44 +47:12:08.1	1.65 \pm 0.42	2.94 \pm 0.51	8.93 \pm 0.47	8.20 \pm 0.48	2.36 \pm 0.09	2.14 \pm 0.11	0.00 \pm 13.00	3.02 \pm 0.59	0.00065 \pm 0.00578
73	13:29:47.68 +47:12:03.9	2.65 \pm 0.25	2.69 \pm 0.11	10.88 \pm 0.10	8.92 \pm 0.10	2.51 \pm 0.25	1.42 \pm 0.22	13.58 \pm 13.00	3.73 \pm 0.59	0.00000 \pm 0.00139
74	13:29:48.40 +47:12:03.7	3.99 \pm 0.10	3.99 \pm 0.52	18.84 \pm 0.54	12.08 \pm 0.53	3.02 \pm 0.03	2.51 \pm 0.03	18.86 \pm 13.00	5.26 \pm 0.59	0.00692 \pm 0.00196
75	13:29:49.12 +47:12:03.6	21.85 \pm 0.60	13.81 \pm 0.51	127.65 \pm 0.79	41.67 \pm 0.59	10.76 \pm 0.29	8.06 \pm 0.28	37.46 \pm 13.00	5.51 \pm 0.59	0.17886 \pm 0.03730
76	13:29:49.85 +47:12:03.4	5.23 \pm 0.27	5.26 \pm 0.32	29.37 \pm 0.34	14.54 \pm 0.32	4.17 \pm 0.58	2.92 \pm 0.54	48.04 \pm 13.00	4.64 \pm 0.59	0.02933 \pm 0.00722
77	13:29:50.57 +47:12:03.3	13.72 \pm 0.60	11.67 \pm 0.35	92.03 \pm 0.45	34.34 \pm 0.38	10.55 \pm 0.33	7.27 \pm 0.32	59.66 \pm 13.00	4.04 \pm 0.59	0.17450 \pm 0.03844
78	13:29:51.29 +47:12:03.1	52.27 \pm 0.95	24.76 \pm 0.83	279.54 \pm 1.34	74.74 \pm 0.96	22.80 \pm 0.83	15.91 \pm 0.81	293.62 \pm 13.00	5.03 \pm 0.59	0.33123 \pm 0.06744
79	13:29:52.01 +47:12:02.9	45.60 \pm 0.94	31.76 \pm 0.93	258.87 \pm 1.35	95.92 \pm 1.09	27.18 \pm 0.49	20.77 \pm 0.48	507.32 \pm 13.00	4.69 \pm 0.59	0.35022 \pm 0.07165
80	13:29:52.73 +47:12:02.8	51.54 \pm 0.97	31.66 \pm 0.94	287.30 \pm 1.40	93.18 \pm 1.09	22.13 \pm 0.48	16.19 \pm 0.49	302.17 \pm 13.00	4.85 \pm 0.59	0.37422 \pm 0.07629
81	13:29:53.46 +47:12:02.6	14.38 \pm 0.73	11.71 \pm 0.73	81.39 \pm 0.84	34.69 \pm 0.78	9.00 \pm 0.44	6.02 \pm 0.42	198.96 \pm 13.00	6.67 \pm 0.59	0.10215 \pm 0.02346
82	13:29:54.18 +47:12:02.4	27.59 \pm 0.83	10.82 \pm 0.80	128.34 \pm 1.07	34.50 \pm 0.88	9.39 \pm 0.17	6.77 \pm 0.17	116.76 \pm 13.00	7.53 \pm 0.59	0.10491 \pm 0.02216
83	13:29:54.90 +47:12:02.3	53.17 \pm 0.84	19.84 \pm 0.38	331.38 \pm 0.72	57.59 \pm 0.44	19.71 \pm 0.15	13.89 \pm 0.15	150.05 \pm 13.00	7.46 \pm 0.59	0.55634 \pm 0.11268
84	13:29:55.62 +47:12:02.1	15.96 \pm 0.04	10.31 \pm 0.55	105.20 \pm 0.84	28.99 \pm 0.61	8.97 \pm 0.01	6.70 \pm 0.01	541.34 \pm 13.00	8.80 \pm 0.59	0.19294 \pm 0.03876
85	13:29:56.34 +47:12:01.9	24.62 \pm 0.69	12.27 \pm 0.62	123.21 \pm 0.92	36.61 \pm 0.71	12.27 \pm 0.32	9.32 \pm 0.32	82.01 \pm 13.00	6.94 \pm 0.59	0.11955 \pm 0.02505
86	13:29:57.07 +47:12:01.8	6.86 \pm 0.27	6.12 \pm 0.28	37.55 \pm 0.33	19.01 \pm 0.31	5.99 \pm 0.11	3.91 \pm 0.11	19.73 \pm 13.00	4.55 \pm 0.59	0.03766 \pm 0.00843
87	13:29:57.79 +47:12:01.6	2.30 \pm 0.42	2.75 \pm 0.45	9.66 \pm 0.47	7.42 \pm 0.46	2.67 \pm 0.11	1.42 \pm 0.08	5.61 \pm 13.00	3.66 \pm 0.59	0.00000 \pm 0.00260
88	13:29:48.03 +47:11:57.4	2.17 \pm 0.46	2.56 \pm 0.48	10.91 \pm 0.49	8.44 \pm 0.50	2.64 \pm 0.50	2.04 \pm 0.48	2.64 \pm 13.00	3.15 \pm 0.59	0.00101 \pm 0.00495
89	13:29:48.75 +47:11:57.3	3.46 \pm 0.03	3.25 \pm 0.11	14.67 \pm 0.11	9.16 \pm 0.11	2.73 \pm 0.44	2.54 \pm 0.49	6.70 \pm 13.00	5.33 \pm 0.59	0.00014 \pm 0.00027
90	13:29:49.47 +47:11:57.1	5.55 \pm 0.49	5.01 \pm 0.59	28.01 \pm 0.63	16.00 \pm 0.62	3.56 \pm 0.27	2.76 \pm 0.31	11.76 \pm 13.00	2.42 \pm 0.59	0.01956 \pm 0.00670
91	13:29:50.19 +47:11:57.0	31.60 \pm 0.05	18.98 \pm 0.61	192.13 \pm 0.95	59.01 \pm 0.71	17.93 \pm 0.37	13.14 \pm 0.36	176.44 \pm 13.00	4.48 \pm 0.59	0.30077 \pm 0.06025
92	13:29:50.92 +47:11:56.8	45.84 \pm 0.89	29.61 \pm 0.84	247.21 \pm 1.25	90.73 \pm 0.99	25.74 \pm 0.44	18.36 \pm 0.43	605.72 \pm 13.00	7.25 \pm 0.59	0.29722 \pm 0.06067
93	13:29:51.64 +47:11:56.6	38.93 \pm 1.04	27.17 \pm 1.10	221.49 \pm 1.38	83.86 \pm 1.23	19.65 \pm 0.23	14.92 \pm 0.22	550.31 \pm 13.00	5.72 \pm 0.59	0.29965 \pm 0.06225
94	13:29:52.36 +47:11:56.5	43.30 \pm 1.14	91.64 \pm 0.74	220.27 \pm 0.79	278.90 \pm 0.91	57.15 \pm 0.29	44.82 \pm 0.29	392.05 \pm 13.00	3.84 \pm 0.59	0.20632 \pm 0.04316
95	13:29:53.08 +47:11:56.3	43.47 \pm 1.08	55.62 \pm 1.20	213.43 \pm 1.39	171.49 \pm 1.42	36.72 \pm 0.65	27.61 \pm 0.67	143.95 \pm 13.00	5.23 \pm 0.59	0.20577 \pm 0.04258
96	13:29:53.80 +47:11:56.2	39.75 \pm 0.91	19.66 \pm 0.80	213.20 \pm 1.10	60.59 \pm 0.89	15.07 \pm 0.47	10.36 \pm 0.45	87.01 \pm 13.00	5.37 \pm 0.59	0.25174 \pm 0.05180
97	13:29:54.53 +47:11:56.0	19.26 \pm 0.72	13.40 \pm 0.79	105.76 \pm 0.97	38.36 \pm 0.85	10.29 \pm 0.16	6.79 \pm 0.16	134.66 \pm 13.00	4.34 \pm 0.59	0.12638 \pm 0.02732
98	13:29:55.25 +47:11:55.8	19.00 \pm 0.35	13.20 \pm 0.67	110.51 \pm 0.91	38.54 \pm 0.74	11.97 \pm 0.35	8.65 \pm 0.34	216.58 \pm 13.00	6.38 \pm 0.59	0.15191 \pm 0.03106
99	13:29:55.97 +47:11:55.7	47.55 \pm 0.76	14.66 \pm 0.32	213.11 \pm 0.57	45.70 \pm 0.37	14.98 \pm 0.59	11.68 \pm 0.58	378.85 \pm 13.00	7.82 \pm 0.59	0.16615 \pm 0.03371
100	13:29:56.69 +47:11:55.5	21.19 \pm 0.34	9.29 \pm 0.31	102.52 \pm 0.45	28.00 \pm 0.34	8.65 \pm 0.12	6.52 \pm 0.12	63.48 \pm 13.00	4.32 \pm 0.59	0.09002 \pm 0.01830
101	13:29:57.41 +47:11:55.3	15.09 \pm 0.52	8.23 \pm 0.27	72.32 \pm 0.37	23.06 \pm 0.29	6.57 \pm 0.10	4.54 \pm 0.10	41.05 \pm 13.00	4.32 \pm 0.59	0.05891 \pm 0.01270
102	13:29:47.65 +47:11:51.2	2.08 \pm 0.41	4.55 \pm 0.62	9.41 \pm 0.47	8.06 \pm 0.48	1.87 \pm 0.41	1.54 \pm 0.46	45.82 \pm 13.00	2.94 \pm 0.59	0.00000 \pm 0.00322
103	13:29:48.38 +47:11:51.0	2.29 \pm 0.42	2.98 \pm 0.26	11.49 \pm 0.26	8.56 \pm 0.26	2.89 \pm 0.26	1.81 \pm 0.23	21.23 \pm 13.00	4.88 \pm 0.59	0.00161 \pm 0.00451
104	13:29:49.10 +47:11:50.8	4.52 \pm 0.11	5.10 \pm 0.61	24.66 \pm 0.60	13.74 \pm 0.58	4.24 \pm 0.55	2.67 \pm 0.53	0.00 \pm 13.00	6.11 \pm 0.59	0.02095 \pm 0.00474
105	13:29:49.82 +47:11:50.7	26.11 \pm 0.74	12.89 \pm 0.71	130.83 \pm 0.97	38.71 \pm 0.77	9.13 \pm 0.68	7.04 \pm 0.67	266.10 \pm 13.00	5.80 \pm 0.59	0.12798 \pm 0.02681
106	13:29:50.54 +47:11:50.5	33.12 \pm 0.78	22.43 \pm 0.68	194.78 \pm 0.99	68.60 \pm 0.79	19.04<				

TABLE 1 — *Continued*

ID	Equatorial Coordinates	H β	[NII] λ 6548	H α	[NII] λ 6584	[SII] λ 6717	[SII] λ 6731	Σ_{H_2}	Σ_{HI}	Σ_{SFR}
111	13:29:54.15 +47:11:49.7	44.26 \pm 0.92	24.15 \pm 0.93	242.37 \pm 1.31	74.55 \pm 1.06	17.43 \pm 0.06	12.62 \pm 0.06	104.72 \pm 13.00	3.29 \pm 0.59	0.30160 \pm 0.06177
112	13:29:54.87 +47:11:49.5	41.37 \pm 0.77	16.17 \pm 0.72	198.66 \pm 1.10	45.77 \pm 0.79	13.42 \pm 0.38	9.42 \pm 0.37	141.08 \pm 13.00	4.97 \pm 0.59	0.18111 \pm 0.03696
113	13:29:55.59 +47:11:49.4	76.13 \pm 1.02	30.47 \pm 0.72	379.38 \pm 1.24	90.62 \pm 0.84	23.49 \pm 0.42	17.92 \pm 0.41	319.07 \pm 13.00	6.77 \pm 0.59	0.38663 \pm 0.07808
114	13:29:56.32 +47:11:49.2	23.41 \pm 0.64	11.13 \pm 0.61	130.04 \pm 0.91	33.53 \pm 0.67	11.15 \pm 0.13	7.69 \pm 0.13	109.58 \pm 13.00	6.82 \pm 0.59	0.16213 \pm 0.03382
115	13:29:57.04 +47:11:49.1	5.71 \pm 0.10	4.89 \pm 0.48	27.81 \pm 0.51	13.94 \pm 0.49	3.63 \pm 0.11	2.61 \pm 0.10	9.44 \pm 13.00	4.70 \pm 0.59	0.01705 \pm 0.00372
116	13:29:57.76 +47:11:48.9	3.55 \pm 0.36	4.69 \pm 0.49	11.76 \pm 0.48	11.76 \pm 0.48	3.83 \pm 0.40	2.51 \pm 0.40	27.71 \pm 13.00	4.88 \pm 0.59	0.01006 \pm 0.00468
117	13:29:48.00 +47:11:44.7	5.53 \pm 0.42	3.09 \pm 0.44	22.68 \pm 0.50	9.72 \pm 0.46	3.17 \pm 0.08	1.90 \pm 0.09	24.80 \pm 13.00	3.80 \pm 0.59	0.00489 \pm 0.00264
118	13:29:48.72 +47:11:44.6	3.33 \pm 0.23	3.97 \pm 0.56	16.91 \pm 0.54	11.78 \pm 0.54	3.50 \pm 0.03	2.44 \pm 0.04	9.04 \pm 13.00	5.95 \pm 0.59	0.00777 \pm 0.00323
119	13:29:49.44 +47:11:44.4	16.87 \pm 0.61	8.84 \pm 0.60	83.85 \pm 0.81	26.61 \pm 0.67	6.91 \pm 0.58	5.39 \pm 0.59	63.01 \pm 13.00	6.69 \pm 0.59	0.07672 \pm 0.01665
120	13:29:50.17 +47:11:44.2	22.48 \pm 0.64	20.71 \pm 0.68	157.02 \pm 0.98	63.22 \pm 0.80	17.64 \pm 0.66	12.42 \pm 0.65	405.33 \pm 13.00	9.21 \pm 0.59	0.33435 \pm 0.06978
121	13:29:50.89 +47:11:44.1	34.13 \pm 0.45	20.93 \pm 0.84	173.71 \pm 1.12	65.81 \pm 0.96	16.34 \pm 0.18	12.14 \pm 0.18	244.02 \pm 13.00	7.90 \pm 0.59	0.17990 \pm 0.03642
122	13:29:51.61 +47:11:43.9	52.87 \pm 1.09	29.90 \pm 1.12	269.89 \pm 1.41	93.14 \pm 1.24	20.07 \pm 1.14	14.65 \pm 1.09	111.63 \pm 13.00	3.26 \pm 0.59	0.28729 \pm 0.05880
123	13:29:52.33 +47:11:43.7	31.55 \pm 0.10	94.01 \pm 1.83	131.59 \pm 1.69	279.00 \pm 2.05	42.75 \pm 0.37	38.12 \pm 0.40	228.58 \pm 13.00	3.37 \pm 0.59	0.07390 \pm 0.01502
124	13:29:53.05 +47:11:43.6	53.33 \pm 1.59	297.73 \pm 2.31	312.51 \pm 2.48	863.73 \pm 2.83	110.81 \pm 0.14	122.21 \pm 0.16	184.59 \pm 13.00	2.61 \pm 0.59	0.40826 \pm 0.08647
125	13:29:53.78 +47:11:43.4	33.39 \pm 1.02	21.21 \pm 0.62	158.03 \pm 0.68	69.96 \pm 0.67	14.83 \pm 1.16	13.79 \pm 1.30	111.82 \pm 13.00	3.12 \pm 0.59	0.13715 \pm 0.02885
126	13:29:54.50 +47:11:43.3	40.50 \pm 0.89	19.78 \pm 0.88	214.77 \pm 1.23	65.14 \pm 1.00	16.71 \pm 0.47	13.42 \pm 0.48	200.35 \pm 13.00	4.56 \pm 0.59	0.24713 \pm 0.05075
127	13:29:55.22 +47:11:43.1	28.82 \pm 0.69	15.65 \pm 0.68	158.04 \pm 0.99	48.74 \pm 0.77	14.58 \pm 0.36	9.35 \pm 0.34	251.45 \pm 13.00	7.79 \pm 0.59	0.19359 \pm 0.03998
128	13:29:55.94 +47:11:42.9	24.83 \pm 0.69	13.15 \pm 0.65	132.91 \pm 0.93	40.00 \pm 0.73	11.76 \pm 0.14	8.57 \pm 0.13	347.01 \pm 13.00	10.39 \pm 0.59	0.15226 \pm 0.03181
129	13:29:56.66 +47:11:42.8	5.86 \pm 0.49	4.59 \pm 0.45	30.47 \pm 0.51	15.05 \pm 0.48	4.17 \pm 0.10	3.00 \pm 0.10	31.71 \pm 13.00	6.88 \pm 0.59	0.02439 \pm 0.00760
130	13:29:57.39 +47:11:42.6	3.87 \pm 0.37	4.09 \pm 0.50	17.72 \pm 0.49	10.82 \pm 0.48	3.74 \pm 0.47	2.04 \pm 0.44	7.14 \pm 13.00	4.63 \pm 0.59	0.00480 \pm 0.00322
131	13:29:47.63 +47:11:38.4	9.52 \pm 0.43	4.35 \pm 0.44	39.80 \pm 0.55	13.48 \pm 0.46	4.09 \pm 0.09	2.66 \pm 0.09	33.53 \pm 13.00	3.78 \pm 0.59	0.01771 \pm 0.00441
132	13:29:48.35 +47:11:38.3	2.37 \pm 0.38	3.31 \pm 0.45	10.41 \pm 0.45	10.57 \pm 0.48	2.58 \pm 0.41	1.98 \pm 0.45	0.00 \pm 13.00	2.68 \pm 0.59	0.00000 \pm 0.00272
133	13:29:49.07 +47:11:38.1	5.07 \pm 0.03	5.60 \pm 0.31	24.88 \pm 0.31	15.18 \pm 0.31	5.08 \pm 0.54	4.25 \pm 0.58	65.40 \pm 13.00	3.90 \pm 0.59	0.01461 \pm 0.00302
134	13:29:49.79 +47:11:38.0	19.41 \pm 0.60	13.51 \pm 0.61	121.07 \pm 0.88	40.05 \pm 0.70	12.92 \pm 0.33	8.35 \pm 0.31	364.64 \pm 13.00	7.48 \pm 0.59	0.19699 \pm 0.04146
135	13:29:50.51 +47:11:37.8	39.59 \pm 0.16	19.72 \pm 0.62	242.84 \pm 1.00	58.44 \pm 0.71	18.22 \pm 0.71	13.43 \pm 0.71	549.48 \pm 13.00	7.63 \pm 0.59	0.39052 \pm 0.07825
136	13:29:51.24 +47:11:37.6	20.90 \pm 0.73	15.59 \pm 0.81	109.13 \pm 0.97	46.04 \pm 0.88	10.33 \pm 0.42	7.67 \pm 0.41	197.14 \pm 13.00	5.35 \pm 0.59	0.11599 \pm 0.02490
137	13:29:51.96 +47:11:37.5	34.98 \pm 0.92	28.79 \pm 1.05	180.33 \pm 1.24	85.04 \pm 1.16	17.21 \pm 0.90	12.44 \pm 0.88	139.93 \pm 13.00	2.52 \pm 0.59	0.19285 \pm 0.04010
138	13:29:52.68 +47:11:37.3	51.78 \pm 1.16	47.95 \pm 1.33	233.74 \pm 1.47	144.48 \pm 1.48	26.86 \pm 0.72	21.64 \pm 0.75	59.76 \pm 13.00	2.43 \pm 0.59	0.18638 \pm 0.03835
139	13:29:53.40 +47:11:37.1	17.19 \pm 0.83	23.16 \pm 1.17	99.68 \pm 1.20	70.09 \pm 1.26	13.53 \pm 1.24	12.06 \pm 1.26	168.95 \pm 13.00	4.00 \pm 0.59	0.13487 \pm 0.03049
140	13:29:54.12 +47:11:37.0	47.97 \pm 0.95	25.67 \pm 0.96	242.75 \pm 1.27	75.80 \pm 1.06	17.55 \pm 0.97	14.20 \pm 0.99	224.21 \pm 13.00	4.11 \pm 0.59	0.25228 \pm 0.05157
141	13:29:54.84 +47:11:36.8	21.30 \pm 0.61	20.78 \pm 0.67	138.97 \pm 0.92	63.76 \pm 0.79	19.25 \pm 0.69	14.30 \pm 0.68	343.93 \pm 13.00	6.83 \pm 0.59	0.25237 \pm 0.05273
142	13:29:55.57 +47:11:36.7	24.93 \pm 0.67	13.33 \pm 0.63	126.29 \pm 0.89	40.60 \pm 0.71	11.85 \pm 0.13	9.69 \pm 0.14	342.97 \pm 13.00	9.15 \pm 0.59	0.12642 \pm 0.02639
143	13:29:56.29 +47:11:36.5	8.21 \pm 0.52	5.80 \pm 0.57	36.81 \pm 0.64	17.43 \pm 0.60	3.42 \pm 0.11	2.94 \pm 0.12	11.85 \pm 13.00	4.80 \pm 0.59	0.01996 \pm 0.00562
144	13:29:57.01 +47:11:36.3	21.35 \pm 0.54	8.52 \pm 0.27	92.11 \pm 0.40	25.37 \pm 0.30	7.98 \pm 0.26	5.33 \pm 0.26	23.49 \pm 13.00	4.13 \pm 0.59	0.05964 \pm 0.01244
145	13:29:57.73 +47:11:36.2	5.02 \pm 0.43	4.21 \pm 0.47	21.90 \pm 0.50	10.88 \pm 0.47	3.58 \pm 0.03	2.67 \pm 0.03	12.02 \pm 13.00	3.37 \pm 0.59	0.00650 \pm 0.00325
146	13:29:47.97 +47:11:32.0	2.02 \pm 0.39	2.53 \pm 0.48	8.95 \pm 0.44	6.90 \pm 0.45	2.18 \pm 0.01	1.16 \pm 0.01	0.00 \pm 13.00	3.57 \pm 0.59	0.00000 \pm 0.00286
147	13:29:48.69 +47:11:31.8	3.03 \pm 0.42	4.86 \pm 0.30	15.40 \pm 0.27	10.42 \pm 0.27	2.97 \pm 0.45	2.35 \pm 0.48	24.25 \pm 13.00	3.46 \pm 0.59	0.00620 \pm 0.00476
148	13:29:49.42 +47:11:31.7	11.43 \pm 0.46	5.93 \pm 0.54	59.45 \pm 0.69	18.85 \pm 0.58	6.73 \pm 0.55	4.56 \pm 0.53	195.48 \pm 13.00	6.85 \pm 0.59	0.05770 \pm 0.01285
149	13:29:50.14 +47:11:31.5	18.81 \pm 0.28	18.69 \pm 0.60	160.08 \pm 0.93	57.74 \pm 0.71	18.64 \pm 0.60	13.53 \pm 0.58	960.65 \pm 13.00	8.22 \pm 0.59	0.53224 \pm 0.10787
150	13:29:50.86 +47:11:31.3	27.28 \pm 0.73	16.59 \pm 0.78	134.51 \pm 0.97	46.95 \pm 0.84	11.53 \pm 0.05	10.57 \pm 0.06	210.28 \pm 13.00	6.90 \pm 0.59	0.12702 \pm 0.02649
151	13:29:51.58 +47:11:31.2	18.39 \pm 0.72	13.89 \pm 0.79	103.37 \pm 0.96	43.01 \pm 0.88	10.07 \pm 0.05	8.05 \pm 0.06	206.44 \pm 13.00	8.99 \pm 0.59	0.13044 \pm 0.02837
152	13:29:52.30 +47:11:31.0	58.93 \pm 0.52	36.58 \pm 0.21	303.30 \pm 0.29	106.63 \pm 0.24	21.76 \pm 0.19	17.22 \pm 0.20	118.99 \pm 13.00	5.56 \pm 0.59	0.33033 \pm 0.06634
153	13:29:53.03 +47:11:30.9	20.57 \pm 0.78	15.60 \pm 0.92	113.46 \pm 1.07	47.69 \pm 1.00	9.54 \pm 0.06	8.00 \pm 0.07	259.97 \pm 13.00	5.49 \pm 0.59	0.13789 \pm 0.02985
154	13:29:53.75 +47:11:30.7	35.88 \pm 0.89	20.51 \pm 0.93	189.93 \pm 1.20	61.79 \pm 1.03	13.25 \pm 0.19	10.98 \pm 0.19	282.84 \pm 13.00	5.33 \pm 0.59	0.21648 \pm 0.04479
155	13:29:54.47 +47:11:30.5	27.25 \pm 0.66	18.74 \pm 0.70	172.92 \pm 1.01	54.67 \pm 0.80	15.27 \pm 0.69	11.13 \pm 0.71	349.80 \pm 13.00	5.45 \pm 0.59	0.29727 \pm 0.06134
156	13:29:55.19 +47:11:30.4	14.31 \pm 0.61	10.51 \pm 0.60	69.90 \pm 0.68	29.55 \pm 0.62	8.07 \pm 0.62	6.03 \pm 0.64	342.27 \pm 13.00	5.06 \pm 0.59	0.05939 \pm 0.01331
157	13:29:55.91 +47:11:30.2	5.58 \pm 0.04	4.39 \pm 0.13	24.51 \pm 0.13	12.78 \pm 0.12	2.62 \pm 0.03	2.75 \pm 0.04	37.86 \pm 13.00	4.25 \pm 0.59	0.00883 \pm 0.00180
158	13:29:56.64 +47:11:30.0	4.99 \pm 0.03	5.19 \pm 0.26	22.39 \pm 0.28	13.73 \pm 0.28	4.19 \pm 0.47	2.59 \pm 0.45	8.06 \pm 13.00	6.01 \pm 0.59	0.00798 \pm 0.00169
159	13:29:57.36 +47:11:29.9	5.69 \pm 0.43	4.69 \pm 0.49	21.51 \pm 0.50	11.65 \pm 0.48	4.11 \pm 0.49	2.51 \pm 0.44	7.33 \pm 13.00	4.75 \pm 0.59	0.00164 \pm 0.00196
160	13:29:47.60 +47:11:25.7	4.28 \pm 0.39	3.44 \pm 0.47	17.91 \pm 0.46	8.07 \pm 0.44	3.11 \pm 0.09	2.09 \pm 0.09	27.17 \pm 13.00	4.45 \pm 0.59	0.00212 \pm 0.00245
161	13:29:48.32 +47:11:25.5	2.61 \pm 0.33	2.13 \pm 0.43	9.94 \pm 0.43	6.92 \pm 0.44	1.95 \pm 0.19	1.11 \pm 0.20	16.81 \pm 13.00	4.01 \pm 0.59	0.00000 \pm 0.00155
162	13:29:49.04 +47:11:25.4	3.88 \pm 0.09	3.85 \pm 0.45	21.43 \pm 0.47	9.78 \pm 0.44	3.07 \pm 0.04	2.23 \pm 0.03	10.50 \pm 13.00	3.65 \pm 0.59	0.01740 \pm 0.00394
163										

TABLE 1 — *Continued*

ID	Equatorial Coordinates	H β	[NII] λ 6548	H α	[NII] λ 6584	[SII] λ 6717	[SII] λ 6731	Σ_{H_2}	Σ_{HI}	Σ_{SFR}
168	13:29:53.37 +47:11:24.4	38.86 \pm 0.75	20.16 \pm 0.75	199.20 \pm 1.08	56.64 \pm 0.84	15.40 \pm 0.39	10.53 \pm 0.38	408.54 \pm 13.00	8.02 \pm 0.59	0.21135 \pm 0.04317
169	13:29:54.10 +47:11:24.2	40.76 \pm 0.72	22.78 \pm 0.63	214.34 \pm 0.95	67.59 \pm 0.73	19.47 \pm 0.15	15.09 \pm 0.15	339.39 \pm 13.00	4.34 \pm 0.59	0.24194 \pm 0.04924
170	13:29:54.82 +47:11:24.1	7.50 \pm 0.01	6.41 \pm 0.31	39.94 \pm 0.35	20.25 \pm 0.33	5.14 \pm 0.56	3.91 \pm 0.57	147.60 \pm 13.00	5.97 \pm 0.59	0.03781 \pm 0.00762
171	13:29:55.54 +47:11:23.9	4.65 \pm 0.45	5.00 \pm 0.46	21.70 \pm 0.48	15.32 \pm 0.51	3.57 \pm 0.03	2.86 \pm 0.04	5.03 \pm 13.00	5.19 \pm 0.59	0.00903 \pm 0.00424
172	13:29:56.26 +47:11:23.8	7.65 \pm 0.44	4.25 \pm 0.50	32.31 \pm 0.56	13.73 \pm 0.51	4.11 \pm 0.48	3.08 \pm 0.48	3.06 \pm 13.00	4.96 \pm 0.59	0.01291 \pm 0.00382
173	13:29:56.98 +47:11:23.6	8.33 \pm 0.43	4.98 \pm 0.40	35.92 \pm 0.48	13.52 \pm 0.43	4.72 \pm 0.09	3.15 \pm 0.09	0.00 \pm 13.00	8.44 \pm 0.59	0.01678 \pm 0.00443
174	13:29:57.70 +47:11:23.4	8.67 \pm 0.44	5.78 \pm 0.47	44.94 \pm 0.58	19.72 \pm 0.51	8.17 \pm 0.27	5.02 \pm 0.25	44.23 \pm 13.00	5.56 \pm 0.59	0.04064 \pm 0.00970
175	13:29:47.95 +47:11:19.3	1.61 \pm 0.35	2.32 \pm 0.45	7.06 \pm 0.40	5.31 \pm 0.41	1.64 \pm 0.38	0.91 \pm 0.39	43.73 \pm 13.00	4.22 \pm 0.59	0.00000 \pm 0.00243
176	13:29:48.67 +47:11:19.1	1.76 \pm 0.36	2.51 \pm 0.50	9.11 \pm 0.44	5.43 \pm 0.44	1.19 \pm 0.08	0.50 \pm 0.06	12.10 \pm 13.00	3.08 \pm 0.59	0.00000 \pm 0.00435
177	13:29:49.39 +47:11:18.9	4.26 \pm 0.44	4.92 \pm 0.54	20.75 \pm 0.53	12.73 \pm 0.53	3.32 \pm 0.03	2.72 \pm 0.03	34.88 \pm 13.00	3.68 \pm 0.59	0.01004 \pm 0.00476
178	13:29:50.11 +47:11:18.8	23.57 \pm 0.56	12.86 \pm 0.29	107.69 \pm 0.42	37.53 \pm 0.33	12.10 \pm 0.55	9.25 \pm 0.56	576.38 \pm 13.00	7.10 \pm 0.59	0.08253 \pm 0.01708
179	13:29:50.83 +47:11:18.6	6.21 \pm 0.10	6.12 \pm 0.52	39.51 \pm 0.61	19.14 \pm 0.56	5.56 \pm 0.29	4.24 \pm 0.29	438.05 \pm 13.00	4.98 \pm 0.59	0.06008 \pm 0.01244
180	13:29:51.55 +47:11:18.4	7.64 \pm 0.11	8.30 \pm 0.60	35.59 \pm 0.64	19.78 \pm 0.61	5.26 \pm 0.04	3.05 \pm 0.04	135.02 \pm 13.00	3.28 \pm 0.59	0.02147 \pm 0.00457
181	13:29:52.28 +47:11:18.3	10.04 \pm 0.04	8.02 \pm 0.62	53.17 \pm 0.70	22.68 \pm 0.65	5.14 \pm 0.12	4.07 \pm 0.12	192.15 \pm 13.00	5.54 \pm 0.59	0.05296 \pm 0.01076
182	13:29:53.00 +47:11:18.1	5.41 \pm 0.57	7.44 \pm 0.14	28.68 \pm 0.14	21.11 \pm 0.14	3.52 \pm 0.04	4.40 \pm 0.06	131.89 \pm 13.00	4.74 \pm 0.59	0.02381 \pm 0.00854
183	13:29:53.72 +47:11:18.0	7.79 \pm 0.50	6.46 \pm 0.51	34.07 \pm 0.55	18.09 \pm 0.53	4.46 \pm 0.29	4.11 \pm 0.36	102.26 \pm 13.00	3.65 \pm 0.59	0.01613 \pm 0.00478
184	13:29:54.44 +47:11:17.8	6.37 \pm 0.48	7.09 \pm 0.61	28.00 \pm 0.59	17.28 \pm 0.58	4.58 \pm 0.28	3.20 \pm 0.32	123.73 \pm 13.00	4.20 \pm 0.59	0.01163 \pm 0.00415
185	13:29:55.16 +47:11:17.6	4.15 \pm 0.03	3.60 \pm 0.52	17.27 \pm 0.54	12.18 \pm 0.54	2.73 \pm 0.04	1.97 \pm 0.04	0.00 \pm 13.00	3.96 \pm 0.59	0.00155 \pm 0.00089
186	13:29:55.89 +47:11:17.5	6.81 \pm 0.44	5.53 \pm 0.52	26.40 \pm 0.54	13.58 \pm 0.51	3.53 \pm 0.47	2.51 \pm 0.46	22.37 \pm 13.00	2.98 \pm 0.59	0.00527 \pm 0.00237
187	13:29:56.61 +47:11:17.3	7.72 \pm 0.41	5.69 \pm 0.25	42.28 \pm 0.31	16.19 \pm 0.26	5.58 \pm 0.23	3.72 \pm 0.23	36.71 \pm 13.00	5.60 \pm 0.59	0.04380 \pm 0.01050
188	13:29:57.33 +47:11:17.1	7.42 \pm 0.25	5.35 \pm 0.48	31.10 \pm 0.54	14.02 \pm 0.49	4.68 \pm 0.10	3.17 \pm 0.10	56.89 \pm 13.00	5.18 \pm 0.59	0.01165 \pm 0.00287
189	13:29:47.57 +47:11:13.0	1.69 \pm 0.02	2.25 \pm 0.03	7.50 \pm 0.03	5.74 \pm 0.03	1.46 \pm 0.37	1.37 \pm 0.40	29.01 \pm 13.00	3.51 \pm 0.59	0.00000 \pm 0.00018
190	13:29:48.29 +47:11:12.8	4.30 \pm 0.08	3.32 \pm 0.43	17.02 \pm 0.45	8.77 \pm 0.42	2.92 \pm 0.22	1.93 \pm 0.20	64.46 \pm 13.00	3.65 \pm 0.59	0.00011 \pm 0.00074
191	13:29:49.01 +47:11:12.6	2.72 \pm 0.40	2.68 \pm 0.47	10.90 \pm 0.46	7.17 \pm 0.45	2.11 \pm 0.09	1.63 \pm 0.09	11.86 \pm 13.00	3.28 \pm 0.59	0.00000 \pm 0.00216
192	13:29:49.74 +47:11:12.5	2.76 \pm 0.40	4.02 \pm 0.04	17.57 \pm 0.04	9.93 \pm 0.04	2.81 \pm 0.44	2.16 \pm 0.48	18.64 \pm 13.00	4.97 \pm 0.59	0.02077 \pm 0.00992
193	13:29:50.46 +47:11:12.3	16.93 \pm 0.47	10.78 \pm 0.50	99.58 \pm 0.73	30.99 \pm 0.56	9.72 \pm 0.49	7.50 \pm 0.49	472.23 \pm 13.00	7.73 \pm 0.59	0.13935 \pm 0.02913
194	13:29:51.18 +47:11:12.2	3.23 \pm 0.01	4.90 \pm 0.53	17.95 \pm 0.53	12.27 \pm 0.53	3.02 \pm 0.03	2.59 \pm 0.04	357.00 \pm 13.00	5.48 \pm 0.59	0.01315 \pm 0.00304
195	13:29:51.90 +47:11:12.0	5.03 \pm 0.03	4.71 \pm 0.11	21.64 \pm 0.12	12.92 \pm 0.12	3.22 \pm 0.04	1.94 \pm 0.03	74.45 \pm 13.00	3.83 \pm 0.59	0.00575 \pm 0.00118
196	13:29:52.62 +47:11:11.8	5.81 \pm 0.46	6.04 \pm 0.56	27.55 \pm 0.58	16.59 \pm 0.58	4.58 \pm 0.11	3.28 \pm 0.11	116.36 \pm 13.00	6.16 \pm 0.59	0.01519 \pm 0.00519
197	13:29:53.35 +47:11:11.7	6.52 \pm 0.45	6.16 \pm 0.52	33.17 \pm 0.58	16.89 \pm 0.55	4.36 \pm 0.11	3.85 \pm 0.11	97.39 \pm 13.00	2.44 \pm 0.59	0.02575 \pm 0.00723
198	13:29:54.07 +47:11:11.5	4.91 \pm 0.03	5.34 \pm 0.04	20.38 \pm 0.04	13.71 \pm 0.04	3.85 \pm 0.49	2.46 \pm 0.51	34.67 \pm 13.00	1.93 \pm 0.59	0.00361 \pm 0.00075
199	13:29:54.79 +47:11:11.4	6.94 \pm 0.45	4.93 \pm 0.51	27.49 \pm 0.55	12.57 \pm 0.51	4.31 \pm 0.03	3.20 \pm 0.04	18.83 \pm 13.00	3.10 \pm 0.59	0.00675 \pm 0.00270
200	13:29:55.51 +47:11:11.2	3.71 \pm 0.43	3.69 \pm 0.49	14.82 \pm 0.44	8.74 \pm 0.43	2.09 \pm 0.42	2.42 \pm 0.58	0.00 \pm 13.00	3.71 \pm 0.59	0.00000 \pm 0.00227
201	13:29:56.23 +47:11:11.0	3.49 \pm 0.41	3.49 \pm 0.27	13.62 \pm 0.25	10.05 \pm 0.26	3.87 \pm 0.48	2.61 \pm 0.53	39.38 \pm 13.00	3.12 \pm 0.59	0.00000 \pm 0.00195
202	13:29:56.95 +47:11:10.9	4.28 \pm 0.39	4.38 \pm 0.45	18.54 \pm 0.47	12.48 \pm 0.47	3.74 \pm 0.03	2.41 \pm 0.03	98.38 \pm 13.00	6.97 \pm 0.59	0.00365 \pm 0.00277
203	13:29:57.68 +47:11:10.7	3.00 \pm 0.34	4.04 \pm 0.43	14.43 \pm 0.44	10.44 \pm 0.45	3.38 \pm 0.03	2.96 \pm 0.03	56.65 \pm 13.00	7.05 \pm 0.59	0.00335 \pm 0.00335
204	13:29:47.92 +47:11:06.5	2.13 \pm 0.18	2.88 \pm 0.41	9.43 \pm 0.36	6.76 \pm 0.36	1.96 \pm 0.08	1.72 \pm 0.09	32.92 \pm 13.00	5.35 \pm 0.59	0.00000 \pm 0.00142
205	13:29:48.64 +47:11:06.4	1.94 \pm 0.35	1.85 \pm 0.03	7.89 \pm 0.03	6.62 \pm 0.03	2.44 \pm 0.08	1.43 \pm 0.08	19.13 \pm 13.00	4.79 \pm 0.59	0.00000 \pm 0.00191
206	13:29:49.36 +47:11:06.2	2.28 \pm 0.03	2.56 \pm 0.24	11.09 \pm 0.24	6.59 \pm 0.22	2.56 \pm 0.23	1.53 \pm 0.25	30.78 \pm 13.00	5.16 \pm 0.59	0.00032 \pm 0.00057
207	13:29:50.08 +47:11:06.0	4.27 \pm 0.08	3.08 \pm 0.44	17.83 \pm 0.48	9.48 \pm 0.46	3.44 \pm 0.45	2.10 \pm 0.47	42.76 \pm 13.00	5.52 \pm 0.59	0.00199 \pm 0.00096
208	13:29:50.81 +47:11:05.9	4.58 \pm 0.21	4.61 \pm 0.44	25.40 \pm 0.50	14.40 \pm 0.47	4.72 \pm 0.24	3.39 \pm 0.24	515.89 \pm 13.00	5.17 \pm 0.59	0.02305 \pm 0.00567
209	13:29:51.53 +47:11:05.7	3.05 \pm 0.38	3.66 \pm 0.03	19.04 \pm 0.03	9.60 \pm 0.03	2.60 \pm 0.03	1.72 \pm 0.03	373.50 \pm 13.00	5.14 \pm 0.59	0.02214 \pm 0.00917
210	13:29:52.25 +47:11:05.6	5.90 \pm 0.09	5.25 \pm 0.52	29.48 \pm 0.55	13.15 \pm 0.51	4.11 \pm 0.25	3.17 \pm 0.26	126.22 \pm 13.00	5.06 \pm 0.59	0.02040 \pm 0.00438
211	13:29:52.97 +47:11:05.4	3.30 \pm 0.23	3.67 \pm 0.01	14.87 \pm 0.01	11.41 \pm 0.01	2.08 \pm 0.47	1.54 \pm 0.46	113.92 \pm 13.00	5.35 \pm 0.59	0.00183 \pm 0.00174
212	13:29:53.69 +47:11:05.2	2.81 \pm 0.03	3.07 \pm 0.09	11.92 \pm 0.11	9.91 \pm 0.11	2.81 \pm 0.03	1.67 \pm 0.03	40.77 \pm 13.00	2.02 \pm 0.59	0.00000 \pm 0.00024
213	13:29:54.41 +47:11:05.1	8.07 \pm 0.44	4.34 \pm 0.50	27.70 \pm 0.54	12.58 \pm 0.50	4.15 \pm 0.44	2.29 \pm 0.40	0.00 \pm 13.00	4.72 \pm 0.59	0.00214 \pm 0.00153
214	13:29:55.14 +47:11:04.9	7.25 \pm 0.24	6.04 \pm 0.12	28.12 \pm 0.12	11.35 \pm 0.11	3.49 \pm 0.03	2.18 \pm 0.03	37.35 \pm 13.00	5.24 \pm 0.59	0.00634 \pm 0.00169
215	13:29:55.86 +47:11:04.7	4.65 \pm 0.39	4.00 \pm 0.49	18.55 \pm 0.51	10.78 \pm 0.50	3.06 \pm 0.10	2.08 \pm 0.10	43.72 \pm 13.00	2.94 \pm 0.59	0.00129 \pm 0.00212
216	13:29:56.58 +47:11:04.6	5.33 \pm 0.39	5.17 \pm 0.04	25.04 \pm 0.04	13.24 \pm 0.03	3.93 \pm 0.10	3.53 \pm 0.10	24.72 \pm 13.00	4.41 \pm 0.59	0.01242 \pm 0.00417
217	13:29:57.30 +47:11:04.4	10.69 \pm 0.40	6.79 \pm 0.45	40.55 \pm 0.51	17.56 \pm 0.45	5.51 \pm 0.36	4.41 \pm 0.38	94.11 \pm 13.00	8.30 \pm 0.59	0.01271 \pm 0.00312
218	13:29:47.54 +47:11:00.2	1.73 \pm 0.34	1.04 \pm 0.37	5.73 \pm 0.39	4.96 \pm 0.41	1.09 \pm 0.01	0.39 \pm 0.01	42.75 \pm 13.00	3.82 \pm 0.59	0.00000 \pm 0.00102
219	13:29:48.27 +47:11:00.1	1.85 \pm 0.27	2.06 \pm 0.03	7.43 \pm 0.03	5.39 \pm 0.03	2.11 \pm 0.37	1.43 \pm 0.38	31.04 \pm 13.00	3.59 \pm 0.59	0.00000 \pm 0.00138
220	13:29:48.99 +47:10:59.9	2.17 \pm 0.03	2.72 \pm 0.43	7.76 \pm 0.41	5.85 \pm 0.42	2.37 \pm 0.03	1.89 \pm 0.03	47.03 \pm 13.00	3.63 \pm 0.59	

TABLE 1 — *Continued*

ID	Equatorial Coordinates	H β	[NII] λ 6548	H α	[NII] λ 6584	[SII] λ 6717	[SII] λ 6731	Σ_{H_2}	Σ_{HI}	Σ_{SFR}
225	13:29:52.60 +47:10:59.1	2.87 \pm 0.31	2.99 \pm 0.01	15.00 \pm 0.01	8.81 \pm 0.01	1.70 \pm 0.45	2.17 \pm 0.52	246.77 \pm 13.00	5.75 \pm 0.59	0.00680 \pm 0.00390
226	13:29:53.32 +47:10:58.9	1.75 \pm 0.01	2.64 \pm 0.25	8.86 \pm 0.24	7.94 \pm 0.26	1.70 \pm 0.45	1.64 \pm 0.44	63.03 \pm 13.00	3.35 \pm 0.59	0.00000 \pm 0.00057
227	13:29:54.04 +47:10:58.8	3.20 \pm 0.25	2.03 \pm 0.03	11.79 \pm 0.04	7.85 \pm 0.04	2.12 \pm 0.49	1.61 \pm 0.54	0.00 \pm 13.00	2.85 \pm 0.59	0.00000 \pm 0.00096
228	13:29:54.76 +47:10:58.6	2.62 \pm 0.38	3.95 \pm 0.49	13.66 \pm 0.48	9.85 \pm 0.49	3.31 \pm 0.47	2.32 \pm 0.48	21.42 \pm 13.00	4.12 \pm 0.59	0.00520 \pm 0.00483
229	13:29:55.48 +47:10:58.5	3.55 \pm 0.41	3.88 \pm 0.50	15.29 \pm 0.48	10.16 \pm 0.49	2.55 \pm 0.45	2.47 \pm 0.49	27.25 \pm 13.00	4.88 \pm 0.59	0.00101 \pm 0.00278
230	13:29:56.21 +47:10:58.3	5.83 \pm 0.09	5.29 \pm 0.48	29.49 \pm 0.52	13.32 \pm 0.49	5.35 \pm 0.46	2.98 \pm 0.45	99.16 \pm 13.00	6.58 \pm 0.59	0.02129 \pm 0.00453
231	13:29:56.93 +47:10:58.1	8.69 \pm 0.22	6.69 \pm 0.10	47.95 \pm 0.12	19.40 \pm 0.11	7.76 \pm 0.03	5.17 \pm 0.03	157.32 \pm 13.00	14.02 \pm 0.59	0.05210 \pm 0.01088
232	13:29:57.65 +47:10:58.0	14.15 \pm 0.48	8.04 \pm 0.52	55.94 \pm 0.61	19.28 \pm 0.52	8.50 \pm 0.49	7.13 \pm 0.51	266.52 \pm 13.00	11.67 \pm 0.59	0.02462 \pm 0.00551
233	13:29:47.89 +47:10:53.8	3.80 \pm 0.33	2.31 \pm 0.32	15.26 \pm 0.35	5.69 \pm 0.33	2.80 \pm 0.08	1.00 \pm 0.07	44.98 \pm 13.00	4.63 \pm 0.59	0.00000 \pm 0.00176
234	13:29:48.61 +47:10:53.6	5.98 \pm 0.20	3.01 \pm 0.36	23.64 \pm 0.39	9.51 \pm 0.36	3.00 \pm 0.20	2.36 \pm 0.20	40.23 \pm 13.00	4.20 \pm 0.59	0.00426 \pm 0.00140
235	13:29:49.33 +47:10:53.5	3.17 \pm 0.03	3.22 \pm 0.20	14.77 \pm 0.24	9.13 \pm 0.23	4.12 \pm 0.44	2.73 \pm 0.40	51.19 \pm 13.00	4.19 \pm 0.59	0.00274 \pm 0.00075
236	13:29:50.06 +47:10:53.3	19.79 \pm 0.49	9.43 \pm 0.49	80.35 \pm 0.65	25.19 \pm 0.51	9.25 \pm 0.26	7.14 \pm 0.26	55.21 \pm 13.00	5.92 \pm 0.59	0.04303 \pm 0.00903
237	13:29:50.78 +47:10:53.1	15.87 \pm 0.25	7.02 \pm 0.48	57.46 \pm 0.60	18.53 \pm 0.51	5.92 \pm 0.01	3.78 \pm 0.01	43.20 \pm 13.00	6.01 \pm 0.59	0.01923 \pm 0.00401
238	13:29:51.50 +47:10:53.0	3.74 \pm 0.35	4.64 \pm 0.47	23.08 \pm 0.48	10.30 \pm 0.44	2.84 \pm 0.41	2.58 \pm 0.48	281.26 \pm 13.00	9.51 \pm 0.59	0.02811 \pm 0.00928
239	13:29:52.22 +47:10:52.8	6.38 \pm 0.38	6.11 \pm 0.09	37.30 \pm 0.11	17.03 \pm 0.10	5.60 \pm 0.03	3.75 \pm 0.03	502.45 \pm 13.00	6.00 \pm 0.59	0.04479 \pm 0.01103
240	13:29:52.94 +47:10:52.7	4.56 \pm 0.35	4.29 \pm 0.42	26.16 \pm 0.49	12.35 \pm 0.45	4.66 \pm 0.23	3.14 \pm 0.23	296.67 \pm 13.00	6.68 \pm 0.59	0.02666 \pm 0.00793
241	13:29:53.67 +47:10:52.5	6.85 \pm 0.22	5.19 \pm 0.46	34.89 \pm 0.53	14.48 \pm 0.49	4.74 \pm 0.09	3.57 \pm 0.09	148.85 \pm 13.00	6.58 \pm 0.59	0.02763 \pm 0.00616
242	13:29:54.39 +47:10:52.3	4.48 \pm 0.03	4.51 \pm 0.09	28.35 \pm 0.11	13.52 \pm 0.10	4.58 \pm 0.43	3.87 \pm 0.43	238.76 \pm 13.00	6.79 \pm 0.59	0.03939 \pm 0.00791
243	13:29:55.11 +47:10:52.2	11.88 \pm 0.22	13.07 \pm 0.41	88.10 \pm 0.58	38.04 \pm 0.47	10.09 \pm 0.10	7.61 \pm 0.09	259.43 \pm 13.00	7.32 \pm 0.59	0.20999 \pm 0.04287
244	13:29:55.83 +47:10:52.0	10.87 \pm 0.36	11.86 \pm 0.42	67.86 \pm 0.55	30.93 \pm 0.47	9.97 \pm 0.10	7.81 \pm 0.10	283.06 \pm 13.00	9.58 \pm 0.59	0.10580 \pm 0.02258
245	13:29:56.55 +47:10:51.8	42.03 \pm 0.57	26.05 \pm 0.04	237.37 \pm 0.07	69.03 \pm 0.05	23.09 \pm 0.12	18.45 \pm 0.11	317.74 \pm 13.00	13.35 \pm 0.59	0.31654 \pm 0.06390
246	13:29:47.72 +47:12:33.6	10.94 \pm 0.44	5.78 \pm 0.47	49.70 \pm 0.62	16.08 \pm 0.50	5.90 \pm 0.09	4.05 \pm 0.08	0.00 \pm 13.00	10.02 \pm 0.59	0.03187 \pm 0.00731
247	13:29:48.44 +47:12:33.4	5.60 \pm 0.45	4.64 \pm 0.48	29.50 \pm 0.54	12.60 \pm 0.48	4.33 \pm 0.44	2.84 \pm 0.43	87.16 \pm 13.00	10.98 \pm 0.59	0.02422 \pm 0.00747
248	13:29:49.17 +47:12:33.2	4.29 \pm 0.45	5.85 \pm 0.26	28.44 \pm 0.30	15.93 \pm 0.28	5.85 \pm 0.10	3.53 \pm 0.09	255.17 \pm 13.00	8.80 \pm 0.59	0.04505 \pm 0.01465
249	13:29:49.89 +47:12:33.1	4.39 \pm 0.49	4.60 \pm 0.26	24.72 \pm 0.30	14.18 \pm 0.29	4.31 \pm 0.03	2.88 \pm 0.03	237.27 \pm 13.00	8.42 \pm 0.59	0.02317 \pm 0.00871
250	13:29:50.61 +47:12:32.9	3.40 \pm 0.26	4.46 \pm 0.53	18.19 \pm 0.55	11.57 \pm 0.54	3.78 \pm 0.27	2.58 \pm 0.26	114.88 \pm 13.00	8.90 \pm 0.59	0.01168 \pm 0.00435
251	13:29:51.33 +47:12:32.8	2.84 \pm 0.48	4.58 \pm 0.30	15.66 \pm 0.29	12.14 \pm 0.29	2.91 \pm 0.10	1.76 \pm 0.09	95.40 \pm 13.00	6.01 \pm 0.59	0.00981 \pm 0.00713
252	13:29:52.05 +47:12:32.6	6.93 \pm 0.50	5.92 \pm 0.54	33.15 \pm 0.61	16.50 \pm 0.55	5.09 \pm 0.10	3.63 \pm 0.10	157.05 \pm 13.00	6.09 \pm 0.59	0.02106 \pm 0.00630
253	13:29:52.78 +47:12:32.4	7.44 \pm 0.50	5.87 \pm 0.28	42.80 \pm 0.33	16.75 \pm 0.29	4.91 \pm 0.10	3.66 \pm 0.10	183.79 \pm 13.00	8.66 \pm 0.59	0.05085 \pm 0.01305
254	13:29:53.50 +47:12:32.3	5.61 \pm 0.49	4.89 \pm 0.11	30.30 \pm 0.12	14.43 \pm 0.11	5.04 \pm 0.50	3.50 \pm 0.48	136.92 \pm 13.00	6.14 \pm 0.59	0.02721 \pm 0.00849
255	13:29:54.22 +47:12:32.1	7.04 \pm 0.47	5.17 \pm 0.26	36.06 \pm 0.31	15.39 \pm 0.28	5.24 \pm 0.10	3.84 \pm 0.09	216.76 \pm 13.00	6.47 \pm 0.59	0.02948 \pm 0.00796
256	13:29:54.94 +47:12:31.9	15.31 \pm 0.57	9.35 \pm 0.28	91.72 \pm 0.42	28.32 \pm 0.31	10.93 \pm 0.52	7.38 \pm 0.50	164.15 \pm 13.00	10.19 \pm 0.59	0.13331 \pm 0.02867
257	13:29:55.66 +47:12:31.8	29.03 \pm 0.70	11.65 \pm 0.56	164.38 \pm 0.99	32.63 \pm 0.64	10.66 \pm 0.54	7.80 \pm 0.53	30.10 \pm 13.00	4.97 \pm 0.59	0.21718 \pm 0.04483
258	13:29:56.39 +47:12:31.6	14.16 \pm 0.52	5.97 \pm 0.25	83.85 \pm 0.38	17.42 \pm 0.26	5.23 \pm 0.09	3.67 \pm 0.09	36.51 \pm 13.00	4.00 \pm 0.59	0.11749 \pm 0.02527
259	13:29:57.11 +47:12:31.5	3.69 \pm 0.39	3.29 \pm 0.22	19.32 \pm 0.24	9.32 \pm 0.22	3.11 \pm 0.22	1.97 \pm 0.18	57.86 \pm 13.00	3.95 \pm 0.59	0.01193 \pm 0.00533
260	13:29:47.35 +47:12:27.3	7.29 \pm 0.43	6.89 \pm 0.40	54.62 \pm 0.55	19.40 \pm 0.44	6.27 \pm 0.09	4.18 \pm 0.09	173.98 \pm 13.00	11.66 \pm 0.59	0.12956 \pm 0.03076
261	13:29:48.07 +47:12:27.1	4.42 \pm 0.45	3.99 \pm 0.49	25.95 \pm 0.55	10.70 \pm 0.49	4.14 \pm 0.46	3.09 \pm 0.47	116.83 \pm 13.00	11.15 \pm 0.59	0.02826 \pm 0.00976
262	13:29:48.79 +47:12:27.0	6.15 \pm 0.50	4.94 \pm 0.52	33.10 \pm 0.60	13.57 \pm 0.54	3.57 \pm 0.25	2.69 \pm 0.25	197.79 \pm 13.00	10.23 \pm 0.59	0.03038 \pm 0.00910
263	13:29:49.51 +47:12:26.8	3.41 \pm 0.50	3.82 \pm 0.28	18.98 \pm 0.29	11.93 \pm 0.29	3.86 \pm 0.42	2.75 \pm 0.45	101.06 \pm 13.00	6.25 \pm 0.59	0.01465 \pm 0.00793
264	13:29:50.23 +47:12:26.6	4.10 \pm 0.52	5.35 \pm 0.04	20.25 \pm 0.04	14.48 \pm 0.04	4.13 \pm 0.51	3.10 \pm 0.53	28.39 \pm 13.00	4.51 \pm 0.59	0.01015 \pm 0.00559
265	13:29:50.96 +47:12:26.5	2.48 \pm 0.49	4.68 \pm 0.30	14.81 \pm 0.30	13.25 \pm 0.31	3.11 \pm 0.50	2.53 \pm 0.53	54.66 \pm 13.00	6.16 \pm 0.59	0.01237 \pm 0.00930
266	13:29:51.68 +47:12:26.3	4.09 \pm 0.50	5.40 \pm 0.55	23.72 \pm 0.58	15.19 \pm 0.58	3.68 \pm 0.50	3.20 \pm 0.52	110.42 \pm 13.00	7.12 \pm 0.59	0.02406 \pm 0.00981
267	13:29:52.40 +47:12:26.2	6.62 \pm 0.51	5.72 \pm 0.56	37.35 \pm 0.64	17.09 \pm 0.58	5.34 \pm 0.29	3.42 \pm 0.27	186.25 \pm 13.00	6.02 \pm 0.59	0.04068 \pm 0.01142
268	13:29:53.12 +47:12:26.0	8.62 \pm 0.55	5.63 \pm 0.13	43.28 \pm 0.14	15.75 \pm 0.12	5.93 \pm 0.12	3.79 \pm 0.11	112.01 \pm 13.00	4.60 \pm 0.59	0.03547 \pm 0.00913
269	13:29:53.85 +47:12:25.8	8.04 \pm 0.12	6.21 \pm 0.34	44.43 \pm 0.36	15.19 \pm 0.32	4.71 \pm 0.55	3.25 \pm 0.58	76.47 \pm 13.00	5.60 \pm 0.59	0.04781 \pm 0.00977
270	13:29:54.57 +47:12:25.7	9.72 \pm 0.52	7.31 \pm 0.46	58.32 \pm 0.61	21.49 \pm 0.50	7.31 \pm 0.51	5.12 \pm 0.50	262.93 \pm 13.00	8.63 \pm 0.59	0.08112 \pm 0.01898
271	13:29:55.29 +47:12:25.5	13.35 \pm 0.54	8.37 \pm 0.45	78.41 \pm 0.66	23.60 \pm 0.50	8.81 \pm 0.27	5.94 \pm 0.26	147.66 \pm 13.00	8.55 \pm 0.59	0.10715 \pm 0.02347
272	13:29:56.01 +47:12:25.3	20.79 \pm 0.61	8.40 \pm 0.53	100.69 \pm 0.82	23.21 \pm 0.57	7.97 \pm 0.26	6.04 \pm 0.26	44.99 \pm 13.00	7.22 \pm 0.59	0.08841 \pm 0.01867
273	13:29:56.73 +47:12:25.2	11.09 \pm 0.27	5.78 \pm 0.40	63.83 \pm 0.59	16.68 \pm 0.44	6.98 \pm 0.25	3.95 \pm 0.23	89.71 \pm 13.00	6.03 \pm 0.59	0.08116 \pm 0.01693
274	13:29:57.46 +47:12:25.0	2.23 \pm 0.39	3.29 \pm 0.27	12.68 \pm 0.25	8.17 \pm 0.25	2.32 \pm 0.09	1.44 \pm 0.09	42.63 \pm 13.00	4.27 \pm 0.59	0.00707 \pm 0.00627
275	13:29:47.69 +47:12:20.8	2.89 \pm 0.43	3.50 \pm 0.51	17.12 \pm 0.50	9.21 \pm 0.49	3.02 \pm 0.09	1.93 \pm 0.09	188.39 \pm 13.00	9.65 \pm 0.59	0.01549 \pm 0.00832
276	13:29:48.42 +47:12:20.7	2.59 \pm 0.41	3.57 \pm 0.58	13.08 \pm 0.51	7.62 \pm 0.51	3.26 \pm 0.03	1.77 \pm 0.03	152.78 \pm 13.00	7.82 \pm 0.59	0.00341 \pm 0.00455
277	13:29:49.14 +47:12:20.5	3.10 \pm 0.26	4.30 \pm 0.57	17.88 \pm 0.57	10.69 \pm 0.56					

TABLE 1 — *Continued*

ID	Equatorial Coordinates	H β	[NII] λ 6548	H α	[NII] λ 6584	[SII] λ 6717	[SII] λ 6731	Σ_{H_2}	Σ_{HI}	Σ_{SFR}
282	13:29:52.75 +47:12:19.7	10.25 \pm 0.60	6.95 \pm 0.61	55.42 \pm 0.75	19.61 \pm 0.63	5.32 \pm 0.01	3.65 \pm 0.01	67.48 \pm 13.00	3.93 \pm 0.59	0.05878 \pm 0.01434
283	13:29:53.47 +47:12:19.5	16.08 \pm 0.13	8.83 \pm 0.62	82.82 \pm 0.83	23.03 \pm 0.63	7.29 \pm 0.12	5.21 \pm 0.12	149.21 \pm 13.00	6.92 \pm 0.59	0.08255 \pm 0.01670
284	13:29:54.19 +47:12:19.4	32.61 \pm 0.75	15.05 \pm 0.63	175.16 \pm 1.07	41.71 \pm 0.71	12.58 \pm 0.12	8.50 \pm 0.12	87.35 \pm 13.00	6.28 \pm 0.59	0.20566 \pm 0.04236
285	13:29:54.91 +47:12:19.2	11.32 \pm 0.54	6.72 \pm 0.12	62.09 \pm 0.15	21.05 \pm 0.13	7.06 \pm 0.27	5.10 \pm 0.27	283.38 \pm 13.00	9.24 \pm 0.59	0.06964 \pm 0.01585
286	13:29:55.64 +47:12:19.1	7.15 \pm 0.03	5.78 \pm 0.26	44.97 \pm 0.34	17.89 \pm 0.29	6.65 \pm 0.50	4.77 \pm 0.50	104.84 \pm 13.00	7.43 \pm 0.59	0.06782 \pm 0.01365
287	13:29:56.36 +47:12:18.9	10.83 \pm 0.52	7.41 \pm 0.52	67.17 \pm 0.73	21.20 \pm 0.56	6.39 \pm 0.10	4.95 \pm 0.11	45.49 \pm 13.00	5.84 \pm 0.59	0.10310 \pm 0.02342
288	13:29:57.08 +47:12:18.7	5.72 \pm 0.42	5.28 \pm 0.10	28.94 \pm 0.10	13.32 \pm 0.10	4.17 \pm 0.22	2.80 \pm 0.23	16.52 \pm 13.00	3.36 \pm 0.59	0.02074 \pm 0.00611
289	13:29:47.32 +47:12:14.6	5.12 \pm 0.49	4.09 \pm 0.43	26.39 \pm 0.49	11.47 \pm 0.45	3.88 \pm 0.10	2.97 \pm 0.10	132.31 \pm 13.00	8.96 \pm 0.59	0.01908 \pm 0.00684
290	13:29:48.04 +47:12:14.4	2.04 \pm 0.44	3.25 \pm 0.29	11.26 \pm 0.27	8.50 \pm 0.27	2.35 \pm 0.09	1.61 \pm 0.10	72.72 \pm 13.00	4.71 \pm 0.59	0.00414 \pm 0.00639
291	13:29:48.76 +47:12:14.2	3.03 \pm 0.50	3.90 \pm 0.51	13.79 \pm 0.52	11.71 \pm 0.54	4.48 \pm 0.11	2.84 \pm 0.10	10.28 \pm 13.00	3.91 \pm 0.59	0.00120 \pm 0.00396
292	13:29:49.49 +47:12:14.1	4.29 \pm 0.11	5.36 \pm 0.31	22.00 \pm 0.31	13.27 \pm 0.30	3.97 \pm 0.52	2.70 \pm 0.51	8.88 \pm 13.00	3.43 \pm 0.59	0.01386 \pm 0.00310
293	13:29:50.21 +47:12:13.9	6.97 \pm 0.53	7.82 \pm 0.59	37.61 \pm 0.64	21.49 \pm 0.61	6.27 \pm 0.11	4.20 \pm 0.12	1.25 \pm 13.00	3.38 \pm 0.59	0.03621 \pm 0.01021
294	13:29:50.93 +47:12:13.7	8.95 \pm 0.55	8.88 \pm 0.60	53.36 \pm 0.73	24.34 \pm 0.64	7.69 \pm 0.59	5.53 \pm 0.58	29.08 \pm 13.00	4.40 \pm 0.59	0.07230 \pm 0.01779
295	13:29:51.65 +47:12:13.6	31.04 \pm 0.74	15.10 \pm 0.68	167.23 \pm 1.06	42.13 \pm 0.76	12.35 \pm 0.13	9.04 \pm 0.13	58.81 \pm 13.00	2.85 \pm 0.59	0.19726 \pm 0.04073
296	13:29:52.37 +47:12:13.4	33.04 \pm 0.76	15.16 \pm 0.36	172.07 \pm 0.57	44.79 \pm 0.41	12.99 \pm 0.59	9.36 \pm 0.58	92.58 \pm 13.00	3.36 \pm 0.59	0.18792 \pm 0.03865
297	13:29:53.10 +47:12:13.3	32.71 \pm 0.75	14.23 \pm 0.58	167.91 \pm 0.94	40.86 \pm 0.65	12.23 \pm 0.57	9.03 \pm 0.56	161.62 \pm 13.00	3.93 \pm 0.59	0.17709 \pm 0.03648
298	13:29:53.82 +47:12:13.1	35.83 \pm 0.76	12.48 \pm 0.66	170.42 \pm 1.07	36.76 \pm 0.73	10.41 \pm 0.13	8.32 \pm 0.13	109.45 \pm 13.00	5.39 \pm 0.59	0.15048 \pm 0.03092
299	13:29:54.54 +47:12:12.9	66.00 \pm 0.53	19.18 \pm 0.38	296.48 \pm 0.71	57.12 \pm 0.44	15.78 \pm 0.15	11.24 \pm 0.14	162.04 \pm 13.00	8.56 \pm 0.59	0.23660 \pm 0.04749
300	13:29:55.26 +47:12:12.8	12.88 \pm 0.53	8.54 \pm 0.55	80.69 \pm 0.79	23.57 \pm 0.59	8.45 \pm 0.53	6.64 \pm 0.53	432.62 \pm 13.00	4.96 \pm 0.59	0.12904 \pm 0.02832
301	13:29:55.98 +47:12:12.6	6.39 \pm 0.47	5.54 \pm 0.46	37.64 \pm 0.54	16.29 \pm 0.48	5.47 \pm 0.27	3.97 \pm 0.26	108.38 \pm 13.00	7.65 \pm 0.59	0.04619 \pm 0.01253
302	13:29:56.71 +47:12:12.4	7.68 \pm 0.49	5.22 \pm 0.51	44.95 \pm 0.64	14.81 \pm 0.54	4.72 \pm 0.50	3.65 \pm 0.51	19.51 \pm 13.00	4.74 \pm 0.59	0.05628 \pm 0.01415
303	13:29:57.43 +47:12:12.3	1.99 \pm 0.36	2.41 \pm 0.44	10.88 \pm 0.46	7.77 \pm 0.46	2.38 \pm 0.03	1.27 \pm 0.02	24.67 \pm 13.00	2.21 \pm 0.59	0.00329 \pm 0.00520
304	13:29:47.67 +47:12:08.1	4.73 \pm 0.43	4.32 \pm 0.52	20.09 \pm 0.54	11.01 \pm 0.52	3.73 \pm 0.47	2.66 \pm 0.50	45.08 \pm 13.00	5.32 \pm 0.59	0.00413 \pm 0.00288
305	13:29:48.39 +47:12:07.9	4.25 \pm 0.26	4.21 \pm 0.28	18.66 \pm 0.28	11.34 \pm 0.27	3.55 \pm 0.49	2.36 \pm 0.50	20.04 \pm 13.00	5.18 \pm 0.59	0.00419 \pm 0.00203
306	13:29:49.11 +47:12:07.8	4.94 \pm 0.50	6.25 \pm 0.29	30.58 \pm 0.32	17.29 \pm 0.31	5.30 \pm 0.28	3.96 \pm 0.28	42.23 \pm 13.00	3.80 \pm 0.59	0.04095 \pm 0.01311
307	13:29:49.83 +47:12:07.6	3.36 \pm 0.26	3.82 \pm 0.31	19.76 \pm 0.31	11.07 \pm 0.31	2.52 \pm 0.26	2.22 \pm 0.32	40.23 \pm 13.00	4.46 \pm 0.59	0.01916 \pm 0.00603
308	13:29:50.55 +47:12:07.5	9.41 \pm 0.59	7.17 \pm 0.33	50.94 \pm 0.39	23.62 \pm 0.36	6.51 \pm 0.60	4.70 \pm 0.65	0.00 \pm 13.00	3.38 \pm 0.59	0.05331 \pm 0.01328
309	13:29:51.28 +47:12:07.3	30.79 \pm 0.81	16.89 \pm 0.75	172.07 \pm 1.13	51.76 \pm 0.86	14.51 \pm 0.39	10.71 \pm 0.39	45.06 \pm 13.00	3.41 \pm 0.59	0.22108 \pm 0.04592
310	13:29:52.00 +47:12:07.1	72.99 \pm 1.04	36.84 \pm 0.77	426.43 \pm 1.40	108.86 \pm 0.94	34.23 \pm 0.90	23.94 \pm 0.87	264.15 \pm 13.00	4.54 \pm 0.59	0.62245 \pm 0.12583
311	13:29:52.72 +47:12:07.0	49.36 \pm 0.96	25.26 \pm 0.45	285.83 \pm 0.73	78.24 \pm 0.53	20.61 \pm 0.85	14.19 \pm 0.84	248.54 \pm 13.00	5.99 \pm 0.59	0.40562 \pm 0.08269
312	13:29:53.44 +47:12:06.8	15.77 \pm 0.68	10.46 \pm 0.39	87.97 \pm 0.48	30.01 \pm 0.41	8.02 \pm 0.61	6.68 \pm 0.65	231.51 \pm 13.00	7.63 \pm 0.59	0.10743 \pm 0.02371
313	13:29:54.16 +47:12:06.6	44.79 \pm 0.86	15.22 \pm 0.39	220.75 \pm 0.64	45.42 \pm 0.44	12.06 \pm 0.15	8.80 \pm 0.15	156.11 \pm 13.00	7.90 \pm 0.59	0.21495 \pm 0.04384
314	13:29:54.89 +47:12:06.5	47.26 \pm 0.84	16.72 \pm 0.37	277.57 \pm 0.68	47.43 \pm 0.42	15.67 \pm 0.14	11.63 \pm 0.14	119.31 \pm 13.00	7.76 \pm 0.59	0.40626 \pm 0.08258
315	13:29:55.61 +47:12:06.3	14.01 \pm 0.12	10.54 \pm 0.54	89.79 \pm 0.81	30.75 \pm 0.62	10.16 \pm 0.28	7.46 \pm 0.29	451.89 \pm 13.00	7.21 \pm 0.59	0.15269 \pm 0.03082
316	13:29:56.33 +47:12:06.2	6.75 \pm 0.11	5.62 \pm 0.29	39.42 \pm 0.31	16.68 \pm 0.31	5.84 \pm 0.29	4.25 \pm 0.28	43.17 \pm 13.00	7.03 \pm 0.59	0.04776 \pm 0.00980
317	13:29:57.05 +47:12:06.0	4.44 \pm 0.48	4.40 \pm 0.27	23.82 \pm 0.30	12.98 \pm 0.28	4.23 \pm 0.50	2.94 \pm 0.49	15.35 \pm 13.00	4.11 \pm 0.59	0.01865 \pm 0.00729
318	13:29:47.29 +47:12:01.8	2.48 \pm 0.41	3.05 \pm 0.47	10.90 \pm 0.49	9.38 \pm 0.50	2.69 \pm 0.10	2.25 \pm 0.10	25.17 \pm 13.00	4.00 \pm 0.59	0.00000 \pm 0.00289
319	13:29:48.01 +47:12:01.7	3.07 \pm 0.42	3.51 \pm 0.52	16.04 \pm 0.52	10.07 \pm 0.53	2.86 \pm 0.10	1.96 \pm 0.10	3.44 \pm 13.00	3.41 \pm 0.59	0.00794 \pm 0.00537
320	13:29:48.74 +47:12:01.5	7.56 \pm 0.50	6.32 \pm 0.28	45.68 \pm 0.35	19.80 \pm 0.31	5.65 \pm 0.51	3.62 \pm 0.50	12.68 \pm 13.00	6.15 \pm 0.59	0.06230 \pm 0.01567
321	13:29:49.46 +47:12:01.3	8.27 \pm 0.30	5.04 \pm 0.30	36.67 \pm 0.34	16.68 \pm 0.32	4.27 \pm 0.04	3.39 \pm 0.04	29.63 \pm 13.00	4.62 \pm 0.59	0.01905 \pm 0.00439
322	13:29:50.18 +47:12:01.2	12.85 \pm 0.60	9.90 \pm 0.34	80.03 \pm 0.43	28.85 \pm 0.37	9.51 \pm 0.63	6.50 \pm 0.61	82.76 \pm 13.00	3.87 \pm 0.59	0.12613 \pm 0.02818
323	13:29:50.90 +47:12:01.0	57.53 \pm 0.95	31.31 \pm 0.84	362.57 \pm 1.49	101.31 \pm 1.03	29.98 \pm 0.85	20.71 \pm 0.82	316.05 \pm 13.00	5.84 \pm 0.59	0.62502 \pm 0.12680
324	13:29:51.62 +47:12:00.9	49.36 \pm 0.86	31.67 \pm 0.83	301.50 \pm 1.26	95.73 \pm 0.97	25.54 \pm 0.50	19.39 \pm 0.50	625.62 \pm 13.00	6.06 \pm 0.59	0.48287 \pm 0.09814
325	13:29:52.35 +47:12:00.7	46.53 \pm 1.00	41.27 \pm 1.06	279.00 \pm 1.45	135.21 \pm 1.27	30.97 \pm 0.56	23.16 \pm 0.54	503.67 \pm 13.00	3.88 \pm 0.59	0.42796 \pm 0.08772
326	13:29:53.07 +47:12:00.5	30.04 \pm 0.91	21.10 \pm 0.97	160.55 \pm 1.22	67.76 \pm 1.10	15.19 \pm 0.52	9.88 \pm 0.51	165.90 \pm 13.00	4.82 \pm 0.59	0.18537 \pm 0.03900
327	13:29:53.79 +47:12:00.4	17.60 \pm 0.78	10.62 \pm 0.82	95.12 \pm 1.01	32.07 \pm 0.90	7.59 \pm 0.43	6.34 \pm 0.41	129.18 \pm 13.00	6.73 \pm 0.59	0.10834 \pm 0.02419
328	13:29:54.51 +47:12:00.2	59.31 \pm 0.92	21.37 \pm 0.76	337.09 \pm 1.39	65.22 \pm 0.89	19.40 \pm 0.16	14.87 \pm 0.16	142.33 \pm 13.00	6.49 \pm 0.59	0.46040 \pm 0.09328
329	13:29:55.23 +47:12:00.0	23.87 \pm 0.64	11.98 \pm 0.33	132.99 \pm 0.50	36.69 \pm 0.37	11.72 \pm 0.63	8.23 \pm 0.60	353.61 \pm 13.00	7.57 \pm 0.59	0.16733 \pm 0.03478
330	13:29:55.96 +47:11:59.9	41.18 \pm 0.74	15.85 \pm 0.60	223.94 \pm 1.13	49.62 \pm 0.72	16.70 \pm 0.13	12.13 \pm 0.12	343.95 \pm 13.00	8.29 \pm 0.59	0.27344 \pm 0.05567
331	13:29:56.68 +47:11:59.7	18.06 \pm 0.62	7.78 \pm 0.58	86.23 \pm 0.81	24.28 \pm 0.64	7.83 \pm 0.12	6.44 \pm 0.12	59.69 \pm 13.00	6.30 \pm 0.59	0.07161 \pm 0.01545
332	13:29:57.40 +47:11:59.5	4.25 \pm 0.45	4.06 \pm 0.25	22.12 \pm 0.28	12.21 \pm 0.27	3.41 \pm 0.46	2.99 \pm 0.50	21.41 \pm 13.00	3.96 \pm 0.59	0.01479 \pm 0.00610
333	13:29:47.64 +47:11:55.4	2.71 \pm 0.09	2.77 \pm 0.42	13.00 \pm 0.43	8.10 \pm 0.43	2.77 \pm 0.24	1.47 \pm 0.23	24.88 \pm 13.00	2.66 \pm 0.59	0.00189 \pm 0.00128
334	13:29:48.36 +47:11:55.2	2.54 \pm 0.46	2.69 \pm 0.48	11.79 $\pm</$						

TABLE 1 — *Continued*

ID	Equatorial Coordinates	H β	[NII] λ 6548	H α	[NII] λ 6584	[SII] λ 6717	[SII] λ 6731	Σ_{H_2}	Σ_{HI}	Σ_{SFR}
339	13:29:51.97 +47:11:54.4	32.98 \pm 1.12	50.17 \pm 1.19	176.35 \pm 1.25	159.09 \pm 1.36	28.23 \pm 0.28	22.02 \pm 0.28	377.28 \pm 13.00	4.98 \pm 0.59	0.20496 \pm 0.04356
340	13:29:52.69 +47:11:54.2	48.49 \pm 1.25	122.50 \pm 1.51	223.57 \pm 1.57	370.68 \pm 1.87	73.22 \pm 1.46	56.36 \pm 1.44	274.75 \pm 13.00	4.29 \pm 0.59	0.16700 \pm 0.03498
341	13:29:53.41 +47:11:54.1	41.96 \pm 0.93	34.31 \pm 1.13	207.28 \pm 1.37	108.41 \pm 1.29	22.04 \pm 0.24	17.68 \pm 0.25	163.30 \pm 13.00	5.29 \pm 0.59	0.20234 \pm 0.04163
342	13:29:54.14 +47:11:53.9	28.58 \pm 0.84	19.83 \pm 0.89	146.14 \pm 1.12	53.93 \pm 0.97	15.44 \pm 0.88	10.15 \pm 0.88	7.47 \pm 13.00	3.60 \pm 0.59	0.15130 \pm 0.03178
343	13:29:54.86 +47:11:53.8	18.64 \pm 0.64	12.58 \pm 0.60	103.20 \pm 0.79	38.82 \pm 0.68	12.29 \pm 0.15	8.89 \pm 0.15	145.29 \pm 13.00	4.49 \pm 0.59	0.12551 \pm 0.02684
344	13:29:55.58 +47:11:53.6	28.19 \pm 0.77	14.18 \pm 0.73	153.87 \pm 1.03	41.34 \pm 0.80	10.68 \pm 0.05	7.97 \pm 0.05	340.57 \pm 13.00	8.18 \pm 0.59	0.18615 \pm 0.03880
345	13:29:56.30 +47:11:53.4	33.87 \pm 0.39	15.55 \pm 0.55	173.72 \pm 0.89	45.11 \pm 0.63	15.13 \pm 0.13	11.12 \pm 0.13	149.39 \pm 13.00	5.76 \pm 0.59	0.18320 \pm 0.03696
346	13:29:57.02 +47:11:53.3	10.88 \pm 0.56	6.16 \pm 0.54	50.38 \pm 0.66	18.08 \pm 0.58	5.38 \pm 0.12	3.76 \pm 0.11	20.01 \pm 13.00	3.82 \pm 0.59	0.03431 \pm 0.00832
347	13:29:47.26 +47:11:49.1	2.85 \pm 0.42	3.09 \pm 0.45	11.36 \pm 0.46	8.92 \pm 0.47	3.27 \pm 0.46	2.00 \pm 0.47	17.73 \pm 13.00	3.23 \pm 0.59	0.00000 \pm 0.00220
348	13:29:47.99 +47:11:48.9	3.02 \pm 0.43	3.75 \pm 0.55	11.65 \pm 0.48	8.20 \pm 0.48	2.08 \pm 0.43	1.79 \pm 0.46	24.19 \pm 13.00	3.42 \pm 0.59	0.00000 \pm 0.00204
349	13:29:48.71 +47:11:48.8	4.20 \pm 0.42	3.60 \pm 0.52	17.70 \pm 0.54	11.04 \pm 0.54	3.43 \pm 0.27	2.35 \pm 0.24	10.41 \pm 13.00	6.21 \pm 0.59	0.00221 \pm 0.00271
350	13:29:49.43 +47:11:48.6	10.86 \pm 0.60	7.02 \pm 0.65	56.35 \pm 0.75	18.68 \pm 0.67	5.36 \pm 0.63	3.69 \pm 0.60	70.22 \pm 13.00	6.36 \pm 0.59	0.05384 \pm 0.01300
351	13:29:50.15 +47:11:48.4	28.07 \pm 0.16	19.00 \pm 0.73	162.95 \pm 1.05	57.61 \pm 0.85	16.58 \pm 0.05	11.87 \pm 0.05	360.90 \pm 13.00	8.76 \pm 0.59	0.22794 \pm 0.04579
352	13:29:50.87 +47:11:48.3	27.40 \pm 0.84	19.85 \pm 0.87	156.75 \pm 1.12	61.93 \pm 0.98	14.93 \pm 0.18	12.05 \pm 0.19	296.47 \pm 13.00	9.36 \pm 0.59	0.21168 \pm 0.04454
353	13:29:51.60 +47:11:48.1	42.58 \pm 1.12	28.40 \pm 1.06	225.65 \pm 1.28	87.55 \pm 1.18	14.41 \pm 0.24	14.07 \pm 0.25	241.53 \pm 13.00	4.27 \pm 0.59	0.25977 \pm 0.05390
354	13:29:52.32 +47:11:48.0	37.33 \pm 1.42	138.72 \pm 0.41	173.52 \pm 0.38	415.76 \pm 0.48	61.96 \pm 0.12	56.24 \pm 0.13	224.74 \pm 13.00	5.25 \pm 0.59	0.12995 \pm 0.02848
355	13:29:53.04 +47:11:47.8	55.96 \pm 1.55	168.53 \pm 0.42	229.88 \pm 0.40	524.63 \pm 0.51	80.07 \pm 1.84	69.68 \pm 1.90	188.11 \pm 13.00	3.48 \pm 0.59	0.13137 \pm 0.02765
356	13:29:53.76 +47:11:47.6	40.37 \pm 1.07	26.97 \pm 1.16	194.01 \pm 1.37	81.63 \pm 1.26	18.08 \pm 0.23	13.12 \pm 0.24	97.93 \pm 13.00	3.62 \pm 0.59	0.17701 \pm 0.03683
357	13:29:54.48 +47:11:47.5	36.33 \pm 0.82	19.82 \pm 0.81	198.38 \pm 1.16	62.10 \pm 0.93	18.11 \pm 0.18	12.42 \pm 0.17	179.44 \pm 13.00	4.21 \pm 0.59	0.24338 \pm 0.05006
358	13:29:55.21 +47:11:47.3	89.74 \pm 0.56	28.12 \pm 0.82	417.85 \pm 1.49	84.12 \pm 0.95	22.30 \pm 0.42	17.58 \pm 0.43	150.82 \pm 13.00	5.65 \pm 0.59	0.36640 \pm 0.07348
359	13:29:55.93 +47:11:47.1	58.72 \pm 0.82	50.58 \pm 0.78	387.70 \pm 1.38	154.31 \pm 1.02	33.34 \pm 0.39	31.02 \pm 0.40	449.98 \pm 13.00	8.23 \pm 0.59	0.74227 \pm 0.14998
360	13:29:56.65 +47:11:47.0	9.45 \pm 0.52	6.40 \pm 0.12	44.38 \pm 0.14	18.07 \pm 0.12	4.81 \pm 0.11	3.59 \pm 0.11	13.66 \pm 13.00	6.44 \pm 0.59	0.03018 \pm 0.00749
361	13:29:57.37 +47:11:46.8	3.72 \pm 0.41	3.65 \pm 0.43	19.08 \pm 0.45	11.80 \pm 0.43	3.51 \pm 0.44	2.62 \pm 0.45	41.83 \pm 13.00	4.16 \pm 0.59	0.01065 \pm 0.00517
362	13:29:47.61 +47:11:42.6	6.74 \pm 0.44	4.17 \pm 0.47	27.39 \pm 0.53	10.82 \pm 0.47	3.71 \pm 0.45	2.91 \pm 0.47	15.45 \pm 13.00	4.26 \pm 0.59	0.00772 \pm 0.00292
363	13:29:48.33 +47:11:42.5	5.13 \pm 0.44	3.98 \pm 0.49	21.57 \pm 0.52	11.16 \pm 0.49	3.26 \pm 0.03	2.01 \pm 0.03	8.67 \pm 13.00	3.83 \pm 0.59	0.00493 \pm 0.00291
364	13:29:49.06 +47:11:42.3	5.28 \pm 0.49	4.91 \pm 0.58	29.95 \pm 0.62	15.08 \pm 0.59	4.77 \pm 0.58	3.38 \pm 0.57	39.16 \pm 13.00	5.83 \pm 0.59	0.03103 \pm 0.00997
365	13:29:49.78 +47:11:42.2	26.50 \pm 0.70	14.46 \pm 0.36	148.82 \pm 0.52	42.61 \pm 0.40	13.50 \pm 0.14	9.15 \pm 0.14	246.76 \pm 13.00	7.80 \pm 0.59	0.19200 \pm 0.03983
366	13:29:50.50 +47:11:42.0	33.69 \pm 0.72	22.86 \pm 0.74	205.13 \pm 1.10	66.43 \pm 0.85	20.27 \pm 0.39	14.28 \pm 0.39	493.56 \pm 13.00	9.20 \pm 0.59	0.32277 \pm 0.06617
367	13:29:51.22 +47:11:41.8	39.43 \pm 0.81	19.47 \pm 0.93	196.75 \pm 1.21	58.81 \pm 1.00	15.01 \pm 0.47	10.88 \pm 0.47	155.69 \pm 13.00	5.19 \pm 0.59	0.19598 \pm 0.04017
368	13:29:51.94 +47:11:41.7	32.94 \pm 1.13	41.25 \pm 1.15	176.62 \pm 1.22	127.54 \pm 1.28	22.35 \pm 0.26	16.98 \pm 0.28	89.24 \pm 13.00	2.26 \pm 0.59	0.20656 \pm 0.04395
369	13:29:52.67 +47:11:41.5	87.16 \pm 1.78	471.86 \pm 2.88	500.68 \pm 3.47	1285.67 \pm 3.37	174.67 \pm 2.06	193.44 \pm 2.25	207.82 \pm 13.00	2.06 \pm 0.59	0.63109 \pm 0.12990
370	13:29:53.39 +47:11:41.3	25.32 \pm 1.12	48.56 \pm 1.41	120.76 \pm 1.37	155.17 \pm 1.59	24.67 \pm 1.39	23.80 \pm 1.46	123.87 \pm 13.00	3.99 \pm 0.59	0.09322 \pm 0.02132
371	13:29:54.11 +47:11:41.2	53.74 \pm 1.02	28.88 \pm 1.04	270.79 \pm 1.40	88.11 \pm 1.15	21.51 \pm 0.54	15.13 \pm 0.54	184.13 \pm 13.00	3.12 \pm 0.59	0.27995 \pm 0.05713
372	13:29:54.83 +47:11:41.0	28.17 \pm 0.76	16.09 \pm 0.78	155.53 \pm 1.04	47.83 \pm 0.85	13.15 \pm 0.76	10.39 \pm 0.79	196.34 \pm 13.00	6.78 \pm 0.59	0.19340 \pm 0.04027
373	13:29:55.55 +47:11:40.9	36.04 \pm 0.70	23.11 \pm 0.67	218.17 \pm 1.08	69.65 \pm 0.80	21.88 \pm 0.35	16.03 \pm 0.35	484.93 \pm 13.00	11.61 \pm 0.59	0.33958 \pm 0.06932
374	13:29:56.27 +47:11:40.7	8.34 \pm 0.56	6.23 \pm 0.12	41.21 \pm 0.14	18.20 \pm 0.13	4.86 \pm 0.57	4.13 \pm 0.58	33.12 \pm 13.00	7.71 \pm 0.59	0.03173 \pm 0.00844
375	13:29:57.00 +47:11:40.5	7.62 \pm 0.48	5.38 \pm 0.51	38.11 \pm 0.59	15.70 \pm 0.53	4.61 \pm 0.25	2.60 \pm 0.24	31.87 \pm 13.00	5.94 \pm 0.59	0.02952 \pm 0.00780
376	13:29:47.24 +47:11:36.4	3.54 \pm 0.41	2.25 \pm 0.43	17.44 \pm 0.46	7.88 \pm 0.43	2.20 \pm 0.08	1.21 \pm 0.05	26.05 \pm 13.00	4.44 \pm 0.59	0.00714 \pm 0.00440
377	13:29:47.96 +47:11:36.2	3.04 \pm 0.42	2.74 \pm 0.41	10.20 \pm 0.39	7.74 \pm 0.39	3.00 \pm 0.10	1.46 \pm 0.09	15.37 \pm 13.00	3.50 \pm 0.59	0.00000 \pm 0.00128
378	13:29:48.68 +47:11:36.0	2.88 \pm 0.09	3.37 \pm 0.54	14.48 \pm 0.52	10.59 \pm 0.52	3.30 \pm 0.03	2.26 \pm 0.03	8.49 \pm 13.00	2.97 \pm 0.59	0.00478 \pm 0.00179
379	13:29:49.40 +47:11:35.9	9.26 \pm 0.29	7.71 \pm 0.56	54.54 \pm 0.68	23.45 \pm 0.61	7.69 \pm 0.12	4.48 \pm 0.12	178.90 \pm 13.00	5.85 \pm 0.59	0.07174 \pm 0.01538
380	13:29:50.12 +47:11:35.7	20.19 \pm 0.56	15.29 \pm 0.60	145.37 \pm 0.90	45.51 \pm 0.68	14.04 \pm 0.31	9.50 \pm 0.32	758.47 \pm 13.00	7.35 \pm 0.59	0.33097 \pm 0.06894
381	13:29:50.85 +47:11:35.6	41.81 \pm 0.82	21.45 \pm 0.79	222.63 \pm 1.17	65.02 \pm 0.91	17.84 \pm 0.17	11.43 \pm 0.16	270.26 \pm 13.00	7.09 \pm 0.59	0.25906 \pm 0.05294
382	13:29:51.57 +47:11:35.4	30.83 \pm 0.73	18.59 \pm 0.90	160.49 \pm 1.13	55.41 \pm 0.97	13.68 \pm 0.88	8.80 \pm 0.84	202.74 \pm 13.00	4.99 \pm 0.59	0.17437 \pm 0.03602
383	13:29:52.29 +47:11:35.2	44.05 \pm 1.06	31.56 \pm 1.16	222.43 \pm 1.37	94.91 \pm 1.26	18.12 \pm 1.12	14.46 \pm 1.16	79.04 \pm 13.00	3.16 \pm 0.59	0.22918 \pm 0.04732
384	13:29:53.01 +47:11:35.1	48.67 \pm 1.08	29.74 \pm 1.07	239.68 \pm 1.25	88.74 \pm 1.15	15.52 \pm 0.08	11.06 \pm 0.08	134.17 \pm 13.00	3.84 \pm 0.59	0.23391 \pm 0.04807
385	13:29:53.73 +47:11:34.9	37.10 \pm 0.97	23.38 \pm 0.23	203.39 \pm 0.28	71.37 \pm 0.25	14.85 \pm 0.55	11.80 \pm 0.58	246.45 \pm 13.00	3.53 \pm 0.59	0.25203 \pm 0.05220
386	13:29:54.46 +47:11:34.7	29.90 \pm 0.75	20.20 \pm 0.01	173.50 \pm 0.01	58.71 \pm 0.01	13.90 \pm 0.78	11.62 \pm 0.79	272.34 \pm 13.00	4.74 \pm 0.59	0.24306 \pm 0.05018
387	13:29:55.18 +47:11:34.6	29.06 \pm 0.67	20.00 \pm 0.59	162.57 \pm 0.85	56.20 \pm 0.67	17.61 \pm 0.67	12.80 \pm 0.66	542.89 \pm 13.00	7.39 \pm 0.59	0.20882 \pm 0.04300
388	13:29:55.90 +47:11:34.4	11.22 \pm 0.56	6.95 \pm 0.61	51.64 \pm 0.70	20.59 \pm 0.64	4.65 \pm 0.04	3.64 \pm 0.05	47.75 \pm 13.00	5.45 \pm 0.59	0.03477 \pm 0.00837
389	13:29:56.62 +47:11:34.2	9.66 \pm 0.49	6.72 \pm 0.47	42.33 \pm 0.54	17.52 \pm 0.49	4.12 \pm 0.49	3.27 \pm 0.51	28.70 \pm 13.00	3.44 \pm 0.59	0.02282 \pm 0.00572
390	13:29:57.34 +47:11:34.1	11.16 \pm 0.47	5.58 \pm 0.11	50.78 \pm 0.13	15.57 \pm 0.11	5.00 \pm 0.10	3.63 \pm 0.11	11.06 \pm 13.00	3.99 \pm 0.	

TABLE 1 — *Continued*

ID	Equatorial Coordinates	H β	[NII] λ 6548	H α	[NII] λ 6584	[SII] λ 6717	[SII] λ 6731	Σ_{H_2}	Σ_{HI}	Σ_{SFR}
396	13:29:51.19 +47:11:29.1	20.80 \pm 0.15	14.61 \pm 0.75	110.60 \pm 0.91	43.55 \pm 0.82	11.41 \pm 0.39	8.66 \pm 0.40	170.64 \pm 13.00	8.35 \pm 0.59	0.12289 \pm 0.02477
397	13:29:51.92 +47:11:28.9	36.86 \pm 0.18	28.43 \pm 0.48	183.22 \pm 0.59	80.62 \pm 0.52	18.80 \pm 0.44	13.63 \pm 0.44	158.08 \pm 13.00	9.06 \pm 0.59	0.18022 \pm 0.03611
398	13:29:52.64 +47:11:28.8	33.45 \pm 0.83	20.60 \pm 0.90	171.70 \pm 1.13	57.32 \pm 0.97	12.85 \pm 0.76	9.68 \pm 0.76	244.56 \pm 13.00	5.04 \pm 0.59	0.18121 \pm 0.03752
399	13:29:53.36 +47:11:28.6	34.09 \pm 0.83	21.48 \pm 0.19	186.20 \pm 0.25	59.92 \pm 0.21	13.99 \pm 0.75	10.52 \pm 0.76	300.82 \pm 13.00	8.69 \pm 0.59	0.22784 \pm 0.04696
400	13:29:54.08 +47:11:28.5	26.50 \pm 0.71	17.87 \pm 0.76	141.15 \pm 0.97	53.69 \pm 0.84	13.04 \pm 0.75	8.97 \pm 0.72	351.04 \pm 13.00	5.28 \pm 0.59	0.16046 \pm 0.03342
401	13:29:54.80 +47:11:28.3	12.81 \pm 0.30	12.83 \pm 0.56	76.85 \pm 0.67	36.51 \pm 0.61	10.76 \pm 0.13	8.30 \pm 0.13	276.19 \pm 13.00	6.34 \pm 0.59	0.11031 \pm 0.02284
402	13:29:55.53 +47:11:28.1	6.39 \pm 0.11	6.24 \pm 0.59	31.72 \pm 0.63	16.95 \pm 0.62	4.07 \pm 0.57	2.85 \pm 0.65	66.82 \pm 13.00	4.12 \pm 0.59	0.02231 \pm 0.00481
403	13:29:56.25 +47:11:28.0	5.08 \pm 0.45	5.18 \pm 0.52	21.03 \pm 0.53	13.97 \pm 0.53	3.86 \pm 0.01	1.74 \pm 0.01	10.13 \pm 13.00	5.41 \pm 0.59	0.00402 \pm 0.00280
404	13:29:56.97 +47:11:27.8	6.11 \pm 0.43	4.35 \pm 0.47	22.75 \pm 0.50	12.37 \pm 0.48	3.72 \pm 0.46	2.63 \pm 0.47	0.00 \pm 13.00	7.01 \pm 0.59	0.00190 \pm 0.00187
405	13:29:47.21 +47:11:23.6	16.81 \pm 0.47	7.45 \pm 0.44	72.22 \pm 0.65	22.76 \pm 0.50	7.03 \pm 0.43	5.09 \pm 0.42	10.06 \pm 13.00	6.32 \pm 0.59	0.04395 \pm 0.00936
406	13:29:47.93 +47:11:23.5	2.56 \pm 0.38	2.32 \pm 0.21	8.73 \pm 0.22	6.04 \pm 0.23	1.98 \pm 0.02	2.21 \pm 0.03	28.82 \pm 13.00	3.97 \pm 0.59	0.00000 \pm 0.00117
407	13:29:48.65 +47:11:23.3	2.90 \pm 0.09	3.49 \pm 0.51	12.93 \pm 0.47	7.67 \pm 0.46	1.82 \pm 0.46	1.47 \pm 0.43	0.22 \pm 13.00	3.91 \pm 0.59	0.00000 \pm 0.00104
408	13:29:49.38 +47:11:23.1	6.17 \pm 0.24	5.91 \pm 0.52	38.00 \pm 0.60	16.51 \pm 0.54	5.32 \pm 0.50	4.49 \pm 0.50	48.02 \pm 13.00	4.12 \pm 0.59	0.05279 \pm 0.01183
409	13:29:50.10 +47:11:23.0	45.86 \pm 0.66	29.64 \pm 0.54	251.35 \pm 0.94	87.33 \pm 0.67	23.84 \pm 0.60	17.91 \pm 0.58	997.09 \pm 13.00	6.66 \pm 0.59	0.31377 \pm 0.06347
410	13:29:50.82 +47:11:22.8	10.15 \pm 0.27	7.97 \pm 0.59	54.35 \pm 0.69	25.21 \pm 0.64	6.15 \pm 0.12	4.97 \pm 0.12	360.30 \pm 13.00	6.23 \pm 0.59	0.05601 \pm 0.01187
411	13:29:51.54 +47:11:22.7	30.36 \pm 0.37	13.10 \pm 0.36	151.02 \pm 0.51	37.23 \pm 0.39	8.58 \pm 0.04	6.60 \pm 0.05	131.27 \pm 13.00	6.58 \pm 0.59	0.14692 \pm 0.02965
412	13:29:52.26 +47:11:22.5	22.56 \pm 0.68	14.09 \pm 0.71	117.04 \pm 0.92	42.48 \pm 0.79	11.04 \pm 0.37	7.63 \pm 0.38	237.14 \pm 13.00	5.15 \pm 0.59	0.12327 \pm 0.02600
413	13:29:52.98 +47:11:22.3	25.60 \pm 0.67	17.95 \pm 0.72	138.21 \pm 0.96	54.14 \pm 0.81	14.50 \pm 0.37	11.06 \pm 0.38	340.97 \pm 13.00	7.07 \pm 0.59	0.16199 \pm 0.03370
414	13:29:53.71 +47:11:22.2	28.37 \pm 0.70	14.79 \pm 0.38	139.97 \pm 0.51	43.39 \pm 0.42	10.71 \pm 0.69	7.22 \pm 0.68	245.33 \pm 13.00	3.85 \pm 0.59	0.13273 \pm 0.02745
415	13:29:54.43 +47:11:22.0	13.86 \pm 0.48	10.98 \pm 0.62	68.42 \pm 0.72	32.13 \pm 0.67	8.10 \pm 0.12	6.88 \pm 0.14	270.02 \pm 13.00	4.52 \pm 0.59	0.05953 \pm 0.01294
416	13:29:55.15 +47:11:21.8	6.09 \pm 0.49	4.62 \pm 0.53	24.62 \pm 0.57	16.12 \pm 0.57	3.60 \pm 0.10	3.31 \pm 0.12	30.41 \pm 13.00	5.94 \pm 0.59	0.00562 \pm 0.00291
417	13:29:55.87 +47:11:21.7	6.72 \pm 0.46	5.26 \pm 0.52	28.46 \pm 0.56	14.15 \pm 0.53	4.34 \pm 0.49	2.79 \pm 0.49	38.58 \pm 13.00	3.59 \pm 0.59	0.01018 \pm 0.00358
418	13:29:56.59 +47:11:21.5	8.27 \pm 0.43	5.73 \pm 0.49	42.64 \pm 0.57	15.39 \pm 0.50	4.68 \pm 0.46	3.23 \pm 0.44	28.39 \pm 13.00	6.40 \pm 0.59	0.03743 \pm 0.00907
419	13:29:57.32 +47:11:21.4	13.80 \pm 0.43	6.33 \pm 0.48	63.90 \pm 0.65	18.33 \pm 0.52	6.28 \pm 0.48	4.24 \pm 0.47	32.13 \pm 13.00	6.25 \pm 0.59	0.04635 \pm 0.00999
420	13:29:47.56 +47:11:17.2	1.75 \pm 0.01	3.06 \pm 0.52	7.74 \pm 0.43	6.51 \pm 0.42	1.82 \pm 0.33	1.51 \pm 0.38	30.00 \pm 13.00	5.04 \pm 0.59	0.00000 \pm 0.00075
421	13:29:48.28 +47:11:17.0	1.90 \pm 0.34	2.72 \pm 0.47	10.69 \pm 0.43	6.08 \pm 0.42	1.74 \pm 0.07	1.27 \pm 0.08	53.10 \pm 13.00	3.66 \pm 0.59	0.00398 \pm 0.00532
422	13:29:49.00 +47:11:16.9	2.37 \pm 0.08	2.65 \pm 0.47	11.00 \pm 0.46	7.11 \pm 0.48	1.91 \pm 0.40	1.47 \pm 0.39	23.47 \pm 13.00	2.52 \pm 0.59	0.00000 \pm 0.00114
423	13:29:49.72 +47:11:16.7	5.33 \pm 0.45	5.06 \pm 0.50	25.52 \pm 0.53	13.55 \pm 0.52	4.58 \pm 0.11	3.26 \pm 0.10	99.57 \pm 13.00	4.39 \pm 0.59	0.01382 \pm 0.00501
424	13:29:50.44 +47:11:16.5	18.87 \pm 0.52	10.97 \pm 0.01	98.07 \pm 0.02	32.38 \pm 0.01	9.58 \pm 0.46	6.65 \pm 0.46	537.23 \pm 13.00	8.08 \pm 0.59	0.10206 \pm 0.02131
425	13:29:51.17 +47:11:16.4	3.85 \pm 0.24	5.06 \pm 0.32	20.85 \pm 0.29	14.24 \pm 0.29	4.13 \pm 0.04	2.00 \pm 0.04	259.00 \pm 13.00	3.90 \pm 0.59	0.01553 \pm 0.00449
426	13:29:51.89 +47:11:16.2	6.71 \pm 0.50	6.99 \pm 0.59	29.18 \pm 0.61	18.89 \pm 0.61	4.53 \pm 0.56	2.85 \pm 0.51	146.23 \pm 13.00	3.72 \pm 0.59	0.01202 \pm 0.00422
427	13:29:52.61 +47:11:16.0	7.65 \pm 0.50	7.39 \pm 0.64	39.29 \pm 0.64	19.65 \pm 0.62	5.33 \pm 0.14	3.36 \pm 0.11	111.73 \pm 13.00	5.37 \pm 0.59	0.03330 \pm 0.00888
428	13:29:53.33 +47:11:15.9	5.35 \pm 0.48	6.94 \pm 0.59	24.72 \pm 0.59	19.19 \pm 0.61	4.31 \pm 0.56	3.24 \pm 0.58	103.38 \pm 13.00	3.75 \pm 0.59	0.01124 \pm 0.00459
429	13:29:54.05 +47:11:15.7	5.10 \pm 0.46	6.28 \pm 0.51	24.13 \pm 0.50	17.27 \pm 0.51	4.38 \pm 0.53	3.21 \pm 0.55	68.35 \pm 13.00	3.23 \pm 0.59	0.01190 \pm 0.00473
430	13:29:54.78 +47:11:15.6	4.36 \pm 0.44	5.19 \pm 0.04	19.40 \pm 0.04	14.04 \pm 0.04	3.24 \pm 0.01	2.57 \pm 0.01	20.90 \pm 13.00	3.62 \pm 0.59	0.00521 \pm 0.00332
431	13:29:55.50 +47:11:15.4	3.58 \pm 0.41	4.88 \pm 0.58	17.24 \pm 0.51	10.97 \pm 0.51	2.89 \pm 0.10	1.65 \pm 0.10	0.00 \pm 13.00	3.35 \pm 0.59	0.00612 \pm 0.00408
432	13:29:56.22 +47:11:15.2	6.95 \pm 0.23	4.97 \pm 0.48	30.26 \pm 0.54	14.21 \pm 0.50	4.79 \pm 0.09	3.29 \pm 0.10	37.28 \pm 13.00	3.49 \pm 0.59	0.01290 \pm 0.00314
433	13:29:56.94 +47:11:15.1	7.09 \pm 0.43	6.05 \pm 0.50	29.89 \pm 0.54	14.30 \pm 0.49	4.58 \pm 0.47	3.46 \pm 0.46	51.06 \pm 13.00	7.50 \pm 0.59	0.01106 \pm 0.00350
434	13:29:47.18 +47:11:10.9	5.28 \pm 0.08	3.95 \pm 0.42	20.71 \pm 0.44	10.37 \pm 0.41	3.12 \pm 0.37	2.28 \pm 0.38	74.59 \pm 13.00	4.27 \pm 0.59	0.00216 \pm 0.00082
435	13:29:47.90 +47:11:10.7	2.46 \pm 0.08	2.60 \pm 0.44	10.26 \pm 0.41	6.88 \pm 0.42	2.20 \pm 0.39	1.80 \pm 0.42	21.95 \pm 13.00	3.27 \pm 0.59	0.00000 \pm 0.00077
436	13:29:48.63 +47:11:10.6	3.58 \pm 0.23	3.24 \pm 0.46	12.92 \pm 0.45	8.15 \pm 0.45	2.94 \pm 0.03	1.66 \pm 0.03	43.22 \pm 13.00	4.04 \pm 0.59	0.00000 \pm 0.00097
437	13:29:49.35 +47:11:10.4	2.40 \pm 0.36	2.81 \pm 0.47	11.51 \pm 0.47	7.30 \pm 0.46	2.14 \pm 0.43	2.57 \pm 0.61	13.75 \pm 13.00	4.84 \pm 0.59	0.00045 \pm 0.00342
438	13:29:50.07 +47:11:10.3	6.01 \pm 0.09	5.42 \pm 0.48	32.07 \pm 0.54	14.36 \pm 0.49	5.22 \pm 0.50	3.34 \pm 0.47	95.40 \pm 13.00	7.00 \pm 0.59	0.02835 \pm 0.00596
439	13:29:50.79 +47:11:10.1	7.88 \pm 0.42	7.20 \pm 0.48	43.00 \pm 0.58	19.53 \pm 0.53	5.99 \pm 0.48	4.27 \pm 0.47	687.43 \pm 13.00	6.18 \pm 0.59	0.04431 \pm 0.01070
440	13:29:51.51 +47:11:09.9	3.14 \pm 0.40	4.78 \pm 0.54	19.30 \pm 0.53	12.87 \pm 0.53	4.11 \pm 0.51	2.90 \pm 0.52	196.67 \pm 13.00	4.76 \pm 0.59	0.02145 \pm 0.00924
441	13:29:52.24 +47:11:09.8	11.52 \pm 0.27	6.96 \pm 0.53	59.95 \pm 0.68	21.36 \pm 0.57	5.49 \pm 0.03	4.31 \pm 0.04	84.94 \pm 13.00	5.53 \pm 0.59	0.05842 \pm 0.01223
442	13:29:52.96 +47:11:09.6	5.45 \pm 0.43	5.36 \pm 0.52	25.32 \pm 0.54	13.66 \pm 0.52	3.90 \pm 0.27	2.46 \pm 0.28	141.90 \pm 13.00	5.62 \pm 0.59	0.01207 \pm 0.00439
443	13:29:53.68 +47:11:09.4	3.97 \pm 0.03	5.22 \pm 0.54	17.46 \pm 0.51	12.60 \pm 0.51	3.58 \pm 0.27	2.73 \pm 0.25	52.38 \pm 13.00	0.81 \pm 0.59	0.00324 \pm 0.00111
444	13:29:54.40 +47:11:09.3	11.83 \pm 0.43	6.61 \pm 0.52	46.69 \pm 0.61	17.06 \pm 0.54	4.90 \pm 0.03	3.47 \pm 0.03	8.57 \pm 13.00	3.11 \pm 0.59	0.01868 \pm 0.00435
445	13:29:55.12 +47:11:09.1	7.96 \pm 0.45	4.26 \pm 0.43	27.55 \pm 0.47	11.78 \pm 0.44	3.46 \pm 0.48	2.58 \pm 0.52	13.94 \pm 13.00	4.09 \pm 0.59	0.00232 \pm 0.00158
446	13:29:55.84 +47:11:09.0	3.66 \pm 0.09	4.07 \pm 0.55	13.74 \pm 0.49	9.29 \pm 0.49	2.75 \pm 0.03	2.40 \pm 0.04	38.59 \pm 13.00	2.77 \pm 0.59	0.00000 \pm 0.00070
447	13:29:56.57 +47:11:08.8	4.02 \pm 0.37	4.38 \pm 0.43	16.84 \pm 0.41	11.61 \pm 0.42	4.20 \pm 0.24	2.18 \pm 0.23	59.09 \pm 13.00	3.66 \pm 0.59	0.00143 \pm 0.00228
448	13:29:57.29 +47:11:08.6	4.62 \pm 0.36	4.71 \pm 0.24	21.20 \pm 0.25	12.30 \pm 0.25	4.62 \pm 0.09	3			

TABLE 1 — *Continued*

ID	Equatorial Coordinates	H β	[NII] λ 6548	H α	[NII] λ 6584	[SII] λ 6717	[SII] λ 6731	Σ_{H_2}	Σ_{HI}	Σ_{SFR}
453	13:29:50.42 +47:11:03.8	4.00 \pm 0.37	3.75 \pm 0.23	21.05 \pm 0.26	10.04 \pm 0.25	3.01 \pm 0.09	2.12 \pm 0.09	81.47 \pm 13.00	4.18 \pm 0.59	0.01416 \pm 0.00534
454	13:29:51.14 +47:11:03.6	5.08 \pm 0.37	5.70 \pm 0.42	30.07 \pm 0.45	14.42 \pm 0.41	4.86 \pm 0.09	2.84 \pm 0.09	516.69 \pm 13.00	6.85 \pm 0.59	0.03533 \pm 0.00974
455	13:29:51.86 +47:11:03.5	3.59 \pm 0.20	4.61 \pm 0.11	19.37 \pm 0.11	10.47 \pm 0.10	2.32 \pm 0.09	2.37 \pm 0.10	339.47 \pm 13.00	4.98 \pm 0.59	0.01354 \pm 0.00382
456	13:29:52.58 +47:11:03.3	3.42 \pm 0.42	3.66 \pm 0.27	15.33 \pm 0.26	9.51 \pm 0.28	2.81 \pm 0.46	1.86 \pm 0.52	152.12 \pm 13.00	6.12 \pm 0.59	0.00210 \pm 0.00314
457	13:29:53.30 +47:11:03.2	2.18 \pm 0.20	3.79 \pm 0.59	11.18 \pm 0.49	9.47 \pm 0.51	2.07 \pm 0.01	1.29 \pm 0.01	37.46 \pm 13.00	3.24 \pm 0.59	0.00184 \pm 0.00254
458	13:29:54.03 +47:11:03.0	2.85 \pm 0.43	4.11 \pm 0.47	13.36 \pm 0.44	10.19 \pm 0.44	2.88 \pm 0.09	2.47 \pm 0.10	0.00 \pm 13.00	3.23 \pm 0.59	0.00155 \pm 0.00369
459	13:29:54.75 +47:11:02.8	7.69 \pm 0.43	4.88 \pm 0.54	30.00 \pm 0.54	12.56 \pm 0.50	3.39 \pm 0.01	2.56 \pm 0.01	2.39 \pm 13.00	5.47 \pm 0.59	0.00774 \pm 0.00266
460	13:29:55.47 +47:11:02.7	4.60 \pm 0.42	2.82 \pm 0.45	18.06 \pm 0.49	9.81 \pm 0.48	2.84 \pm 0.22	1.89 \pm 0.24	41.98 \pm 13.00	4.71 \pm 0.59	0.00057 \pm 0.00213
461	13:29:56.19 +47:11:02.5	4.16 \pm 0.38	4.34 \pm 0.50	19.65 \pm 0.49	10.58 \pm 0.48	3.63 \pm 0.45	2.34 \pm 0.42	31.16 \pm 13.00	3.43 \pm 0.59	0.00767 \pm 0.00379
462	13:29:56.91 +47:11:02.3	5.55 \pm 0.33	4.98 \pm 0.44	22.95 \pm 0.45	11.97 \pm 0.43	3.63 \pm 0.21	2.45 \pm 0.22	79.50 \pm 13.00	9.65 \pm 0.59	0.00534 \pm 0.00228
463	13:29:47.16 +47:10:58.2	2.56 \pm 0.34	2.23 \pm 0.54	7.24 \pm 0.39	5.02 \pm 0.43	1.50 \pm 0.02	1.37 \pm 0.03	27.88 \pm 13.00	3.07 \pm 0.59	0.00000 \pm 0.00064
464	13:29:47.88 +47:10:58.0	2.33 \pm 0.17	2.21 \pm 0.23	8.87 \pm 0.21	5.33 \pm 0.21	2.24 \pm 0.40	2.24 \pm 0.49	46.50 \pm 13.00	3.71 \pm 0.59	0.00000 \pm 0.00076
465	13:29:48.60 +47:10:57.8	2.51 \pm 0.36	2.49 \pm 0.44	9.83 \pm 0.40	5.95 \pm 0.41	2.21 \pm 0.38	1.12 \pm 0.41	26.36 \pm 13.00	3.47 \pm 0.59	0.00000 \pm 0.00177
466	13:29:49.32 +47:10:57.7	2.17 \pm 0.37	3.44 \pm 0.50	10.38 \pm 0.43	7.89 \pm 0.45	2.57 \pm 0.08	2.17 \pm 0.10	68.79 \pm 13.00	4.25 \pm 0.59	0.00000 \pm 0.00346
467	13:29:50.04 +47:10:57.5	11.46 \pm 0.43	7.86 \pm 0.48	51.61 \pm 0.58	17.90 \pm 0.49	6.22 \pm 0.10	4.16 \pm 0.09	6.42 \pm 13.00	3.92 \pm 0.59	0.03266 \pm 0.00734
468	13:29:50.76 +47:10:57.4	8.53 \pm 0.23	4.86 \pm 0.41	33.37 \pm 0.46	13.30 \pm 0.42	4.12 \pm 0.22	3.56 \pm 0.23	82.59 \pm 13.00	6.65 \pm 0.59	0.00989 \pm 0.00233
469	13:29:51.49 +47:10:57.2	5.75 \pm 0.37	5.92 \pm 0.24	34.94 \pm 0.29	16.13 \pm 0.26	4.82 \pm 0.23	3.14 \pm 0.22	445.63 \pm 13.00	9.49 \pm 0.59	0.04597 \pm 0.01166
470	13:29:52.21 +47:10:57.0	16.24 \pm 0.46	9.94 \pm 0.48	70.85 \pm 0.64	29.35 \pm 0.53	7.14 \pm 0.25	4.87 \pm 0.24	519.78 \pm 13.00	5.97 \pm 0.59	0.04473 \pm 0.00951
471	13:29:52.93 +47:10:56.9	3.10 \pm 0.22	3.58 \pm 0.49	13.98 \pm 0.46	9.36 \pm 0.47	2.97 \pm 0.44	2.21 \pm 0.44	183.82 \pm 13.00	5.25 \pm 0.59	0.00114 \pm 0.00184
472	13:29:53.65 +47:10:56.7	2.85 \pm 0.38	3.47 \pm 0.28	12.78 \pm 0.25	8.38 \pm 0.25	2.61 \pm 0.45	1.96 \pm 0.43	79.25 \pm 13.00	3.40 \pm 0.59	0.00000 \pm 0.00283
473	13:29:54.37 +47:10:56.5	3.16 \pm 0.40	3.49 \pm 0.26	15.74 \pm 0.26	9.83 \pm 0.26	3.31 \pm 0.44	2.40 \pm 0.47	36.41 \pm 13.00	3.81 \pm 0.59	0.00587 \pm 0.00427
474	13:29:55.09 +47:10:56.4	3.93 \pm 0.38	4.28 \pm 0.46	20.78 \pm 0.49	12.59 \pm 0.48	3.53 \pm 0.24	2.87 \pm 0.27	47.46 \pm 13.00	5.38 \pm 0.59	0.01411 \pm 0.00557
475	13:29:55.82 +47:10:56.2	5.29 \pm 0.23	5.22 \pm 0.48	26.42 \pm 0.52	12.67 \pm 0.49	4.34 \pm 0.40	3.09 \pm 0.41	53.91 \pm 13.00	5.95 \pm 0.59	0.01718 \pm 0.00432
476	13:29:56.54 +47:10:56.1	14.98 \pm 0.25	9.94 \pm 0.48	74.22 \pm 0.63	25.77 \pm 0.51	9.03 \pm 0.10	6.64 \pm 0.10	244.23 \pm 13.00	11.94 \pm 0.59	0.06607 \pm 0.01352
477	13:29:57.26 +47:10:55.9	8.81 \pm 0.40	6.88 \pm 0.03	46.46 \pm 0.04	17.45 \pm 0.03	7.09 \pm 0.40	5.53 \pm 0.41	231.83 \pm 13.00	14.72 \pm 0.59	0.04439 \pm 0.01015
478	13:29:47.50 +47:10:51.7	2.41 \pm 0.34	2.22 \pm 0.37	10.44 \pm 0.38	5.05 \pm 0.37	1.76 \pm 0.02	1.90 \pm 0.03	41.73 \pm 13.00	4.13 \pm 0.59	0.00000 \pm 0.00233
479	13:29:48.22 +47:10:51.6	11.12 \pm 0.40	5.03 \pm 0.09	45.53 \pm 0.11	13.17 \pm 0.09	5.02 \pm 0.38	3.75 \pm 0.39	39.82 \pm 13.00	3.70 \pm 0.59	0.02034 \pm 0.00462
480	13:29:48.95 +47:10:51.4	5.54 \pm 0.38	3.68 \pm 0.41	19.51 \pm 0.45	10.35 \pm 0.42	3.98 \pm 0.41	3.14 \pm 0.42	65.80 \pm 13.00	4.00 \pm 0.59	0.00000 \pm 0.00138
481	13:29:49.67 +47:10:51.2	7.18 \pm 0.23	4.77 \pm 0.09	28.05 \pm 0.11	13.13 \pm 0.10	5.02 \pm 0.43	3.95 \pm 0.45	14.20 \pm 13.00	5.83 \pm 0.59	0.00657 \pm 0.00170
482	13:29:50.39 +47:10:51.1	28.19 \pm 0.54	11.66 \pm 0.52	99.69 \pm 0.71	28.95 \pm 0.55	9.53 \pm 0.04	7.08 \pm 0.04	38.68 \pm 13.00	6.29 \pm 0.59	0.03853 \pm 0.00796
483	13:29:51.11 +47:10:50.9	12.17 \pm 0.48	6.44 \pm 0.51	43.82 \pm 0.58	18.69 \pm 0.53	3.96 \pm 0.01	2.85 \pm 0.01	47.22 \pm 13.00	6.56 \pm 0.59	0.01186 \pm 0.00301
484	13:29:51.83 +47:10:50.7	6.33 \pm 0.39	5.93 \pm 0.46	33.83 \pm 0.52	16.93 \pm 0.48	6.04 \pm 0.09	4.48 \pm 0.10	333.67 \pm 13.00	6.82 \pm 0.59	0.03068 \pm 0.00800
485	13:29:52.55 +47:10:50.6	10.66 \pm 0.41	8.68 \pm 0.45	62.21 \pm 0.59	22.30 \pm 0.48	8.26 \pm 0.39	5.66 \pm 0.39	448.81 \pm 13.00	7.59 \pm 0.59	0.08154 \pm 0.01781
486	13:29:53.28 +47:10:50.4	12.63 \pm 0.10	7.13 \pm 0.48	58.58 \pm 0.61	18.58 \pm 0.50	7.07 \pm 0.47	4.81 \pm 0.48	168.79 \pm 13.00	7.88 \pm 0.59	0.04174 \pm 0.00847
487	13:29:54.00 +47:10:50.3	7.95 \pm 0.23	5.43 \pm 0.44	40.48 \pm 0.55	17.39 \pm 0.49	5.87 \pm 0.09	4.47 \pm 0.10	230.78 \pm 13.00	8.42 \pm 0.59	0.03378 \pm 0.00731
488	13:29:54.72 +47:10:50.1	10.01 \pm 0.40	10.12 \pm 0.25	66.20 \pm 0.33	27.38 \pm 0.27	6.93 \pm 0.09	6.77 \pm 0.09	459.87 \pm 13.00	8.09 \pm 0.59	0.11841 \pm 0.02580
489	13:29:55.44 +47:10:49.9	25.07 \pm 0.26	22.56 \pm 0.11	130.56 \pm 0.16	57.73 \pm 0.13	17.02 \pm 0.49	14.62 \pm 0.51	496.56 \pm 13.00	10.12 \pm 0.59	0.14000 \pm 0.02817
490	13:29:56.16 +47:10:49.8	22.14 \pm 0.49	17.89 \pm 0.51	136.01 \pm 0.78	48.55 \pm 0.59	16.40 \pm 0.50	12.67 \pm 0.50	383.70 \pm 13.00	11.84 \pm 0.59	0.21482 \pm 0.04414
491	13:29:48.10 +47:12:31.3	6.02 \pm 0.45	4.56 \pm 0.50	29.58 \pm 0.54	10.82 \pm 0.47	3.50 \pm 0.03	2.61 \pm 0.03	36.97 \pm 13.00	10.65 \pm 0.59	0.01937 \pm 0.00601
492	13:29:48.82 +47:12:31.2	4.63 \pm 0.10	5.80 \pm 0.30	28.08 \pm 0.31	14.24 \pm 0.28	4.94 \pm 0.48	3.06 \pm 0.47	192.62 \pm 13.00	9.30 \pm 0.59	0.03456 \pm 0.00727
493	13:29:49.54 +47:12:31.0	3.68 \pm 0.03	4.71 \pm 0.55	22.70 \pm 0.58	13.45 \pm 0.56	4.98 \pm 0.45	3.57 \pm 0.45	213.36 \pm 13.00	6.82 \pm 0.59	0.02727 \pm 0.00588
494	13:29:50.27 +47:12:30.8	4.60 \pm 0.52	5.05 \pm 0.31	23.99 \pm 0.31	14.37 \pm 0.30	3.75 \pm 0.26	2.55 \pm 0.27	133.67 \pm 13.00	6.91 \pm 0.59	0.01712 \pm 0.00710
495	13:29:50.99 +47:12:30.7	2.27 \pm 0.49	4.63 \pm 0.33	14.07 \pm 0.29	11.65 \pm 0.29	3.71 \pm 0.28	2.60 \pm 0.27	114.05 \pm 13.00	6.22 \pm 0.59	0.01315 \pm 0.01048
496	13:29:51.71 +47:12:30.5	3.36 \pm 0.49	5.43 \pm 0.04	19.00 \pm 0.04	13.67 \pm 0.04	4.10 \pm 0.57	2.66 \pm 0.51	125.76 \pm 13.00	4.67 \pm 0.59	0.01563 \pm 0.00818
497	13:29:52.43 +47:12:30.4	5.32 \pm 0.48	6.46 \pm 0.31	29.29 \pm 0.32	17.44 \pm 0.30	5.33 \pm 0.26	3.99 \pm 0.28	209.26 \pm 13.00	6.93 \pm 0.59	0.02754 \pm 0.00879
498	13:29:53.16 +47:12:30.2	7.33 \pm 0.53	5.09 \pm 0.30	40.37 \pm 0.35	15.05 \pm 0.30	5.13 \pm 0.04	3.56 \pm 0.04	95.44 \pm 13.00	6.39 \pm 0.59	0.04197 \pm 0.01125
499	13:29:53.88 +47:12:30.0	4.58 \pm 0.10	4.76 \pm 0.47	30.24 \pm 0.53	13.09 \pm 0.48	5.17 \pm 0.51	3.87 \pm 0.52	172.97 \pm 13.00	4.94 \pm 0.59	0.04804 \pm 0.01019
500	13:29:54.60 +47:12:29.9	9.26 \pm 0.53	6.95 \pm 0.29	58.15 \pm 0.38	19.68 \pm 0.30	7.01 \pm 0.50	5.38 \pm 0.52	218.21 \pm 13.00	8.32 \pm 0.59	0.09057 \pm 0.02144
501	13:29:55.32 +47:12:29.7	14.99 \pm 0.56	9.43 \pm 0.29	91.76 \pm 0.43	26.18 \pm 0.31	9.85 \pm 0.27	7.22 \pm 0.27	98.59 \pm 13.00	7.93 \pm 0.59	0.14036 \pm 0.03025
502	13:29:56.04 +47:12:29.5	37.18 \pm 0.82	14.99 \pm 0.65	193.77 \pm 1.10	44.73 \pm 0.74	12.19 \pm 0.32	8.62 \pm 0.31	46.22 \pm 13.00	4.62 \pm 0.59	0.21320 \pm 0.04381
503	13:29:56.77 +47:12:29.4	8.71 \pm 0.47	4.88 \pm 0.49	51.43 \pm 0.64	13.32 \pm 0.49	4.77 \pm 0.22	4.04 \pm 0.25	71.26 \pm 13.00	4.30 \pm 0.59	0.06757 \pm 0.01596
504	13:29:57.49 +47:12:29.2	1.93 \pm 0.34	3.67 \pm 0.51	11.62 \pm 0.44	6.68 \pm 0.41	1.80 \pm 0.19	1.93 \pm 0.21	63.40 \pm 13.00	4.44 \pm 0.59	0.00777 \pm 0.00676
505	13:29:47.73 +47:12:25.0	7.55 \pm 0.47	5.38 \pm 0.25	45.20 \pm 0.33	16.29 \pm 0.27	2.96 \pm 0.06	2.93 \pm 0.09	233.57<		

TABLE 1 — *Continued*

ID	Equatorial Coordinates	H β	[NII] λ 6548	H α	[NII] λ 6584	[SII] λ 6717	[SII] λ 6731	Σ_{H_2}	Σ_{HI}	Σ_{SFR}
510	13:29:51.34 +47:12:24.2	3.01 \pm 0.29	4.89 \pm 0.58	16.66 \pm 0.57	12.44 \pm 0.57	4.01 \pm 0.04	2.55 \pm 0.04	90.69 \pm 13.00	7.90 \pm 0.59	0.01133 \pm 0.00503
511	13:29:52.06 +47:12:24.1	7.91 \pm 0.29	6.85 \pm 0.51	53.07 \pm 0.63	21.46 \pm 0.54	6.57 \pm 0.11	3.82 \pm 0.10	104.51 \pm 13.00	6.95 \pm 0.59	0.09622 \pm 0.02095
512	13:29:52.78 +47:12:23.9	6.97 \pm 0.30	6.27 \pm 0.62	34.25 \pm 0.65	15.47 \pm 0.60	3.70 \pm 0.11	1.95 \pm 0.10	182.87 \pm 13.00	4.09 \pm 0.59	0.02417 \pm 0.00583
513	13:29:53.50 +47:12:23.7	11.89 \pm 0.60	8.15 \pm 0.32	65.01 \pm 0.41	24.05 \pm 0.34	7.86 \pm 0.56	6.16 \pm 0.57	92.69 \pm 13.00	4.72 \pm 0.59	0.07284 \pm 0.01675
514	13:29:54.22 +47:12:23.6	10.09 \pm 0.61	8.01 \pm 0.05	54.56 \pm 0.05	17.32 \pm 0.04	6.24 \pm 0.32	4.68 \pm 0.32	136.93 \pm 13.00	7.65 \pm 0.59	0.05764 \pm 0.01407
515	13:29:54.95 +47:12:23.4	12.74 \pm 0.12	7.76 \pm 0.52	76.02 \pm 0.78	23.18 \pm 0.59	7.98 \pm 0.27	4.99 \pm 0.25	272.46 \pm 13.00	8.71 \pm 0.59	0.10756 \pm 0.02178
516	13:29:55.67 +47:12:23.3	8.75 \pm 0.51	6.43 \pm 0.54	51.25 \pm 0.69	17.85 \pm 0.56	6.51 \pm 0.51	4.58 \pm 0.50	89.13 \pm 13.00	8.28 \pm 0.59	0.06593 \pm 0.01599
517	13:29:56.39 +47:12:23.1	11.95 \pm 0.55	7.60 \pm 0.55	62.22 \pm 0.72	17.68 \pm 0.56	6.21 \pm 0.26	4.05 \pm 0.24	43.78 \pm 13.00	7.12 \pm 0.59	0.06114 \pm 0.01395
518	13:29:57.11 +47:12:22.9	5.13 \pm 0.10	4.76 \pm 0.50	27.36 \pm 0.55	11.63 \pm 0.49	3.65 \pm 0.03	2.88 \pm 0.03	33.45 \pm 13.00	4.32 \pm 0.59	0.02259 \pm 0.00490
519	13:29:57.83 +47:12:22.8	1.93 \pm 0.42	3.01 \pm 0.54	9.09 \pm 0.45	6.78 \pm 0.45	2.34 \pm 0.03	1.62 \pm 0.03	71.14 \pm 13.00	4.09 \pm 0.59	0.00000 \pm 0.00371
520	13:29:48.07 +47:12:18.6	2.68 \pm 0.45	3.86 \pm 0.29	16.30 \pm 0.27	10.47 \pm 0.27	3.41 \pm 0.11	2.28 \pm 0.10	100.69 \pm 13.00	5.49 \pm 0.59	0.01567 \pm 0.00920
521	13:29:48.80 +47:12:18.4	2.85 \pm 0.11	3.71 \pm 0.36	14.24 \pm 0.29	9.32 \pm 0.29	3.34 \pm 0.11	1.36 \pm 0.10	84.18 \pm 13.00	4.78 \pm 0.59	0.00438 \pm 0.00160
522	13:29:49.52 +47:12:18.3	3.03 \pm 0.44	5.40 \pm 0.64	15.90 \pm 0.57	12.96 \pm 0.58	4.08 \pm 0.11	2.62 \pm 0.10	47.80 \pm 13.00	3.11 \pm 0.59	0.00802 \pm 0.00571
523	13:29:50.24 +47:12:18.1	2.86 \pm 0.47	4.51 \pm 0.61	16.07 \pm 0.57	11.47 \pm 0.56	4.82 \pm 0.56	3.03 \pm 0.53	0.00 \pm 13.00	2.94 \pm 0.59	0.01123 \pm 0.00759
524	13:29:50.96 +47:12:17.9	3.85 \pm 0.27	5.02 \pm 0.51	24.55 \pm 0.53	13.35 \pm 0.50	3.57 \pm 0.04	2.63 \pm 0.03	28.41 \pm 13.00	6.49 \pm 0.59	0.03347 \pm 0.00922
525	13:29:51.68 +47:12:17.8	8.37 \pm 0.61	8.19 \pm 0.36	51.04 \pm 0.39	18.31 \pm 0.34	5.30 \pm 0.59	4.22 \pm 0.59	90.08 \pm 13.00	4.69 \pm 0.59	0.07269 \pm 0.01880
526	13:29:52.41 +47:12:17.6	11.57 \pm 0.62	10.04 \pm 0.35	66.22 \pm 0.42	27.66 \pm 0.37	8.56 \pm 0.33	5.46 \pm 0.31	50.72 \pm 13.00	3.78 \pm 0.59	0.08330 \pm 0.01943
527	13:29:53.13 +47:12:17.5	21.81 \pm 0.72	10.99 \pm 0.15	122.82 \pm 0.21	28.58 \pm 0.15	9.09 \pm 0.13	6.28 \pm 0.13	96.01 \pm 13.00	5.46 \pm 0.59	0.15762 \pm 0.03337
528	13:29:53.85 +47:12:17.3	25.62 \pm 0.72	12.28 \pm 0.63	151.00 \pm 1.05	36.13 \pm 0.71	10.64 \pm 0.32	7.30 \pm 0.31	158.08 \pm 13.00	6.67 \pm 0.59	0.21794 \pm 0.04548
529	13:29:54.57 +47:12:17.1	40.42 \pm 0.82	16.60 \pm 0.58	209.22 \pm 1.03	46.44 \pm 0.66	14.42 \pm 0.13	10.40 \pm 0.13	158.51 \pm 13.00	8.92 \pm 0.59	0.22752 \pm 0.04655
530	13:29:55.29 +47:12:17.0	7.86 \pm 0.27	7.95 \pm 0.13	51.10 \pm 0.15	21.95 \pm 0.13	6.75 \pm 0.11	5.64 \pm 0.11	291.65 \pm 13.00	6.89 \pm 0.59	0.08517 \pm 0.01826
531	13:29:56.02 +47:12:16.8	7.11 \pm 0.11	6.81 \pm 0.30	43.83 \pm 0.35	17.73 \pm 0.30	6.13 \pm 0.03	4.58 \pm 0.04	58.02 \pm 13.00	7.22 \pm 0.59	0.06253 \pm 0.01276
532	13:29:56.74 +47:12:16.6	10.68 \pm 0.55	7.28 \pm 0.50	65.47 \pm 0.66	19.19 \pm 0.51	6.76 \pm 0.28	4.85 \pm 0.28	27.42 \pm 13.00	3.78 \pm 0.59	0.09732 \pm 0.02245
533	13:29:57.46 +47:12:16.5	2.97 \pm 0.09	4.13 \pm 0.27	14.45 \pm 0.24	9.15 \pm 0.24	2.62 \pm 0.09	1.77 \pm 0.10	51.01 \pm 13.00	2.13 \pm 0.59	0.00373 \pm 0.00122
534	13:29:47.70 +47:12:12.3	4.21 \pm 0.27	3.95 \pm 0.13	17.09 \pm 0.11	8.54 \pm 0.11	3.02 \pm 0.10	2.44 \pm 0.10	64.43 \pm 13.00	6.31 \pm 0.59	0.00078 \pm 0.00143
535	13:29:48.42 +47:12:12.1	2.17 \pm 0.49	4.47 \pm 0.52	11.73 \pm 0.46	10.15 \pm 0.48	3.51 \pm 0.51	2.03 \pm 0.50	23.85 \pm 13.00	4.22 \pm 0.59	0.00400 \pm 0.00662
536	13:29:49.14 +47:12:12.0	3.94 \pm 0.04	5.34 \pm 0.32	20.77 \pm 0.31	13.23 \pm 0.30	3.69 \pm 0.11	3.09 \pm 0.12	21.16 \pm 13.00	3.19 \pm 0.59	0.01392 \pm 0.00293
537	13:29:49.86 +47:12:11.8	4.81 \pm 0.55	5.56 \pm 0.62	21.64 \pm 0.60	12.50 \pm 0.59	3.02 \pm 0.11	2.26 \pm 0.11	6.09 \pm 13.00	3.74 \pm 0.59	0.00751 \pm 0.00450
538	13:29:50.59 +47:12:11.7	11.33 \pm 0.53	7.86 \pm 0.62	58.40 \pm 0.76	23.27 \pm 0.66	6.95 \pm 0.31	4.70 \pm 0.31	0.00 \pm 13.00	3.18 \pm 0.59	0.05522 \pm 0.01274
539	13:29:51.31 +47:12:11.5	14.50 \pm 0.63	12.17 \pm 0.59	90.05 \pm 0.78	32.71 \pm 0.63	10.19 \pm 0.65	6.27 \pm 0.62	56.44 \pm 13.00	3.47 \pm 0.59	0.14226 \pm 0.03145
540	13:29:52.03 +47:12:11.3	41.00 \pm 0.85	20.20 \pm 0.77	211.88 \pm 1.22	53.95 \pm 0.85	15.96 \pm 0.73	11.44 \pm 0.73	100.66 \pm 13.00	3.44 \pm 0.59	0.22968 \pm 0.04706
541	13:29:52.75 +47:12:11.2	23.54 \pm 0.74	12.74 \pm 0.73	125.00 \pm 1.02	34.50 \pm 0.78	10.04 \pm 0.37	6.66 \pm 0.36	198.54 \pm 13.00	4.20 \pm 0.59	0.13986 \pm 0.02959
542	13:29:53.47 +47:12:11.0	29.34 \pm 0.16	13.51 \pm 0.69	152.00 \pm 1.07	38.20 \pm 0.77	11.87 \pm 0.36	8.88 \pm 0.35	110.17 \pm 13.00	4.71 \pm 0.59	0.16270 \pm 0.03270
543	13:29:54.20 +47:12:10.8	56.76 \pm 0.93	19.33 \pm 0.73	288.84 \pm 1.36	52.89 \pm 0.83	14.81 \pm 0.15	11.47 \pm 0.15	137.54 \pm 13.00	6.84 \pm 0.59	0.30614 \pm 0.06215
544	13:29:54.92 +47:12:10.7	33.38 \pm 0.84	11.81 \pm 0.39	160.65 \pm 0.57	31.92 \pm 0.40	9.73 \pm 0.35	7.37 \pm 0.36	181.12 \pm 13.00	6.28 \pm 0.59	0.14519 \pm 0.03006
545	13:29:55.64 +47:12:10.5	7.62 \pm 0.44	8.72 \pm 0.49	49.98 \pm 0.60	24.20 \pm 0.53	7.46 \pm 0.52	6.15 \pm 0.55	337.71 \pm 13.00	6.02 \pm 0.59	0.08516 \pm 0.02036
546	13:29:56.36 +47:12:10.4	6.21 \pm 0.52	5.07 \pm 0.31	34.14 \pm 0.34	12.70 \pm 0.30	3.53 \pm 0.26	3.55 \pm 0.29	56.56 \pm 13.00	8.09 \pm 0.59	0.03371 \pm 0.00995
547	13:29:57.08 +47:12:10.2	2.94 \pm 0.44	3.77 \pm 0.30	16.52 \pm 0.28	9.27 \pm 0.27	3.39 \pm 0.10	1.80 \pm 0.09	30.31 \pm 13.00	3.45 \pm 0.59	0.01184 \pm 0.00703
548	13:29:57.81 +47:12:10.0	1.54 \pm 0.40	3.22 \pm 0.54	7.93 \pm 0.48	7.76 \pm 0.49	3.17 \pm 0.51	1.80 \pm 0.49	0.00 \pm 13.00	2.18 \pm 0.59	0.00000 \pm 0.00476
549	13:29:48.05 +47:12:05.9	2.79 \pm 0.49	3.51 \pm 0.29	14.47 \pm 0.28	9.67 \pm 0.27	2.97 \pm 0.04	2.27 \pm 0.03	11.26 \pm 13.00	4.94 \pm 0.59	0.00593 \pm 0.00585
550	13:29:48.77 +47:12:05.7	5.53 \pm 0.52	5.82 \pm 0.56	27.24 \pm 0.60	15.89 \pm 0.57	4.74 \pm 0.11	2.66 \pm 0.10	29.97 \pm 13.00	5.26 \pm 0.59	0.01722 \pm 0.00635
551	13:29:49.49 +47:12:05.5	6.98 \pm 0.53	5.22 \pm 0.04	37.06 \pm 0.05	15.66 \pm 0.04	4.90 \pm 0.13	2.83 \pm 0.12	58.67 \pm 13.00	5.47 \pm 0.59	0.03393 \pm 0.00952
552	13:29:50.21 +47:12:05.4	5.36 \pm 0.48	7.15 \pm 0.40	33.37 \pm 0.36	17.01 \pm 0.34	4.26 \pm 0.59	2.88 \pm 0.59	44.17 \pm 13.00	4.06 \pm 0.59	0.04621 \pm 0.01369
553	13:29:50.93 +47:12:05.2	20.79 \pm 0.73	13.83 \pm 0.74	129.11 \pm 1.02	39.11 \pm 0.80	11.14 \pm 0.38	8.11 \pm 0.36	0.00 \pm 13.00	3.28 \pm 0.59	0.20858 \pm 0.04449
554	13:29:51.66 +47:12:05.1	59.12 \pm 1.02	30.17 \pm 0.78	343.35 \pm 1.32	93.25 \pm 0.93	27.30 \pm 0.90	19.79 \pm 0.88	298.50 \pm 13.00	4.32 \pm 0.59	0.49247 \pm 0.10006
555	13:29:52.38 +47:12:04.9	55.06 \pm 1.00	36.13 \pm 0.50	321.45 \pm 0.79	107.51 \pm 0.60	31.14 \pm 0.83	22.98 \pm 0.80	378.08 \pm 13.00	4.93 \pm 0.59	0.46587 \pm 0.09475
556	13:29:53.10 +47:12:04.7	27.99 \pm 0.87	16.40 \pm 0.45	142.01 \pm 0.60	51.01 \pm 0.51	14.13 \pm 0.18	9.27 \pm 0.18	272.60 \pm 13.00	7.12 \pm 0.59	0.14400 \pm 0.03034
557	13:29:53.82 +47:12:04.6	17.94 \pm 0.76	12.39 \pm 0.82	104.51 \pm 1.02	32.42 \pm 0.86	8.78 \pm 0.05	5.69 \pm 0.05	177.08 \pm 13.00	7.71 \pm 0.59	0.14354 \pm 0.03160
558	13:29:54.54 +47:12:04.4	66.23 \pm 0.99	19.91 \pm 0.43	354.50 \pm 0.79	56.04 \pm 0.47	17.73 \pm 0.78	11.89 \pm 0.76	68.62 \pm 13.00	9.12 \pm 0.59	0.42373 \pm 0.08572
559	13:29:55.27 +47:12:04.2	28.14 \pm 0.69	13.24 \pm 0.14	167.69 \pm 0.23	37.16 \pm 0.15	12.56 \pm 0.32	8.95 \pm 0.31	433.94 \pm 13.00	7.63 \pm 0.59	0.24944 \pm 0.05144
560	13:29:55.99 +47:12:04.1	13.31 \pm 0.55	9.38 \pm 0.58	76.00 \pm 0.79	25.19 \pm 0.63	8.62 \pm 0.56	5.99 \pm 0.56	174.10 \pm 13.00	7.57 \pm 0.59	0.09670 \pm 0.02137
561	13:29:56.71 +47:12:03.9	8.56 \pm 0.57	6.43 \pm 0.58	46.07 \pm 0.70	18.65 \pm 0.62	6.16 \pm 0.12	4.36 \pm 0.11	50.19 \pm 13.00	5.59 \pm 0.59	0.04654 \pm 0.01209
562	13:29:57.43 +47:12:03.7	2.66 \pm 0.45	3.93 \pm 0.52	14.18 \pm 0.52	11.09 \pm 0.52	3				

TABLE 1 — *Continued*

ID	Equatorial Coordinates	H β	[NII] λ 6548	H α	[NII] λ 6584	[SII] λ 6717	[SII] λ 6731	Σ_{H_2}	Σ_{HI}	Σ_{SFR}
567	13:29:50.56 +47:11:58.9	26.31 \pm 0.76	22.57 \pm 0.40	194.36 \pm 0.61	65.20 \pm 0.47	18.90 \pm 0.39	15.26 \pm 0.39	316.12 \pm 13.00	5.55 \pm 0.59	0.47247 \pm 0.09838
568	13:29:51.28 +47:11:58.8	41.98 \pm 0.93	25.18 \pm 0.91	238.19 \pm 1.34	77.32 \pm 1.05	21.25 \pm 0.47	16.45 \pm 0.48	674.85 \pm 13.00	6.86 \pm 0.59	0.32094 \pm 0.06591
569	13:29:52.00 +47:11:58.6	39.68 \pm 0.93	34.63 \pm 0.59	233.67 \pm 0.77	109.30 \pm 0.70	26.10 \pm 0.23	19.85 \pm 0.24	510.09 \pm 13.00	4.91 \pm 0.59	0.34238 \pm 0.07041
570	13:29:52.73 +47:11:58.4	43.64 \pm 1.09	56.61 \pm 0.67	233.14 \pm 0.78	171.88 \pm 0.79	35.97 \pm 0.25	27.15 \pm 0.26	288.68 \pm 13.00	3.78 \pm 0.59	0.27375 \pm 0.05654
571	13:29:53.45 +47:11:58.3	30.05 \pm 0.97	19.72 \pm 0.86	161.30 \pm 1.10	62.24 \pm 0.97	14.84 \pm 0.20	10.50 \pm 0.20	149.46 \pm 13.00	5.77 \pm 0.59	0.18819 \pm 0.03978
572	13:29:54.17 +47:11:58.1	20.28 \pm 0.84	12.98 \pm 0.90	110.51 \pm 1.07	35.08 \pm 0.94	8.66 \pm 0.18	7.12 \pm 0.18	50.87 \pm 13.00	5.59 \pm 0.59	0.13024 \pm 0.02861
573	13:29:54.89 +47:11:58.0	32.07 \pm 0.76	15.92 \pm 0.72	187.44 \pm 1.14	45.85 \pm 0.81	15.34 \pm 0.15	9.97 \pm 0.15	194.68 \pm 13.00	5.72 \pm 0.59	0.26797 \pm 0.05525
574	13:29:55.61 +47:11:57.8	17.14 \pm 0.60	10.27 \pm 0.61	112.97 \pm 0.91	30.39 \pm 0.68	9.80 \pm 0.04	6.38 \pm 0.04	516.67 \pm 13.00	9.01 \pm 0.59	0.20797 \pm 0.04442
575	13:29:56.34 +47:11:57.6	63.27 \pm 0.93	21.25 \pm 0.73	278.27 \pm 1.29	60.07 \pm 0.84	19.71 \pm 0.72	13.06 \pm 0.69	132.29 \pm 13.00	6.44 \pm 0.59	0.21092 \pm 0.04272
576	13:29:57.06 +47:11:57.5	12.65 \pm 0.04	6.93 \pm 0.52	59.14 \pm 0.65	22.35 \pm 0.54	6.53 \pm 0.54	3.74 \pm 0.49	32.88 \pm 13.00	4.36 \pm 0.59	0.04321 \pm 0.00874
577	13:29:57.78 +47:11:57.3	4.74 \pm 0.46	3.74 \pm 0.28	20.59 \pm 0.28	9.57 \pm 0.26	3.01 \pm 0.24	1.91 \pm 0.22	11.77 \pm 13.00	4.75 \pm 0.59	0.00532 \pm 0.00323
578	13:29:48.02 +47:11:53.1	2.92 \pm 0.10	3.15 \pm 0.27	11.09 \pm 0.27	8.76 \pm 0.27	3.44 \pm 0.03	2.29 \pm 0.04	28.13 \pm 13.00	3.26 \pm 0.59	0.00000 \pm 0.00056
579	13:29:48.74 +47:11:53.0	4.53 \pm 0.48	3.50 \pm 0.53	19.58 \pm 0.56	10.45 \pm 0.54	2.79 \pm 0.10	2.48 \pm 0.10	12.10 \pm 13.00	5.33 \pm 0.59	0.00434 \pm 0.00338
580	13:29:49.46 +47:11:52.8	6.68 \pm 0.12	7.28 \pm 0.65	41.73 \pm 0.70	19.49 \pm 0.64	5.87 \pm 0.13	4.41 \pm 0.13	39.09 \pm 13.00	4.35 \pm 0.59	0.06117 \pm 0.01276
581	13:29:50.18 +47:11:52.6	25.73 \pm 0.72	18.10 \pm 0.73	167.80 \pm 1.07	54.63 \pm 0.83	18.31 \pm 0.65	12.45 \pm 0.62	412.26 \pm 13.00	6.89 \pm 0.59	0.30664 \pm 0.06393
582	13:29:50.91 +47:11:52.5	27.52 \pm 0.86	18.63 \pm 0.87	168.03 \pm 1.17	60.36 \pm 0.99	15.50 \pm 0.87	10.76 \pm 0.85	433.07 \pm 13.00	8.15 \pm 0.59	0.26418 \pm 0.05562
583	13:29:51.63 +47:11:52.3	30.54 \pm 0.08	25.45 \pm 1.16	172.37 \pm 1.38	85.38 \pm 1.32	17.10 \pm 0.24	14.26 \pm 0.26	402.65 \pm 13.00	5.26 \pm 0.59	0.22666 \pm 0.04553
584	13:29:52.35 +47:11:52.2	37.65 \pm 0.28	94.75 \pm 0.34	174.61 \pm 0.34	290.33 \pm 0.41	54.01 \pm 1.53	43.83 \pm 1.58	327.95 \pm 13.00	4.79 \pm 0.59	0.13020 \pm 0.02615
585	13:29:53.07 +47:11:52.0	43.85 \pm 1.26	102.59 \pm 0.83	208.75 \pm 0.85	306.80 \pm 0.99	63.93 \pm 0.80	48.03 \pm 0.81	192.07 \pm 13.00	4.32 \pm 0.59	0.16736 \pm 0.03534
586	13:29:53.79 +47:11:51.8	44.45 \pm 1.07	25.61 \pm 0.60	231.01 \pm 0.75	75.21 \pm 0.64	17.64 \pm 0.23	12.78 \pm 0.22	89.55 \pm 13.00	3.78 \pm 0.59	0.25470 \pm 0.05249
587	13:29:54.52 +47:11:51.7	22.81 \pm 0.80	17.57 \pm 0.87	127.49 \pm 1.08	49.96 \pm 0.94	13.88 \pm 0.84	10.73 \pm 0.87	115.70 \pm 13.00	3.88 \pm 0.59	0.16112 \pm 0.03445
588	13:29:55.24 +47:11:51.5	42.32 \pm 0.81	18.93 \pm 0.75	229.98 \pm 1.22	57.26 \pm 0.86	15.61 \pm 0.15	11.53 \pm 0.15	131.04 \pm 13.00	5.40 \pm 0.59	0.28067 \pm 0.05730
589	13:29:55.96 +47:11:51.3	36.60 \pm 0.43	19.59 \pm 0.71	204.10 \pm 1.13	55.20 \pm 0.81	15.86 \pm 0.14	12.03 \pm 0.14	396.88 \pm 13.00	7.74 \pm 0.59	0.26293 \pm 0.05307
590	13:29:56.68 +47:11:51.2	15.01 \pm 0.62	8.36 \pm 0.55	71.08 \pm 0.68	23.59 \pm 0.57	7.38 \pm 0.51	5.59 \pm 0.53	25.92 \pm 13.00	4.71 \pm 0.59	0.05587 \pm 0.01248
591	13:29:57.40 +47:11:51.0	7.09 \pm 0.27	6.25 \pm 0.50	36.13 \pm 0.53	15.36 \pm 0.47	4.07 \pm 0.49	3.88 \pm 0.51	44.55 \pm 13.00	4.50 \pm 0.59	0.02915 \pm 0.00666
592	13:29:47.64 +47:11:46.8	3.15 \pm 0.45	3.85 \pm 0.54	10.73 \pm 0.48	7.84 \pm 0.47	2.31 \pm 0.42	1.66 \pm 0.45	15.14 \pm 13.00	3.80 \pm 0.59	0.00000 \pm 0.00145
593	13:29:48.37 +47:11:46.7	3.55 \pm 0.44	4.38 \pm 0.29	16.79 \pm 0.28	9.68 \pm 0.27	2.84 \pm 0.10	1.92 \pm 0.09	7.68 \pm 13.00	5.16 \pm 0.59	0.00503 \pm 0.00399
594	13:29:49.09 +47:11:46.5	4.17 \pm 0.52	4.88 \pm 0.64	23.78 \pm 0.62	12.43 \pm 0.61	3.61 \pm 0.01	2.25 \pm 0.01	7.25 \pm 13.00	6.72 \pm 0.59	0.02290 \pm 0.00958
595	13:29:49.81 +47:11:46.4	21.10 \pm 0.73	11.98 \pm 0.73	116.09 \pm 0.97	34.51 \pm 0.78	8.72 \pm 0.14	6.10 \pm 0.14	212.27 \pm 13.00	6.80 \pm 0.59	0.14037 \pm 0.02999
596	13:29:50.53 +47:11:46.2	31.26 \pm 0.77	26.08 \pm 0.81	204.11 \pm 1.18	77.98 \pm 0.95	22.17 \pm 0.43	15.96 \pm 0.41	313.65 \pm 13.00	9.99 \pm 0.59	0.37610 \pm 0.07768
597	13:29:51.25 +47:11:46.0	43.30 \pm 1.05	26.01 \pm 1.10	233.20 \pm 1.41	71.80 \pm 1.18	16.22 \pm 1.03	14.11 \pm 1.07	204.80 \pm 13.00	5.73 \pm 0.59	0.27902 \pm 0.05761
598	13:29:51.98 +47:11:45.9	28.88 \pm 1.15	49.12 \pm 0.81	137.59 \pm 0.79	154.86 \pm 0.92	22.64 \pm 1.41	21.31 \pm 1.49	112.87 \pm 13.00	3.47 \pm 0.59	0.10724 \pm 0.02380
599	13:29:52.70 +47:11:45.7	88.76 \pm 2.02	462.58 \pm 2.91	519.94 \pm 2.89	1315.30 \pm 3.54	204.99 \pm 2.67	242.63 \pm 2.96	246.51 \pm 13.00	3.81 \pm 0.59	0.68499 \pm 0.14161
600	13:29:53.42 +47:11:45.5	35.58 \pm 1.28	77.54 \pm 1.60	167.10 \pm 1.58	227.92 \pm 1.84	39.07 \pm 1.52	30.51 \pm 1.53	141.07 \pm 13.00	3.62 \pm 0.59	0.12787 \pm 0.02797
601	13:29:54.14 +47:11:45.4	49.70 \pm 1.06	26.40 \pm 1.06	267.84 \pm 1.45	78.55 \pm 1.17	18.50 \pm 0.22	14.21 \pm 0.22	141.91 \pm 13.00	3.19 \pm 0.59	0.32252 \pm 0.06609
602	13:29:54.86 +47:11:45.2	34.31 \pm 0.82	17.78 \pm 0.81	183.87 \pm 1.15	50.12 \pm 0.89	14.08 \pm 0.41	10.84 \pm 0.43	148.35 \pm 13.00	5.38 \pm 0.59	0.21525 \pm 0.04443
603	13:29:55.59 +47:11:45.1	59.09 \pm 0.48	31.59 \pm 0.17	337.29 \pm 0.29	88.33 \pm 0.20	24.04 \pm 0.16	18.38 \pm 0.15	469.65 \pm 13.00	8.53 \pm 0.59	0.46524 \pm 0.09336
604	13:29:56.31 +47:11:44.9	19.38 \pm 0.63	11.32 \pm 0.57	100.65 \pm 0.75	33.73 \pm 0.61	8.72 \pm 0.32	7.12 \pm 0.33	95.77 \pm 13.00	7.62 \pm 0.59	0.10483 \pm 0.02232
605	13:29:57.03 +47:11:44.7	5.42 \pm 0.25	5.09 \pm 0.29	25.38 \pm 0.30	12.88 \pm 0.29	4.06 \pm 0.27	3.34 \pm 0.27	15.56 \pm 13.00	5.90 \pm 0.59	0.01256 \pm 0.00334
606	13:29:57.75 +47:11:44.6	3.15 \pm 0.03	4.28 \pm 0.47	13.45 \pm 0.43	10.96 \pm 0.44	3.16 \pm 0.09	2.47 \pm 0.10	29.87 \pm 13.00	3.82 \pm 0.59	0.00000 \pm 0.00072
607	13:29:47.99 +47:11:40.4	4.83 \pm 0.43	4.12 \pm 0.52	19.43 \pm 0.52	9.71 \pm 0.48	3.01 \pm 0.03	2.01 \pm 0.03	43.63 \pm 13.00	3.82 \pm 0.59	0.00208 \pm 0.00236
608	13:29:48.71 +47:11:40.2	3.42 \pm 0.03	5.38 \pm 0.57	16.19 \pm 0.55	12.35 \pm 0.56	2.81 \pm 0.03	3.07 \pm 0.03	0.00 \pm 13.00	3.64 \pm 0.59	0.00454 \pm 0.00146
609	13:29:49.43 +47:11:40.1	11.38 \pm 0.59	9.45 \pm 0.64	71.72 \pm 0.80	26.51 \pm 0.68	8.82 \pm 0.13	5.39 \pm 0.13	126.49 \pm 13.00	6.67 \pm 0.59	0.11519 \pm 0.02654
610	13:29:50.16 +47:11:39.9	26.88 \pm 0.68	19.39 \pm 0.69	190.79 \pm 1.08	55.33 \pm 0.79	15.39 \pm 0.35	11.06 \pm 0.34	628.39 \pm 13.00	8.14 \pm 0.59	0.42378 \pm 0.08761
611	13:29:50.88 +47:11:39.8	29.24 \pm 0.79	19.07 \pm 0.45	168.89 \pm 0.59	51.74 \pm 0.49	13.99 \pm 0.17	9.93 \pm 0.17	259.86 \pm 13.00	7.00 \pm 0.59	0.23397 \pm 0.04860
612	13:29:51.60 +47:11:39.6	31.79 \pm 0.96	23.81 \pm 0.91	168.01 \pm 1.09	70.01 \pm 1.01	14.89 \pm 0.21	10.71 \pm 0.22	132.25 \pm 13.00	3.31 \pm 0.59	0.18951 \pm 0.03981
613	13:29:52.32 +47:11:39.4	39.14 \pm 1.20	70.19 \pm 0.33	185.84 \pm 0.33	206.95 \pm 0.38	39.17 \pm 0.32	32.13 \pm 0.33	122.09 \pm 13.00	1.38 \pm 0.59	0.14704 \pm 0.03126
614	13:29:53.04 +47:11:39.3	38.53 \pm 1.29	152.04 \pm 0.40	169.43 \pm 0.36	425.89 \pm 0.47	70.71 \pm 0.12	72.96 \pm 0.13	119.88 \pm 13.00	3.13 \pm 0.59	0.11109 \pm 0.02394
615	13:29:53.77 +47:11:39.1	29.92 \pm 1.03	25.72 \pm 1.18	162.62 \pm 1.33	77.57 \pm 1.28	16.13 \pm 1.18	11.15 \pm 1.12	167.12 \pm 13.00	4.50 \pm 0.59	0.19537 \pm 0.04165
616	13:29:54.49 +47:11:38.9	39.72 \pm 0.93	27.21 \pm 0.86	200.26 \pm 1.10	81.93 \pm 0.97	18.87 \pm 0.50	16.21 \pm 0.52	192.39 \pm 13.00	4.93 \pm 0.59	0.20455 \pm 0.04217
617	13:29:55.21 +47:11:38.8	26.40 \pm 0.68	21.40 \pm 0.38	180.01 \pm 0.56	62.14 \pm 0.44	19.23 \pm 0.70	14.59 \pm 0.68	477.56 \pm 13.00	9.68 \pm 0.59	0.36437 \pm 0.07532
618	13:29:55.93 +47:11:38.6	17.52 \pm 0.66	11.08 \pm 0.15	82.50 \pm 0.18	29.71 \pm 0.15	8.68 \pm 0.62	6.10 \pm 0.63	111.89 \pm 13.00	9.05 \pm 0.59	0.06565 \pm

TABLE 1 — *Continued*

ID	Equatorial Coordinates	H β	[NII] λ 6548	H α	[NII] λ 6584	[SII] λ 6717	[SII] λ 6731	Σ_{H_2}	Σ_{HI}	Σ_{SFR}
624	13:29:49.78 +47:11:33.6	13.71 \pm 0.30	12.26 \pm 0.04	103.06 \pm 0.06	35.09 \pm 0.05	10.58 \pm 0.57	7.05 \pm 0.56	593.61 \pm 13.00	8.37 \pm 0.59	0.25522 \pm 0.05229
625	13:29:50.50 +47:11:33.5	24.47 \pm 0.65	16.27 \pm 0.69	164.32 \pm 1.01	47.79 \pm 0.77	14.34 \pm 0.15	9.27 \pm 0.14	525.32 \pm 13.00	7.11 \pm 0.59	0.32042 \pm 0.06650
626	13:29:51.23 +47:11:33.3	23.96 \pm 0.75	17.17 \pm 0.81	124.17 \pm 1.01	51.69 \pm 0.90	12.09 \pm 0.79	8.66 \pm 0.81	278.45 \pm 13.00	6.83 \pm 0.59	0.13103 \pm 0.02772
627	13:29:51.95 +47:11:33.1	36.17 \pm 0.91	24.82 \pm 1.00	190.56 \pm 1.24	73.37 \pm 1.10	16.18 \pm 0.97	12.63 \pm 1.00	147.02 \pm 13.00	6.43 \pm 0.59	0.21489 \pm 0.04451
628	13:29:52.67 +47:11:33.0	56.87 \pm 1.10	27.53 \pm 1.12	287.14 \pm 1.48	84.50 \pm 1.24	17.36 \pm 0.24	12.43 \pm 0.23	146.83 \pm 13.00	3.91 \pm 0.59	0.29882 \pm 0.06101
629	13:29:53.39 +47:11:32.8	29.38 \pm 0.96	23.80 \pm 1.10	171.15 \pm 1.31	70.49 \pm 1.20	12.50 \pm 0.07	9.10 \pm 0.07	236.59 \pm 13.00	4.43 \pm 0.59	0.24191 \pm 0.05120
630	13:29:54.11 +47:11:32.7	38.49 \pm 0.93	22.06 \pm 0.53	205.50 \pm 0.67	63.90 \pm 0.57	14.41 \pm 0.20	11.37 \pm 0.20	268.56 \pm 13.00	3.65 \pm 0.59	0.23981 \pm 0.04946
631	13:29:54.84 +47:11:32.5	22.09 \pm 0.64	15.50 \pm 0.68	153.56 \pm 0.99	48.13 \pm 0.78	14.58 \pm 0.68	10.50 \pm 0.68	397.47 \pm 13.00	5.66 \pm 0.59	0.32333 \pm 0.06754
632	13:29:55.56 +47:11:32.3	17.03 \pm 0.35	9.04 \pm 0.58	81.77 \pm 0.72	25.54 \pm 0.60	6.83 \pm 0.13	5.95 \pm 0.14	226.11 \pm 13.00	5.44 \pm 0.59	0.06832 \pm 0.01412
633	13:29:56.28 +47:11:32.2	9.04 \pm 0.54	5.85 \pm 0.56	39.97 \pm 0.66	18.18 \pm 0.60	4.32 \pm 0.01	4.34 \pm 0.01	33.99 \pm 13.00	4.19 \pm 0.59	0.02157 \pm 0.00585
634	13:29:57.00 +47:11:32.0	10.02 \pm 0.50	5.98 \pm 0.47	45.72 \pm 0.55	14.88 \pm 0.47	5.06 \pm 0.26	3.28 \pm 0.25	2.63 \pm 13.00	3.87 \pm 0.59	0.02882 \pm 0.00704
635	13:29:57.72 +47:11:31.8	6.58 \pm 0.25	4.42 \pm 0.11	29.26 \pm 0.12	11.18 \pm 0.11	3.84 \pm 0.10	2.64 \pm 0.11	24.44 \pm 13.00	4.93 \pm 0.59	0.01325 \pm 0.00321
636	13:29:47.96 +47:11:27.7	3.48 \pm 0.44	2.68 \pm 0.25	10.17 \pm 0.24	6.40 \pm 0.23	2.97 \pm 0.25	0.85 \pm 0.21	8.69 \pm 13.00	3.70 \pm 0.59	0.00000 \pm 0.00084
637	13:29:48.69 +47:11:27.5	3.59 \pm 0.45	3.71 \pm 0.04	15.27 \pm 0.04	10.46 \pm 0.04	2.46 \pm 0.24	2.16 \pm 0.25	14.02 \pm 13.00	3.46 \pm 0.59	0.00067 \pm 0.00279
638	13:29:49.41 +47:11:27.3	9.65 \pm 0.52	8.76 \pm 0.60	61.67 \pm 0.72	20.90 \pm 0.60	7.94 \pm 0.52	5.99 \pm 0.50	108.57 \pm 13.00	5.36 \pm 0.59	0.10076 \pm 0.02351
639	13:29:50.13 +47:11:27.2	46.50 \pm 0.37	30.70 \pm 0.66	266.40 \pm 1.15	88.93 \pm 0.82	25.96 \pm 0.65	19.58 \pm 0.63	1063.21 \pm 13.00	7.72 \pm 0.59	0.36817 \pm 0.07396
640	13:29:50.85 +47:11:27.0	19.98 \pm 0.65	13.01 \pm 0.70	112.47 \pm 0.91	37.21 \pm 0.76	9.56 \pm 0.67	7.51 \pm 0.67	225.74 \pm 13.00	7.29 \pm 0.59	0.14324 \pm 0.03039
641	13:29:51.57 +47:11:26.9	23.12 \pm 0.71	14.07 \pm 0.79	130.57 \pm 1.00	37.62 \pm 0.82	10.37 \pm 0.17	7.43 \pm 0.16	147.73 \pm 13.00	10.35 \pm 0.59	0.16938 \pm 0.03571
642	13:29:52.30 +47:11:26.7	34.56 \pm 0.79	24.37 \pm 0.87	186.12 \pm 1.13	67.32 \pm 0.95	18.26 \pm 0.45	13.67 \pm 0.45	227.93 \pm 13.00	5.77 \pm 0.59	0.22050 \pm 0.04541
643	13:29:53.02 +47:11:26.5	29.82 \pm 0.82	22.06 \pm 0.82	159.52 \pm 0.98	56.84 \pm 0.85	13.44 \pm 0.18	9.77 \pm 0.17	348.26 \pm 13.00	8.45 \pm 0.59	0.18449 \pm 0.03846
644	13:29:53.74 +47:11:26.4	37.93 \pm 0.81	23.57 \pm 0.83	211.54 \pm 1.17	64.45 \pm 0.93	17.27 \pm 0.43	12.97 \pm 0.42	339.07 \pm 13.00	7.05 \pm 0.59	0.27301 \pm 0.05598
645	13:29:54.46 +47:11:26.2	23.79 \pm 0.66	18.45 \pm 0.70	126.40 \pm 0.94	53.29 \pm 0.80	15.06 \pm 0.69	11.69 \pm 0.69	301.70 \pm 13.00	6.07 \pm 0.59	0.14180 \pm 0.02964
646	13:29:55.18 +47:11:26.0	8.66 \pm 0.30	9.06 \pm 0.65	41.80 \pm 0.69	23.79 \pm 0.65	5.95 \pm 0.04	4.31 \pm 0.04	91.44 \pm 13.00	5.67 \pm 0.59	0.03017 \pm 0.00679
647	13:29:55.90 +47:11:25.9	5.20 \pm 0.50	4.19 \pm 0.51	21.92 \pm 0.57	12.83 \pm 0.57	3.64 \pm 0.10	2.55 \pm 0.11	0.00 \pm 13.00	3.83 \pm 0.59	0.00528 \pm 0.00329
648	13:29:56.63 +47:11:25.7	5.81 \pm 0.10	5.22 \pm 0.51	22.83 \pm 0.53	13.10 \pm 0.51	4.33 \pm 0.26	2.99 \pm 0.24	0.00 \pm 13.00	7.99 \pm 0.59	0.00352 \pm 0.00111
649	13:29:57.35 +47:11:25.6	7.50 \pm 0.45	5.03 \pm 0.45	31.66 \pm 0.48	14.31 \pm 0.44	4.37 \pm 0.10	3.17 \pm 0.10	11.69 \pm 13.00	6.19 \pm 0.59	0.01240 \pm 0.00377
650	13:29:47.59 +47:11:21.4	4.70 \pm 0.36	3.87 \pm 0.54	16.14 \pm 0.47	8.27 \pm 0.45	2.90 \pm 0.44	1.84 \pm 0.48	37.42 \pm 13.00	5.20 \pm 0.59	0.00000 \pm 0.00121
651	13:29:48.31 +47:11:21.2	1.91 \pm 0.39	4.29 \pm 0.15	7.90 \pm 0.09	5.69 \pm 0.10	1.73 \pm 0.03	1.42 \pm 0.04	24.62 \pm 13.00	4.03 \pm 0.59	0.00000 \pm 0.00220
652	13:29:49.03 +47:11:21.1	3.07 \pm 0.03	3.71 \pm 0.57	15.58 \pm 0.51	7.90 \pm 0.50	3.20 \pm 0.11	2.42 \pm 0.10	1.27 \pm 13.00	3.81 \pm 0.59	0.00630 \pm 0.00177
653	13:29:49.75 +47:11:20.9	9.53 \pm 0.03	10.80 \pm 0.57	60.54 \pm 0.69	27.44 \pm 0.60	8.42 \pm 0.53	6.68 \pm 0.53	365.44 \pm 13.00	4.75 \pm 0.59	0.09724 \pm 0.01964
654	13:29:50.48 +47:11:20.7	33.30 \pm 0.62	17.38 \pm 0.61	149.93 \pm 0.91	49.39 \pm 0.69	13.67 \pm 0.32	10.15 \pm 0.31	721.94 \pm 13.00	7.50 \pm 0.59	0.11502 \pm 0.02352
655	13:29:51.20 +47:11:20.6	10.53 \pm 0.54	10.53 \pm 0.54	57.44 \pm 0.73	22.63 \pm 0.66	5.62 \pm 0.32	4.37 \pm 0.31	167.78 \pm 13.00	4.58 \pm 0.59	0.06276 \pm 0.01473
656	13:29:51.92 +47:11:20.4	15.14 \pm 0.13	10.96 \pm 0.64	85.97 \pm 0.82	28.58 \pm 0.70	6.16 \pm 0.31	5.56 \pm 0.35	202.24 \pm 13.00	4.37 \pm 0.59	0.10930 \pm 0.02209
657	13:29:52.64 +47:11:20.2	11.93 \pm 0.13	12.54 \pm 0.75	64.94 \pm 0.80	34.49 \pm 0.77	7.66 \pm 0.36	6.10 \pm 0.39	238.48 \pm 13.00	5.32 \pm 0.59	0.07192 \pm 0.01466
658	13:29:53.36 +47:11:20.1	14.48 \pm 0.34	12.18 \pm 0.69	77.71 \pm 0.81	31.96 \pm 0.73	8.23 \pm 0.13	6.11 \pm 0.14	231.95 \pm 13.00	4.71 \pm 0.59	0.08511 \pm 0.01770
659	13:29:54.09 +47:11:19.9	17.61 \pm 0.54	11.56 \pm 0.57	87.93 \pm 0.72	31.14 \pm 0.61	8.62 \pm 0.64	6.64 \pm 0.65	174.63 \pm 13.00	3.45 \pm 0.59	0.08186 \pm 0.01736
660	13:29:54.81 +47:11:19.8	6.34 \pm 0.50	6.58 \pm 0.62	28.70 \pm 0.62	16.85 \pm 0.61	5.06 \pm 0.58	3.03 \pm 0.60	86.77 \pm 13.00	4.70 \pm 0.59	0.01372 \pm 0.00479
661	13:29:55.53 +47:11:19.6	4.87 \pm 0.25	5.11 \pm 0.30	20.71 \pm 0.30	12.96 \pm 0.29	4.38 \pm 0.59	2.11 \pm 0.51	40.96 \pm 13.00	4.31 \pm 0.59	0.00471 \pm 0.00189
662	13:29:56.25 +47:11:19.4	10.81 \pm 0.27	6.89 \pm 0.54	53.26 \pm 0.65	17.89 \pm 0.55	5.60 \pm 0.26	3.39 \pm 0.25	34.38 \pm 13.00	3.57 \pm 0.59	0.04378 \pm 0.00926
663	13:29:56.97 +47:11:19.3	10.91 \pm 0.26	6.62 \pm 0.51	54.60 \pm 0.63	17.60 \pm 0.52	5.26 \pm 0.48	3.67 \pm 0.49	32.82 \pm 13.00	7.22 \pm 0.59	0.04709 \pm 0.00990
664	13:29:57.70 +47:11:19.1	7.15 \pm 0.45	6.11 \pm 0.53	34.58 \pm 0.57	15.83 \pm 0.51	5.36 \pm 0.47	3.50 \pm 0.46	97.47 \pm 13.00	4.93 \pm 0.59	0.02329 \pm 0.00636
665	13:29:47.94 +47:11:14.9	1.90 \pm 0.35	3.01 \pm 0.51	8.23 \pm 0.42	5.87 \pm 0.42	1.96 \pm 0.24	1.20 \pm 0.22	19.99 \pm 13.00	2.98 \pm 0.59	0.00000 \pm 0.00238
666	13:29:48.66 +47:11:14.8	3.50 \pm 0.03	3.99 \pm 0.13	16.05 \pm 0.10	8.12 \pm 0.10	2.73 \pm 0.03	1.47 \pm 0.03	34.10 \pm 13.00	2.88 \pm 0.59	0.00340 \pm 0.00074
667	13:29:49.38 +47:11:14.6	2.82 \pm 0.46	4.23 \pm 0.30	13.12 \pm 0.28	8.66 \pm 0.28	2.48 \pm 0.01	1.71 \pm 0.01	0.00 \pm 13.00	3.43 \pm 0.59	0.00114 \pm 0.00379
668	13:29:50.10 +47:11:14.5	8.73 \pm 0.48	8.24 \pm 0.31	49.40 \pm 0.34	19.64 \pm 0.30	5.82 \pm 0.04	3.79 \pm 0.03	198.32 \pm 13.00	7.22 \pm 0.59	0.05766 \pm 0.01371
669	13:29:50.82 +47:11:14.3	8.82 \pm 0.41	7.77 \pm 0.12	53.83 \pm 0.14	20.46 \pm 0.12	5.70 \pm 0.11	3.98 \pm 0.11	564.64 \pm 13.00	6.27 \pm 0.59	0.07739 \pm 0.01745
670	13:29:51.55 +47:11:14.1	2.68 \pm 0.40	5.95 \pm 0.59	17.13 \pm 0.55	13.70 \pm 0.57	3.48 \pm 0.11	1.83 \pm 0.11	133.49 \pm 13.00	3.26 \pm 0.59	0.02045 \pm 0.01023
671	13:29:52.27 +47:11:14.0	5.65 \pm 0.43	7.75 \pm 0.63	33.47 \pm 0.63	18.92 \pm 0.62	5.15 \pm 0.04	4.18 \pm 0.04	110.42 \pm 13.00	5.44 \pm 0.59	0.04066 \pm 0.01134
672	13:29:52.99 +47:11:13.8	7.80 \pm 0.27	7.33 \pm 0.56	38.35 \pm 0.56	18.21 \pm 0.54	5.16 \pm 0.56	3.64 \pm 0.58	92.11 \pm 13.00	4.45 \pm 0.59	0.02835 \pm 0.00640
673	13:29:53.71 +47:11:13.6	4.12 \pm 0.25	6.16 \pm 0.59	20.64 \pm 0.57	14.49 \pm 0.56	3.90 \pm 0.11	3.42 \pm 0.13	70.86 \pm 13.00	2.14 \pm 0.59	0.01121 \pm 0.00364
674	13:29:54.43 +47:11:13.5	4.44 \pm 0.26	6.86 \pm 0.60	21.21 \pm 0.55	15.42 \pm 0.56	5.42 \pm 0.58	3.21 \pm 0.61	47.79 \pm 13.00	3.37 \pm 0.59	0.00960 \pm 0.00320
675	13:29:55.15 +47:11:13.3	4.60 \pm 0.46	5.47 \pm 0.60	17.12 \pm 0.54	11.90 \pm 0.54	3.45 \pm 0.04	2.29 \pm 0.04	0.00 \pm 13.00	3.44 \pm 0.59	0.00000 \pm 0.00198
676	13:29:55.88 +47:11:13.1	3.59 \pm 0.42	3.10 \pm 0.53	15.91 \pm 0.51	9.					

TABLE 1 — *Continued*

ID	Equatorial Coordinates	H β	[NII] λ 6548	H α	[NII] λ 6584	[SII] λ 6717	[SII] λ 6731	Σ_{H_2}	Σ_{HI}	Σ_{SFR}
681	13:29:49.01 +47:11:08.3	2.51 \pm 0.41	4.09 \pm 0.56	11.81 \pm 0.48	8.57 \pm 0.48	2.77 \pm 0.52	2.33 \pm 0.50	5.15 \pm 13.00	4.93 \pm 0.59	0.00030 \pm 0.00361
682	13:29:49.73 +47:11:08.2	2.96 \pm 0.36	3.96 \pm 0.45	16.72 \pm 0.44	9.70 \pm 0.43	3.23 \pm 0.04	1.95 \pm 0.03	22.06 \pm 13.00	5.70 \pm 0.59	0.01249 \pm 0.00627
683	13:29:50.45 +47:11:08.0	8.11 \pm 0.45	6.20 \pm 0.51	44.44 \pm 0.59	16.25 \pm 0.51	5.16 \pm 0.03	3.71 \pm 0.03	317.27 \pm 13.00	5.53 \pm 0.59	0.04670 \pm 0.01132
684	13:29:51.17 +47:11:07.8	3.85 \pm 0.41	5.03 \pm 0.11	23.32 \pm 0.11	13.41 \pm 0.11	4.81 \pm 0.04	2.70 \pm 0.03	507.74 \pm 13.00	6.07 \pm 0.59	0.02682 \pm 0.00949
685	13:29:51.89 +47:11:07.7	4.71 \pm 0.44	5.39 \pm 0.30	26.65 \pm 0.30	12.97 \pm 0.29	4.79 \pm 0.54	2.74 \pm 0.50	127.12 \pm 13.00	3.87 \pm 0.59	0.02625 \pm 0.00862
686	13:29:52.61 +47:11:07.5	5.65 \pm 0.45	5.65 \pm 0.04	24.33 \pm 0.04	12.60 \pm 0.04	3.91 \pm 0.27	1.98 \pm 0.27	119.83 \pm 13.00	7.10 \pm 0.59	0.00784 \pm 0.00328
687	13:29:53.34 +47:11:07.4	4.00 \pm 0.44	4.49 \pm 0.55	17.15 \pm 0.52	11.50 \pm 0.52	4.08 \pm 0.57	2.44 \pm 0.48	79.25 \pm 13.00	2.79 \pm 0.59	0.00227 \pm 0.00293
688	13:29:54.06 +47:11:07.2	4.57 \pm 0.42	5.36 \pm 0.12	22.18 \pm 0.11	12.74 \pm 0.11	3.22 \pm 0.24	2.53 \pm 0.28	3.31 \pm 13.00	2.46 \pm 0.59	0.01126 \pm 0.00456
689	13:29:54.78 +47:11:07.0	22.47 \pm 0.30	8.19 \pm 0.56	92.29 \pm 0.75	20.13 \pm 0.55	6.09 \pm 0.50	4.36 \pm 0.50	0.00 \pm 13.00	4.79 \pm 0.59	0.05259 \pm 0.01070
690	13:29:55.50 +47:11:06.9	4.25 \pm 0.43	4.99 \pm 0.33	17.82 \pm 0.28	9.61 \pm 0.27	2.76 \pm 0.03	2.70 \pm 0.04	21.26 \pm 13.00	3.91 \pm 0.59	0.00213 \pm 0.00258
691	13:29:56.22 +47:11:06.7	4.20 \pm 0.25	4.67 \pm 0.29	14.52 \pm 0.26	10.64 \pm 0.27	3.21 \pm 0.48	2.34 \pm 0.48	7.51 \pm 13.00	2.09 \pm 0.59	0.00000 \pm 0.00085
692	13:29:56.95 +47:11:06.5	5.72 \pm 0.42	6.27 \pm 0.55	25.80 \pm 0.53	12.75 \pm 0.49	4.83 \pm 0.10	3.30 \pm 0.09	69.46 \pm 13.00	5.86 \pm 0.59	0.01102 \pm 0.00395
693	13:29:57.67 +47:11:06.4	9.21 \pm 0.41	8.11 \pm 0.47	49.48 \pm 0.57	21.26 \pm 0.50	8.51 \pm 0.10	5.80 \pm 0.10	111.83 \pm 13.00	8.32 \pm 0.59	0.05041 \pm 0.01149
694	13:29:47.91 +47:11:02.2	2.07 \pm 0.18	3.24 \pm 0.56	7.43 \pm 0.42	4.74 \pm 0.41	1.66 \pm 0.41	1.59 \pm 0.41	51.09 \pm 13.00	4.98 \pm 0.59	0.00000 \pm 0.00078
695	13:29:48.63 +47:11:02.0	2.22 \pm 0.36	2.48 \pm 0.25	8.07 \pm 0.23	5.81 \pm 0.23	2.01 \pm 0.03	1.98 \pm 0.03	27.11 \pm 13.00	3.95 \pm 0.59	0.00000 \pm 0.00137
696	13:29:49.35 +47:11:01.9	2.34 \pm 0.32	2.84 \pm 0.51	11.70 \pm 0.46	7.20 \pm 0.46	2.62 \pm 0.42	1.90 \pm 0.48	82.92 \pm 13.00	4.11 \pm 0.59	0.00167 \pm 0.00345
697	13:29:50.07 +47:11:01.7	5.71 \pm 0.03	5.01 \pm 0.12	24.65 \pm 0.11	11.22 \pm 0.10	2.79 \pm 0.09	2.66 \pm 0.10	0.39 \pm 13.00	3.77 \pm 0.59	0.00821 \pm 0.00166
698	13:29:50.80 +47:11:01.6	4.79 \pm 0.40	5.13 \pm 0.53	21.60 \pm 0.50	10.12 \pm 0.47	3.37 \pm 0.25	3.50 \pm 0.25	204.13 \pm 13.00	6.27 \pm 0.59	0.00755 \pm 0.00349
699	13:29:51.52 +47:11:01.4	4.97 \pm 0.40	5.32 \pm 0.53	22.45 \pm 0.50	11.62 \pm 0.47	3.35 \pm 0.09	2.05 \pm 0.09	544.35 \pm 13.00	7.75 \pm 0.59	0.00832 \pm 0.00357
700	13:29:52.24 +47:11:01.2	5.53 \pm 0.43	3.98 \pm 0.48	22.86 \pm 0.52	10.98 \pm 0.49	2.87 \pm 0.10	2.78 \pm 0.10	316.47 \pm 13.00	5.09 \pm 0.59	0.00522 \pm 0.00277
701	13:29:52.96 +47:11:01.1	3.07 \pm 0.42	4.49 \pm 0.49	13.58 \pm 0.44	10.05 \pm 0.45	2.45 \pm 0.03	1.84 \pm 0.04	80.43 \pm 13.00	4.96 \pm 0.59	0.00029 \pm 0.00300
702	13:29:53.68 +47:11:00.9	2.03 \pm 0.35	3.67 \pm 0.53	9.17 \pm 0.48	8.24 \pm 0.51	2.13 \pm 0.42	1.74 \pm 0.62	0.00 \pm 13.00	2.32 \pm 0.59	0.00000 \pm 0.00275
703	13:29:54.41 +47:11:00.7	3.43 \pm 0.43	4.57 \pm 0.58	13.08 \pm 0.50	9.34 \pm 0.50	2.84 \pm 0.24	2.33 \pm 0.24	0.00 \pm 13.00	3.60 \pm 0.59	0.00000 \pm 0.00197
704	13:29:55.13 +47:11:00.6	4.48 \pm 0.42	4.56 \pm 0.49	20.43 \pm 0.52	10.22 \pm 0.49	3.43 \pm 0.03	1.84 \pm 0.03	51.86 \pm 13.00	5.11 \pm 0.59	0.00700 \pm 0.00364
705	13:29:55.85 +47:11:00.4	4.44 \pm 0.42	4.17 \pm 0.27	18.39 \pm 0.27	11.23 \pm 0.28	3.41 \pm 0.48	2.55 \pm 0.51	33.04 \pm 13.00	4.30 \pm 0.59	0.00218 \pm 0.00248
706	13:29:56.57 +47:11:00.3	5.42 \pm 0.42	4.90 \pm 0.50	27.73 \pm 0.53	13.41 \pm 0.50	5.28 \pm 0.49	3.72 \pm 0.49	81.95 \pm 13.00	8.68 \pm 0.59	0.02005 \pm 0.00625
707	13:29:57.29 +47:11:00.1	5.75 \pm 0.38	5.74 \pm 0.49	26.10 \pm 0.48	11.91 \pm 0.45	4.26 \pm 0.09	2.87 \pm 0.09	167.90 \pm 13.00	12.36 \pm 0.59	0.01164 \pm 0.00382
708	13:29:47.53 +47:10:55.9	1.72 \pm 0.33	1.76 \pm 0.43	7.05 \pm 0.41	4.08 \pm 0.38	1.16 \pm 0.38	0.71 \pm 0.37	47.71 \pm 13.00	3.15 \pm 0.59	0.00000 \pm 0.00189
709	13:29:48.26 +47:10:55.8	4.11 \pm 0.20	2.85 \pm 0.22	16.46 \pm 0.24	6.15 \pm 0.21	2.61 \pm 0.41	2.16 \pm 0.45	26.71 \pm 13.00	4.09 \pm 0.59	0.00003 \pm 0.00106
710	13:29:48.98 +47:10:55.6	2.88 \pm 0.38	2.99 \pm 0.11	11.10 \pm 0.09	6.79 \pm 0.09	2.25 \pm 0.23	2.16 \pm 0.25	58.72 \pm 13.00	4.35 \pm 0.59	0.00000 \pm 0.00171
711	13:29:49.70 +47:10:55.4	5.25 \pm 0.25	4.47 \pm 0.50	21.01 \pm 0.51	10.98 \pm 0.48	3.95 \pm 0.46	2.63 \pm 0.46	36.32 \pm 13.00	4.74 \pm 0.59	0.00294 \pm 0.00157
712	13:29:50.42 +47:10:55.3	26.54 \pm 0.53	12.53 \pm 0.51	104.37 \pm 0.74	32.41 \pm 0.57	10.82 \pm 0.10	8.70 \pm 0.11	29.94 \pm 13.00	5.42 \pm 0.59	0.05438 \pm 0.01122
713	13:29:51.14 +47:10:55.1	6.44 \pm 0.41	4.42 \pm 0.43	29.18 \pm 0.47	11.67 \pm 0.42	3.02 \pm 0.22	2.70 \pm 0.24	197.55 \pm 13.00	8.59 \pm 0.59	0.01418 \pm 0.00428
714	13:29:51.87 +47:10:54.9	13.01 \pm 0.44	11.07 \pm 0.48	81.83 \pm 0.68	33.45 \pm 0.55	7.76 \pm 0.46	5.75 \pm 0.47	609.42 \pm 13.00	7.48 \pm 0.59	0.13224 \pm 0.02818
715	13:29:52.59 +47:10:54.8	8.04 \pm 0.37	6.70 \pm 0.26	43.93 \pm 0.31	18.75 \pm 0.27	4.72 \pm 0.44	3.38 \pm 0.43	358.98 \pm 13.00	6.02 \pm 0.59	0.04570 \pm 0.01047
716	13:29:53.31 +47:10:54.6	2.88 \pm 0.20	3.87 \pm 0.04	17.39 \pm 0.03	9.59 \pm 0.03	2.82 \pm 0.43	1.79 \pm 0.46	161.05 \pm 13.00	4.37 \pm 0.59	0.01715 \pm 0.00506
717	13:29:54.03 +47:10:54.5	4.32 \pm 0.40	3.93 \pm 0.48	21.83 \pm 0.51	10.76 \pm 0.49	2.36 \pm 0.22	2.40 \pm 0.26	118.86 \pm 13.00	5.39 \pm 0.59	0.01291 \pm 0.00510
718	13:29:54.75 +47:10:54.3	4.98 \pm 0.39	5.06 \pm 0.04	27.34 \pm 0.04	13.55 \pm 0.03	4.40 \pm 0.10	2.81 \pm 0.09	122.45 \pm 13.00	6.03 \pm 0.59	0.02471 \pm 0.00734
719	13:29:55.47 +47:10:54.1	7.15 \pm 0.41	6.67 \pm 0.52	34.46 \pm 0.55	17.52 \pm 0.50	4.57 \pm 0.46	3.85 \pm 0.46	143.77 \pm 13.00	6.78 \pm 0.59	0.02292 \pm 0.00607
720	13:29:56.20 +47:10:54.0	9.37 \pm 0.44	8.08 \pm 0.48	55.89 \pm 0.61	21.04 \pm 0.52	6.85 \pm 0.25	4.71 \pm 0.25	237.72 \pm 13.00	9.90 \pm 0.59	0.07623 \pm 0.01733
721	13:29:56.92 +47:10:53.8	20.86 \pm 0.50	12.54 \pm 0.51	108.04 \pm 0.74	35.85 \pm 0.58	12.11 \pm 0.28	8.47 \pm 0.27	232.93 \pm 13.00	13.99 \pm 0.59	0.11255 \pm 0.02331
722	13:29:57.64 +47:10:53.6	11.97 \pm 0.49	8.87 \pm 0.56	55.84 \pm 0.63	20.52 \pm 0.54	7.68 \pm 0.11	6.64 \pm 0.12	149.69 \pm 13.00	11.71 \pm 0.59	0.03993 \pm 0.00905
723	13:29:47.88 +47:10:49.5	3.02 \pm 0.33	3.32 \pm 0.25	14.79 \pm 0.22	5.84 \pm 0.21	2.69 \pm 0.03	2.04 \pm 0.03	67.32 \pm 13.00	4.11 \pm 0.59	0.00432 \pm 0.00332
724	13:29:48.60 +47:10:49.3	7.69 \pm 0.35	5.00 \pm 0.47	27.64 \pm 0.48	11.01 \pm 0.42	3.05 \pm 0.37	2.26 \pm 0.39	39.55 \pm 13.00	2.79 \pm 0.59	0.00349 \pm 0.00155
725	13:29:49.33 +47:10:49.1	4.89 \pm 0.20	4.58 \pm 0.24	21.44 \pm 0.26	10.14 \pm 0.23	3.74 \pm 0.03	2.96 \pm 0.03	21.49 \pm 13.00	4.74 \pm 0.59	0.00627 \pm 0.00191
726	13:29:50.05 +47:10:49.0	22.24 \pm 0.51	9.43 \pm 0.28	90.66 \pm 0.37	23.29 \pm 0.28	11.00 \pm 0.50	8.63 \pm 0.52	48.86 \pm 13.00	6.78 \pm 0.59	0.05047 \pm 0.01047
727	13:29:50.77 +47:10:48.8	21.34 \pm 0.11	8.72 \pm 0.51	75.94 \pm 0.67	21.97 \pm 0.54	8.50 \pm 0.50	6.42 \pm 0.49	9.80 \pm 13.00	4.32 \pm 0.59	0.02734 \pm 0.00553
728	13:29:51.49 +47:10:48.7	7.83 \pm 0.24	6.76 \pm 0.11	35.09 \pm 0.12	13.44 \pm 0.11	3.89 \pm 0.46	2.82 \pm 0.43	137.13 \pm 13.00	6.31 \pm 0.59	0.01843 \pm 0.00407
729	13:29:52.21 +47:10:48.5	9.18 \pm 0.43	8.46 \pm 0.11	53.41 \pm 0.13	21.39 \pm 0.11	7.54 \pm 0.48	5.57 \pm 0.49	270.16 \pm 13.00	6.48 \pm 0.59	0.06794 \pm 0.01537
730	13:29:52.93 +47:10:48.3	19.24 \pm 0.49	10.79 \pm 0.29	92.92 \pm 0.38	25.44 \pm 0.29	8.98 \pm 0.28	6.35 \pm 0.26	388.25 \pm 13.00	9.59 \pm 0.59	0.08024 \pm 0.01671
731	13:29:53.66 +47:10:48.2	13.86 \pm 0.27	7.83 \pm 0.52	61.63 \pm 0.65	19.43 \pm 0.54	6.39 \pm 0.10	5.01 \pm 0.11	109.20 \pm 13.00	8.40 \pm 0.59	0.03963 \pm 0.00823
732	13:29:54.38 +47:10:48.0	6.47 \pm 0.03	6.67 \pm 0.03	35.22 \pm 0.04	16.97 \pm 0.04	6.15 \pm 0.10	3.64 \pm 0.09	375.70 \pm 13.00	7.95 \pm 0.59	0.03417 \pm 0.00685
733	13:29:55.10 +47:10:47.9	16.88 \pm 0.10	19.21 \pm 0.29	107.20 \pm 0.40	47.21 \pm 0.32	12.99 \pm 0.03	12.43<			

TABLE 1 — *Continued*

ID	Equatorial Coordinates	H β	[NII] λ 6548	H α	[NII] λ 6584	[SII] λ 6717	[SII] λ 6731	Σ_{H2}	Σ_{HI}	Σ_{SFR}
----	------------------------	-----------	----------------------	------------	----------------------	----------------------	----------------------	---------------	---------------	----------------